Development of analytical and CAE models for a slotting process using thin-blades

by

Yazdan Kordestany

A thesis submitted in partial fulfillment of the requirements for the degree of

Master of Science

Department of Mechanical Engineering
University of Alberta

© Yazdan Kordestany, 2017

ABSTRACT

Steam assisted gravity drainage (SAGD) is one of the most popular methods used for heavy oil extraction in Canada. Of the existing sand control methods that can be used for SAGD, slotted liners can be considered among the superior ones in terms of their performance and cost of manufacturing. RGL reservoir management Inc. (RGL) is a company operating worldwide supplying sand control and flow control devices for oil extraction process. To manufacture slotted liners, RGL uses a custom made multi spindle slotting machine that has the capacity to cut 80 columns of slots at once. The manufacturing process employed by RGL has not been investigated for efficiency and opportunities to increase its production rate.

In this study, RGL's manufacturing process is taken as the case to analyze the mechanism involved in the cutting process affecting the process efficiency. The analysis results are then used to identify the major contributors to undesired conditions such as short tool life. The analysis techniques used in this research include force analysis through existing analytical and numerical models and implementing the results to conduct an in-depth analysis of the cutting dynamics.

The input parameters considered are blade geometry, cutting speed, and feed rate to investigate their effects on tool life. The resulting effects on tool life are studied through the analysis of forces that are involved in the cutting process. The study of dynamics of the cutting process was also extended to determine the effect of vibration by determining the stability lobe diagram of the process. Results coupled from these two primary parts of the investigation were used to identify optimal processing conditions.

The outputs from force analysis were used to compare different rake angle, relief angle, and blade material. Increasing rake angle resulted in decrease in the required force. As the rake angle increases, the relief angle should be decreased to preserve the material angle of the tooth

A stability lobe diagram which is used to identify ranges for stable operation was determined by making used of the results from force distribution. The approaches employed to specify conditions for the stability lobe diagram showed that the method can be applied to analyze different combinations of tool and workpiece materials.

The most common circular saw blade material was selected and its natural frequency was determined from analytical models and the literature. Existing machining constraints were also considered in determining the optimal shape. After comparing different geometries that results from optimization, a blade that has lower values for outer dimeter (2.93 in), relief angle (28^{o}), tooth height (0.073in), and number of teeth (50); and higher values for bore diameter (1.57 in), rake angle (5^{o}), gullet radius (0.027 in), and tooth pitch (0.184 in) than the current blade used by RGL was identified as the optimal blade.

To my parents – Reza and Sedigheh Kordestany

To my brothers – Ehsan, Hesam, and Amirhossein

To my wife – Sara Vaezafshar

ACKNOWLEDGEMENTS

I would like to thank my supervisor Prof. Yosngsheng Ma for his support and consideration during the period of conducting this thesis work. My deepest acknowledgement also goes to Mr. Michael Leitch since had it not been for his guidance in all aspects, I would not have been able to complete any bit of this research. I would also like to appreciate the cooperation by the whole team at RGL's Nisku shop especially to Mr. Jesse Lemishka.

I have benefitted a lot from the motivation I got from my family and friends who remained close to me at all times. I would, in particular, like to thank my friend Yishak Yusuf for all his support during my journey.

Thank you all!

Yazdan Kordestany

January, 2017

TABLE OF CONTENTS

LIST OF FIGURES

LIST OF TABLES

ACRONYMS AND SYMBOLS

W	Blade thickness (in)	$\emptyset$	Shear angle (degree)
L	I.D slot length (in)	β	Friction angle (degree)
RPM	Rotational spindle speed (rpm)	A_s	Shear plane area (in^2)
v_f	Feed rate (in/sec)	F_x	Force in x direction (N)
P	Plunge (in)	F_y	Force in y direction (N)
th	Pipe thickness (in)	T	Torque (N.m)
$\propto$	Rake angle (degree)	MRR	Material removal rate
γ	Relief angle (degree)	P_u	Friction power (w)
D	Blade diameter (in)	V_c	Deformed chip velocity (in/sec)
ω	Rotational speed (rad/sec)	V	Cutting velocity (in/sec)
H	Distance between the center of the blade and pipe surface at first position (in)	P_s	Shear power (w)
N	Number of blade teeth	V_s	Shear velocity (in/sec)
t_0	First touching point of teeth and pipe (s)	P_{tc}	Total power (w)
t_1	Blade reaches outer surface of pipe (s)	Q	Fracture toughness (psi$\sqrt{in}$)
t_2	Blade reaches inner surface of pipe (s)	E	Young’s modulus (Gpa)
t_3	Blade reaches its last position (s)	ρ	Density (kgm^{-3})
im_{in}	Half inner immersion angle	μ	Friction coefficient
im_{out}	Half outer immersion angle	b_{lim}	Minimum depth of cut (in)
θ_{ju}	Tooth position angle (degree)	Ω	Rotational speed (rev/sec)
N_e	Number of teeth engaged to the pipe	k_s	Force coefficient (N/m^3)
dt_0	Uncut chip thickness (in)	k	Stiffness (N/m)
F_c	Resultant force (N)	n_{cr}	Critical rotational speed (rpm)
F_t	Tangential force (N)	υ	Poisson ratio
F_f	Feed force (N)	$f_{s(n)}$	Natural frequency of non-rotating blade (Hz)
F_s	Shear force (N)	$f_{r(n)}$	Natural frequency of rotating blade (Hz)
τ_s	Shear stress (mpa)	λ	Centrifugal force coefficient

1. INTRODUCTION

Close to a third of the crude oil Canada produced from oil sands in 2014 used this technology Steam assisted gravity drainage (SAGD) [1].SAGD is an *in-situ* method that is used to extract oil from oil sand reserves. Developed by Roger Butler [2] SAGD is today one of the primary methods used to extract bitumen.

In SAGD shown in the Figure 1.1, pairs of horizontal parallel wells separated by a vertical distance of 4-6m are drilled for one kilometer of a horizontal distance. The upper of the two wells (injection well) is used to inject steam in the formation to lower the viscosity of the bitumen. The lower one (production well) is used to collect the produced oil. The well drilled into the formation removes earth for a well (casing) to be inserted to the well bore. The well bore is then cemented to increase the stability and isolate it from underground water to prevent contamination. A smaller pipe with a number of small slits is then inserted in the reservoir.

When steam is injected to the formation a steam chamber around the well is created [3]. The pressure of the steam should be lower than the fracture pressure of the rock mass to prevent the deflection of the rock [4]. Steam injection will go on for months during which the steam chamber expands and the viscosity of the bitumen decreases. This will cause the bitumen to flow down under gravity towards the production well. The produced oil is then pumped to the surface. Surface facilities are then used to separate the water and sand produced with the oil [3].

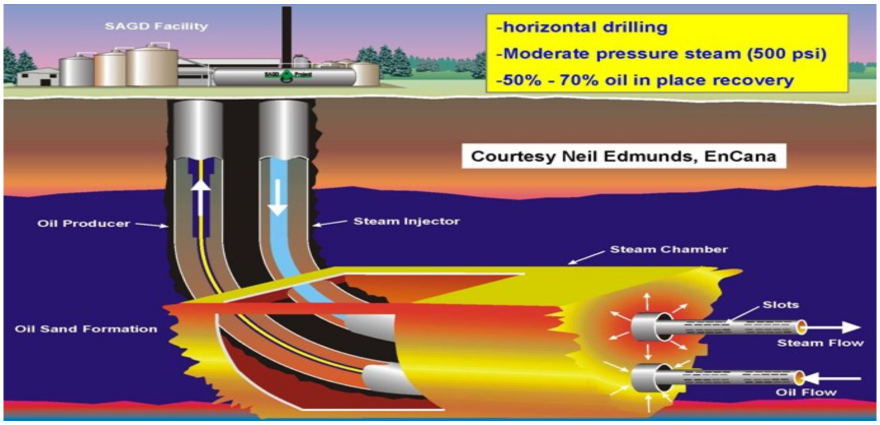

Figure 1.1 – Steam Assisted Gravity Drainage (SAGD) process of producing oil from oilsand reserves [5]

1.1 Sand control in SAGD

Reservoir formations are often made from unconsolidated sands, in contrast of sandstone formations having consolidated marine-deposited sands [4]. It is thus almost inevitable that oil extraction includes production of fines. Larger scales of solids produced along with fluids can devastate downhole tooling, wells, and surface equipment. Sand production is also a primary cause of plugging, formation of scale, fouling, etc. in the well completion pipes [6]. Sand control methods are, therefore, necessary to avoid passing of solids through the open area to flow allowed for oil production.

There are various methods developed to achieve sand control which is essentially preventing solids' entrance into the wells along with the producing fluid. One of such methods aims at restricting production rate by reducing the drag forces due to fluid velocity [4]. However, this approach can be deemed uneconomical as the variation of oil production with time dependent conditions is too complex to accurately predict [4].

Mechanical methods that add components to completion pipes such as slotted liners, wire wrap screens, and prepacked screens can also be used to keep formation sand in place within the wellbore [4]. The fundamental idea behind these techniques is to provide an open area large enough to achieve the required production rate while at the same time small enough for sand particles to pass [4].

Among such mechanical sand control techniques, slotted liners have gained much popularity as they are low cost alternatives to conventional case completions reducing the total well cost [4]. Wire-wrap screens are also considered a low-cost method [4] but with the natural sorting and formation of sand bridged playing a role that determines the performance of these screens. Prepacked screens can also be of sufficient applicability in low well rates coming with the limitation of getting plugged relatively easily with formation materials than the other mechanical sand control alternatives [4].

Of the available mechanical sand control methods, slotted liners have recently become one of the most popular methods employed for SAGD operations [7]. Slotted liners typically include a pipe casing on which rectangular apertures (slots) are made by methods such as cutting with circular saw blades. These slots will provide the required open area to steam injection and oil production while at the same time preventing sand particles to enter the pipe.

1.2 Slotted liners

Liner (pipe before slotting) is a generic term used for any devices in sand control that is placed in a well bore for sand control applications [8]. In most formations in Western Canada with poor and unconsolidated nature, slotted liners (pipe after slotting) are used extensively in SAGD operations. Objective of using slotted liner is to produce maximum amount of bitumen and other fluids with a minimum pressure drop along liners, preventing solids and clays entering the horizontal section of the well which can cause erosion, and downhole tools or surface equipment failure [6]. Meeting the objectives is a key factor to have a successful SAGD operation. It defines how well steam coning between wellbores is prevented by avoiding high differential pressure between production and horizontal well, and the formation sand is kept in place to prevent infilling of production well (during pumping up fluids) and injection well (during injecting steam) with solids which results in plugging [4].

It has been proven that slotted liners are one of the most popular methods of choice for sand control in SAGD due to their mechanical integrity for long horizontal well completions [4]. Slot geometry plays important role in preventing entry of sands. Figure 1.2 shows the three typical types of slot shapes that describe their profile along the pipe wall which are straight cut, keystone, and seamed. The profile of slot is important aspect in sand control performance of slotted liners. Although keystone slots cost more than straight cut slot, their relative performance in terms of sand control is much better than straight ones [9]. Since slot widths at the outer and inner diameters are the same in straight cut slots, the possibility of plugging to occur is high. Seamed slots also perform better than straight ones to prevent plugging by making the outer surface diameter smaller and narrower in comparison with inner diameter. The distribution of slot width in seamed and keystone slots is similar. As the opening is smaller on the outer surface of the pipe than the inner surface, fluid can pass without plugging taking with it particles that may have stuck in the slot [9]. This self-cleaning feature is what has come to be known as seamed slotted liners.

Geometrically a slotted liner is generally specified by the width, length, and arrangement of slots [4]. Slot width determines sand control efficiency of a slotted liner specially by defining anti-plugging characteristics [4]. The slot width is selected based on the particle size distribution of the formation and the condition of forming a sand bridge outside the slot [4]. The criterion thus set for the width of a slot is such that it is smaller than two times of the sand grain diameter usually less than 0.12mm $(1.5D_{50} \leq w \leq 2D_{10})$[1]. This specification defines a slot with through which 90% of total sand sample can enter through slots while sands with larger diameter cannot pass but form a sand bridge which has a high permeability.

Slots may be cut parallel or perpendicular to the axis of liners. It is mostly common to use parallel slot to axis so less strength of the pipe is lost due to cutting [8]. The liner diameter and sought slot arrangement will be used to select the slot length. Greater slot lengths are usually applied to liners with lower diameter and high strength.

(a) Straight cut slot

(b) Keystone cut slot

(c) Seamed top slot

Figure 1.2 – Slot profiles

All parameters related to slot geometry are manipulated to achieve the required open area to flow [9]. After the slot geometry is specified, staggered, gang, or straight patterns shown in Figure 1.3 can be used to arrange the slots along the liner surface. In straight pattern, slot columns are spaced evenly around the circumference without offset. In staggered pattern, slots evenly spaced around the circumference with offset. In gang pattern, multiple slots evenly spaced around circumference in a staggered pattern. Multiple staggered pattern or gang pattern are more commonly used in industry since they significantly increase the open area and, as a result, productivity as compared to single cut patterns [7]. Gang slot pattern also has superiorities with

---

[1] The D_{50} and D_{10} are particle size distribution parameters that represent the size which is larger than 50% and 90% of the sand particles, respectively [REF: Advanced well completion]

respect to installation torque-loading capacity and significantly develops the liner's resistance to lateral bucking and collapse pressures [7].

(a) Stagged slotted liner (b) Gang slotted liner (c) Straight slotted liner

Figure 1.3 – Slot patterns

Generally, slotted liners provide 2 to 3% of their total surface area open to flow [9]. Therefore, total number of required slots can be determined by knowing total external surface area of liners, slot width, slot length, and liner length.

Slot spacing and density (slot distribution) are essential to define and monitor parameters affecting inflow resistance. The specified open area, slot width, and liner's diameter can be used to calculate the number of slots per foot of liner as:

$$N = \frac{12\,\pi\,D\,C}{100\,W\,L} \tag{1.1}$$

where N is the number of slots per foot; D is the outside diameter of the liner (m); C is the required open area (percent); W is the slot width (m); L is the slot length (m).

1.3 Manufacturing process

Advanced techniques are used to manufacture slotted liners as per the specified geometry. One of the most commonly used methods to manufacture slotted liners is laser cutting process. For laser cutting, usually CNC indexing systems are used to ensure that slots are cut on the tube at the required radial and axial precision. This ensures that all requirements are met and maximum strength of pipe is maintained. There is not contact to the operation which has an advantage to avoid undesirable factors that cause the deformation of the base pipe. De-burring, cleaning and drift testing of produced liners according to API standards are included in the manufacturing process.

Water jet cutting process is another approach used to manufacture slotted liners. Water jet makes slots that are free of burrs so that there is no need for cleaning and post cutting steps involved in the process. Any design of slot pattern can also be made without the need to follow pre-defined arrangement and distribution imposed by other techniques such as that of saw spindles. Less amount of steel is thus removed from the pipe making the produced slotted liners have an increased strength. Increases in the production rate and accuracy in the produced slots' geometry can therefore are expected from water jet cutting process.

Circular saw blades can be used as a tool to manufacture slotted liners in numeric control (NC) milling machines. There are several industries that apply multi spindle NC machines to produce slotted liners. Since each pipe joint has hundreds of slots, this approach has the advantage of reducing production time. Having multi-spindle slotting machine benefits cost and time in such a way that it allows simultaneous cutting of slots as many as the number of spindles. The cutting process leaves a significant volume of wickers and burrs in the edges of inner diameter of slots. Post-cutting steps of de-burring, cleaning, and drift testing are therefore a necessity.

Straight cut slots are relatively the easier and most economical ones to produce. In the production of seamed slots, straight ones are cut first and other manufacturing processes are used to alter the geometry. Multi spindle slotting machines are commonly is used to create conventional straight slots. The pipe is first adjusted on the machine's bed and V-pack, aligned with the spindle's center and kept by jaws. Typical multi spindle slotting machine is shown in Figure 1.4. Spindle speed, feed rate, depth of cut, and plunge are then set by the operator. The cutting tools, circular saw blades in this case, move to a stationary position at a specified distance from the liner to be slotted without any rotation. The schematic process is shown in the Figure 1.5.

Blades start to rotate with the specified rate and begin to move toward pipe to be slotted. When the first cutting finishes, cutters move to their stationary position and the pipe is rotated about its axis by a specified degree depending on slot density. The blades move towards the pipe to cut second column. This process repeats until all the columns of slots are made on the pipe. If a coolant is applied continuously the pipe's metallurgical integrity can be kept for the whole machining process. There can be an advanced version of this multi-spindle cutting machine which has the capacity of cutting two rows of slots at once where pipe is located between two rows of cutters.

Slots that are made using such a multi-spindle machine have the same widths at the outer and inner sides of the pipe diameter which is equal to the blades' thickness. However, Figure 1.6 shows the difference in OD and ID slot lengths that is caused due to plunge of cutters where cutters have a limited movement to prevent pipe and blade's bore encounter.

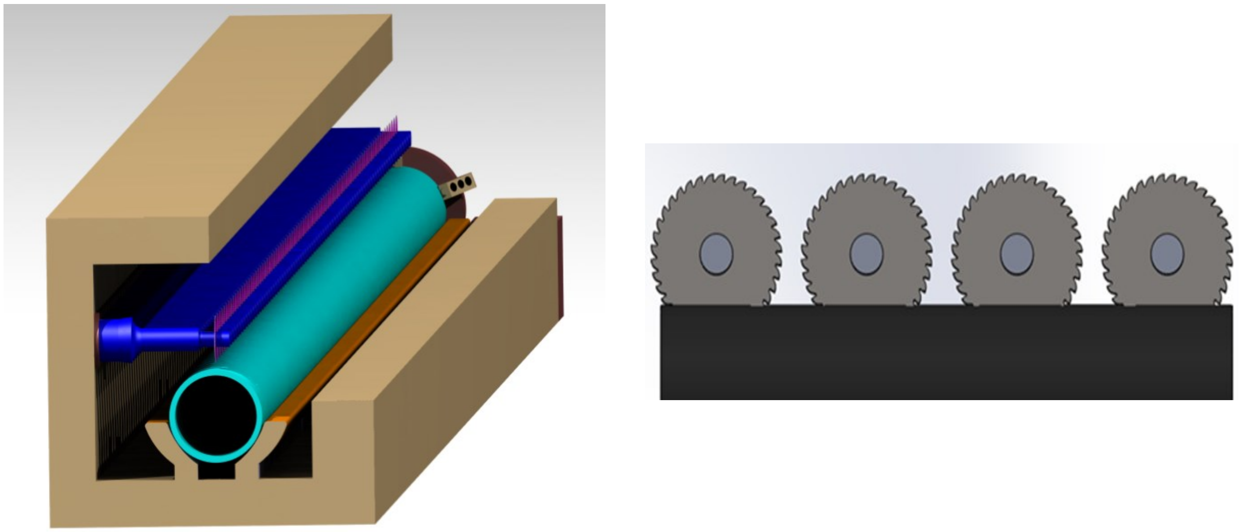

(a) Isometric view (b) Front view

Figure 1.4 – A solid model of the multi spindle slotting machine

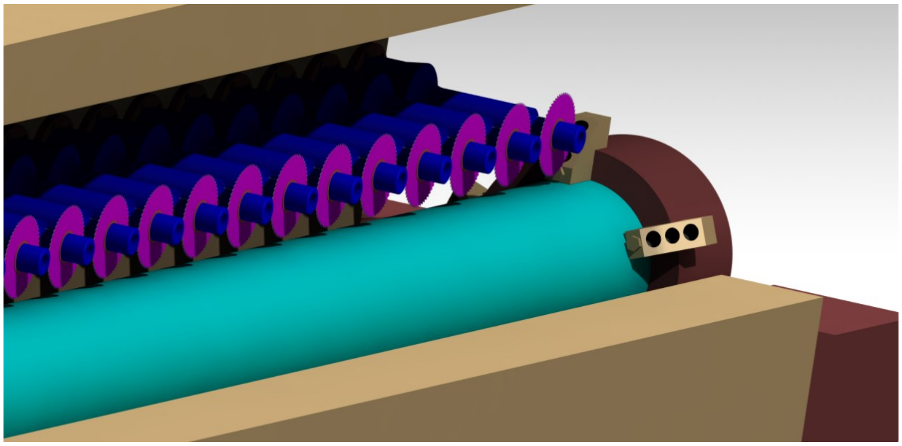

(a) General view

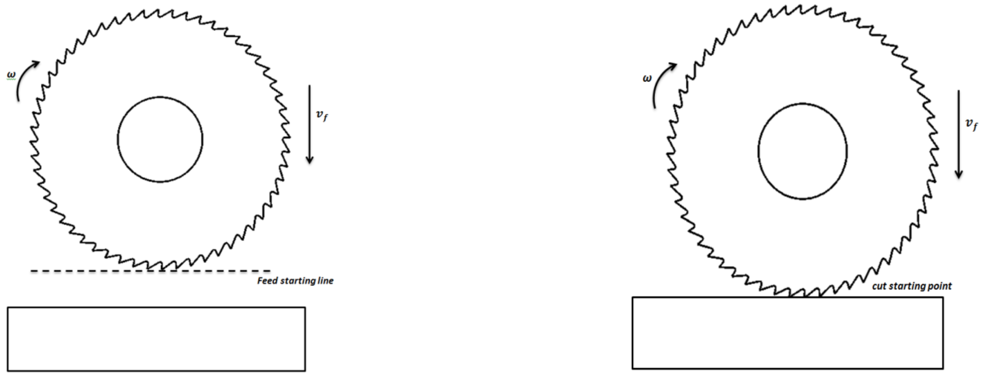

(b) First position of the blade (c) First touching point of the workpiece

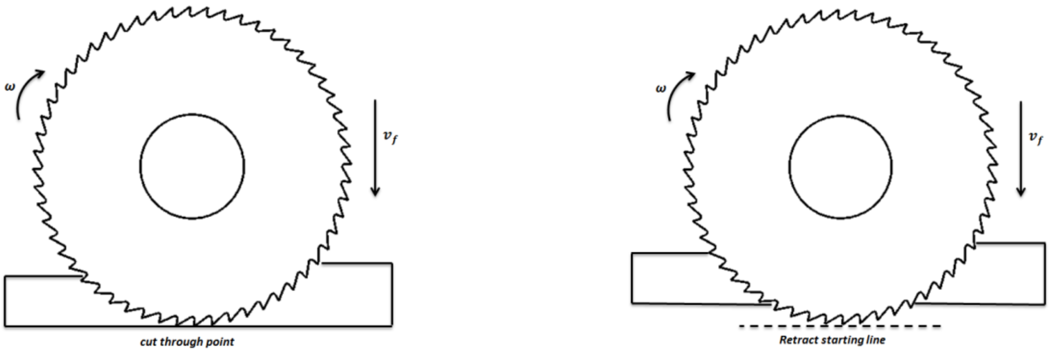

(d) Touching the ID of pipe (e) Last position of the blade

Figure 1.5 – Schematic showing stages in the machining process

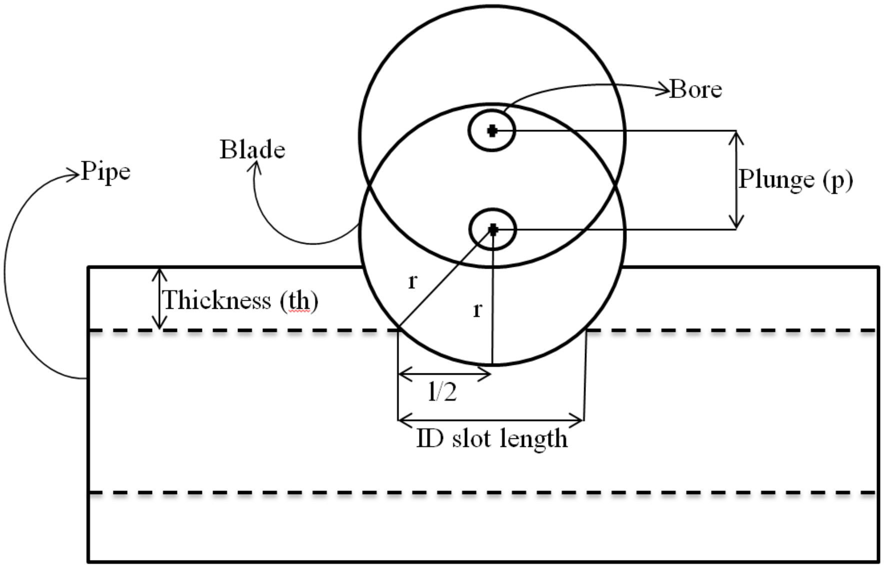

Figure 1.6 – Last position of the blade

The manufacturing process for keystone slots is different than that used for straight ones. Two separate blades at different angles (not perpendicular to pipe) are used to make the slots. A 6° angle is usually used to form the inverted-V shape of keystone slots. Slot width at the outer diameter of liner is smaller than that at the inner diameter which is a proper design to prevent sand grain entrance. Figure 1.7 shows sand grains forming a bridge across the slot opening.

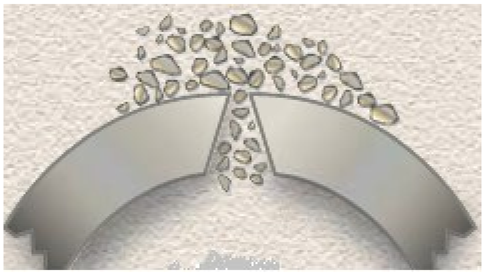

Figure 1.7 – Sand bridging in keystone slot

One method that can be used to make keystone slots is the double cutting slot technique. In this process the pipe is rotated on the center axis after one row of slots on the pipe surface are cut. This process is repeated until the inverted-V shape is formed for all the slots. The problem of this process is that the cutter usually cannot maintain the desire angle and it bends and shakes because of unbalanced pressure.

To manufacture seamed slotted liners, a specific machine is used after making straight slots. A cylinder roller rotates around pipe applying pressure to the outer surface of the slotted liner. Only the cylinder rotates at a specified RPM around the slotted liner to be seamed with its center aligned with that of the slotted pipe. The slotted pipe moves through cylinders along the axial direction with determined speed. The moving speed should be set on the seaming machine to cover all slots and ensure that the shape of all straight slots takes the seamed profile shown in Figure 1.8. Seamed slot width in outer diameter is set as per production requirement which is based on several factors in the reservoir such as particle size distribution and fluid property. The slot width at the inner side of the pipe diameter, however, remains the same as the thickness of the circular saw blades used in the straight slot manufacturing process.

(a) Straight slot

(b) Keystone slot

Figure 1.8 – Straight vs keystone slot

Machining processes that remove unwanted material from the workpiece by using cutting tools that are harder than the workpiece are more demanding [10]. They have the ability to achieve tighter tolerances, better surface quality, complex geometry, and economical justification for part machining. Input variables for such processes include workpiece material property and geometry, tool material property and geometry, cutting parameters and fluid, and holding devices. Cutting forces and power, geometry of final product, surface finish quality, tool failure, and economic costs are considered as output variables. Choosing a proper machining process to produce a specific component therefore depends on part shape, part size, part material, geometric features, surface textures, production quantity, production cost, and environmental impacts.

1.4 Problem statement

RGL Reservoir Management Inc. (RGL) is engaged in design and manufacturing of downhole tooling for oil recovery operations. Its products primarily include devices for sand control as well as inflow and outflow of heavy oil. For SAGD applications RGL is the leading supplier of mechanical sand control devices in the world mainly for slotted liners.

RGL uses a slotting machine that has a similar configuration as NC horizontal milling machine to manufacture slotted liners shown previously in the Figure 1.4 and Figure 1.5. The machine includes multiple spindles (80) to make multiple slots simultaneously. This feature of the manufacturing enables RGL to have an increased production rate.

Pipes material, dimensions and slot geometry are specified by clients which leaves RGL with no flexibility on workpiece selection. Although blades are procured by RGL, the selection still has to be as per clients' specification for pipe material, slot length and width which puts a limitation on its own. According to the slot specifications provided by the client, RGL uses blades of the same thickness as the required slot width. These blades are mounted onto the arbor of the machine for the slotting process. Values for the RPM of the motors that drive the spindles, the feed rates, and the plunge are set before the slotting process starts. Twenty motors are used to drive the 80 spindles (1 motor per 4 spindles). The feed rates can be manipulated to maximize production rate and minimize possibility of blade breakage. The plunge along with the blade diameter determines the length of the slot required. The plunge has to be set at a value where interference between the bush and the workpiece is avoided.

Cutting parameters have direct impacts on production rate. Spindle speed (RPM) and depth of cut determine linear velocity and therefore tangential velocity, cutting angle, and cutting forces. Cutting forces, as a result of proper selection of depth of cut and spindle speed, should maintain dynamic stability of the system to prevent vibration. Spindle speed is the major factor in determining tool life. Extreme feed rates generate excess heat which softens the tool and ultimately causes the edge to get dull. Optimum values of feed rate are also important with respect to the material removal rate. Higher feed rate results in more material removal rate, but with a significant shortcoming in terms of tool breakage due to shocks either at entrance of the blade tooth into the pipe or during the exit of the tooth from the pipe.

The slotting machine used by RGL has been designed and built in-house. Since it was custom made, important parameters that are used to specify such machines cannot be referred to in standards or handbooks. Prediction of performance parameters is almost impossible due the lack of data for defining values such as maximum capacity. Selection of process parameters, tool specifications, and workpiece specifications that affect productivity, therefore, had to be based on observations.

Another point to address is the effect of machine and/or tool vibration on production process. The potential effect of vibration was observed through the lower-than-expected tool life, and audible noises during machining. Blades width is usually so thin (typically around 0.023 in) to cause vibration.

1.5 Objectives

This research aims at obtaining a comprehensive description of RGL's manufacturing process with respect to interacting performance parameters according to the problem stated above. With the ultimate goal of increasing the production rate and hence the profit of RGL, the following are the major objectives set for this study.

- Conduct force analysis on the blades to determine the distribution of forces and identify causes for decreased tool life or breakage;
- Perform dynamic stability analysis to obtain a stability lobe diagram to determine combinations of feed rate and spindle speed values that are in stable and unstable zones, and;
- Identify the shape of blade for optimized natural frequency for maximum tool life.

To achieve these objectives a combination of analytical and numerical methods is applied. Fundamental physics governing the cutting process and distribution of forces on the blades are used in developing the domain for numerical investigation and the required algorithm to solve the analytical equations.

1.6 Thesis organization

The discussion of this research is presented in the five chapters that follow. Review of relevant literature is given in Chapter 2. Methods that are used to carry out force analysis and dynamic stability analysis are discussed in Chapter 3. The chapter that follows, Chapter 4, states the results obtained from both analytical solutions and numerical simulation of the problem. A separate chapter, Chapter 5, is dedicated to present results pertaining to geometry of the blade by making reference to the force analysis results in the preceding chapter. The final chapter concludes the thesis by outlining the major conclusions drawn for the research and future directions suggested.

2. LITERATURE REVIEW

2.1 Force analysis

Metal cutting (machining) is a frequently used manufacturing process that has the ability to achieve tighter tolerances, better surface quality, and complex geometry [11]. Selection of operating parameters such as machine tool, cutting tool, and workpiece characteristics is essential for an economic manufacturing process. Tolerance accuracy and surface quality need to be evaluated by measurement of shear angle, cutting force, cutting power, surface finish, tool wear, deflections, temperatures, vibrations, and part dimensions [11]. Such cutting operations that remove material from the blank include turning, milling, drilling, sawing, boring, broaching, hobing, shaping, slotting, and form cutting [12]. Grinding operations that are used after cutting provide a high quality surface finish and precise dimensions[11].

The two basic categories of metal cutting process – orthogonal and oblique – are illustrated in Figure 2.1. Most machining processes apply oblique metal cutting. The cutting edge in oblique cutting is inclined at an acute angle to the cutting velocity and feed [12]. However, investigating the physical phenomena and mechanics of machining involved in orthogonal metal cutting process is often adequate to describe the whole process as it has been extensively studied [13].

Slotting process is to make slots or grooves on the on the workpiece by feeding a tool towards a fixes or movable part. In the slotting process, the mechanics on each tooth on the circular saw blade follows orthogonal cutting theory since the cutting edge of each tooth is parallel to the surface of the workpiece and perpendicular to the cutting orientation [13]. The material removal process is also considered to be distributed along the cutting edge. It is thus a two dimensional plane strain problem [14].

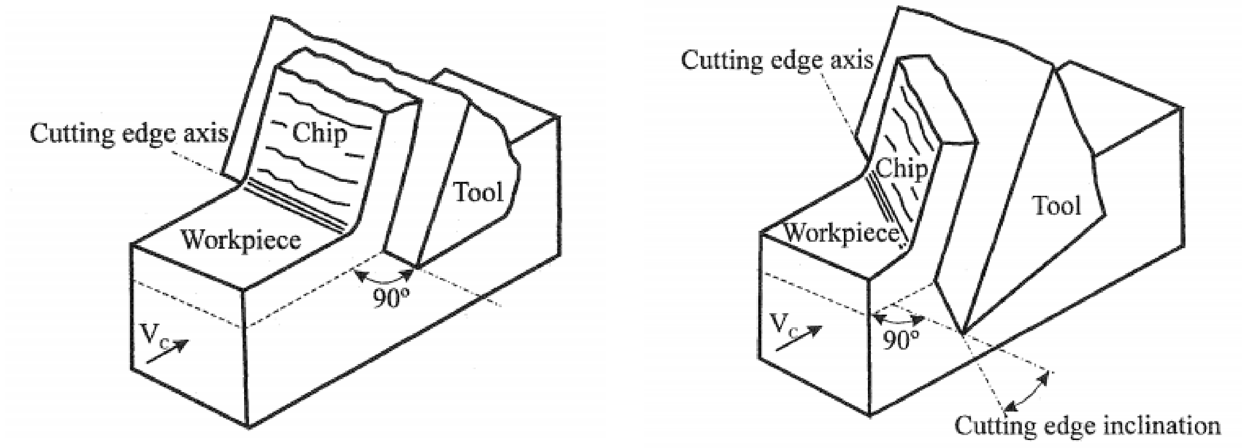

(a) Orthogonal cutting (b) Oblique cutting

Figure 2.1 – Metal cutting categories[13]

2.2 Orthogonal metal cutting

Although there have been many studies on mechanics of machining, especially empirical methods, it can be said that the ability to fully describe the various processes also accounting for changing processing conditions has not yet been attained. Nowadays, the focus is on the development of analytical and numerical methods to ensure such a comprehensive description of machining processes [13].

A good understanding of important parts of machining that have significant influence on the entire process is hence required. One of such parameters is chip formation [15]. Finite Element Method (FEM) has been taken as the suitable tool to describe chip formation since it is not easy to empirically measure this parameter because of the highly localized chip formation with large strain, high strain-rate, high temperature, velocity, and chip-tool friction [16]. Studying chip formation also plays substantial role in determining cutting force, cutting temperature, and tool wear [17]. Three types of chips generally form [10] during a cutting process as shown in Figure 2.2. These are discontinuous chips, continuous chips and continuous chip with built-up edge (BUE).

(a) (b) (c)

Figure 2.2 – Chip formation: (a) Discontinuous, (b) Continuous, (c) Continuous with BUE [10]

Discontinuous chips form when brittle or some ductile metals are machined under low cutting speed conditions [13]. They are also common in processes that have machine vibration or tool chatter [10]. The production of continuous chips is often associated with better surface finish especially for ductile metals under high speed cutting [10]. Continuous chip with built-up edge forms when low carbon machining steels are cut with high speed steel cutting tools under low cutting speeds and it is considered to shorten the tool life [10].

Continuous chip formation is further illustrated in Figure 2.3 [18]. In zone 1, the material is subjected to a shear deformation. The workpiece material is deformed due to high friction at the chip-tool interface shown as zone 2 in front of the rake face, and the flank face. In zone 3, material separation takes place due to high pressure from all sides. Slight material shearing might occur in zone 4 because the flank face can plough the newly generated surface. There is also a chance to have a slight plastic deformation in zone 5.

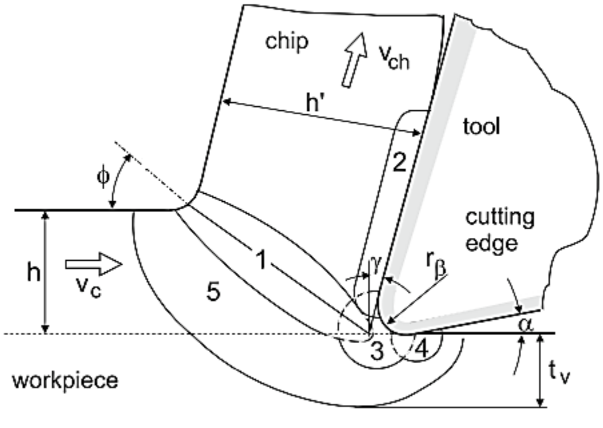

1. Primary shear zone
2. Secondary shear zone at the rake face
3. Secondary shear zone at the stagnation zone/separative zone
4. Secondary shear zone at the flank face
5. Preliminary deformation zone

Figure 2.3 – Chip formation zones [18]

Different approaches have been proposed to model metal cutting processes. One method that has been applied for a long time is the empirical model. Taylor's equation can be considered as the representative example for empirical approaches used since the early 1900s for developing relationship between cutting speed and tool life for cutting steel with a wide variety of tools [19]. However, empirical approaches have always been criticized [19] because similar machining processes have difference in their measured results and results from empirical models are based on specific conditions and original data from testing facility.

Analytical methods have also been used to model metal cutting processes [19]. The Rowe-Spick [20] and Merchant's [21] models can be mentioned as examples that are based on minimum energy principle to predict shear plane angle. The Oxley model [22] predicts the angle between the shear plane and the resultant cutting force.

The assumption that cutting forces are proportional to the uncut chip area is applied in mechanistic models for three dimensional cutting processes [10]. Prediction of cutting forces and tool deflections in end-milling process by applying mechanistic model is covered in [23]. In this model it has been shown that tangential and radial force components depend on instantaneous chip thickness. The flutes of the end-mill have been decomposed into thin axial slices to obtain the instantaneous cutting force by summing force elements for each slice. It should be noted here that the estimation of the instantaneous chip thickness can have considerable complexity if there is no perfect alignment between the cutting tool axis , the tool-holder, and machine tool spindle [19] which is called runout. It is also important to simulate the cutting process when cutter is in contact with the workpiece which requires consideration of cases when flutes are between entrance and exit angles.

Two principles can be followed in the development of models based on finite element analysis: continuum and discretized. Continuum equations are approximated by a number of small different shapes (triangles, rectangles, etc.) called elements. Simplification of a continuum problem can be achieved by applying finite element analysis (FEA) which reduces the problem of infinite changes to large but finite number of variations [19].

2.3 Analytical models of orthogonal metal cutting

The literature contains little work conducted to develop predictive analytical models for the cutting process using circular saw blades. As one of this thesis' primary objectives requires modeling such cutting processes beginning with the mechanics of a single tooth, the review has been focused on methods that can be adapted to the present case. The review of similar orthogonal metal removal processes that apply analytical models to describe their cutting action is presented in this section.

Since mid-1800s there have been several researches conducted to develop analytical models for effects of process parameters and material behavior. In the work by Time et al. [24], it is claimed that the chip is created by shearing ahead of the tool based on observations. Tresca [25] on the other hand stated that the chip is produced due to compression ahead of the tool in metal cutting. Zvorykin [26] developed an equation to predict the shear angle based on the single shear plane model. Mallock [27] has also studied about the shearing mechanism noting importance of friction in the tool-chip interface. The publication by Piispanen [28] presents a "deck of cards" analogy as shown in Figure 2.4 in which the shear plane is the workpiece which also makes a sudden transition into a chip. Ernst and Merchant [29] researched on single shear plane model assuming that the chip acts like a rigid body, the tool is perfectly sharp, and a continuous chip without BUE occurs. Later, Merchant published a comprehensive analytical cutting model [30][21]. The works by Lee and Shaffer [31], Kobayashi and Thomson [32], and Oxley [33] are a few among many that can be said to have made significant contributions in defining the mechanics of metal cutting.

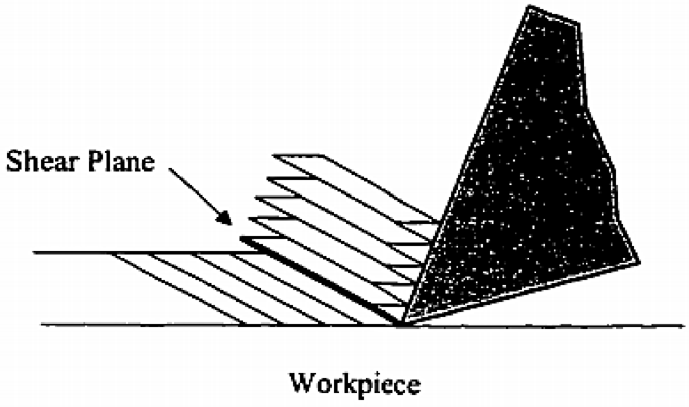

Figure 2.4 – Metal cutting deck of cards analogy[28]

In the shear plane model from the theory of Ernst and Merchant [29], shear forms the chip along a single plane inclined at an angle ϕ. The shear stress along the shear plane is equal to the material flow stress in shear. The chip is assumed to be a separate body in static equilibrium as shown in Merchant's circle force diagram given in Figure 2.5. Merchant derived equations for cutting and thrust forces showing their dependence on the shear angle. All forces act at the tool tip. The forces applied to the chip come from two parts: the tooth, and the uncut workpiece. The balance of these forces results in the force equilibrium.

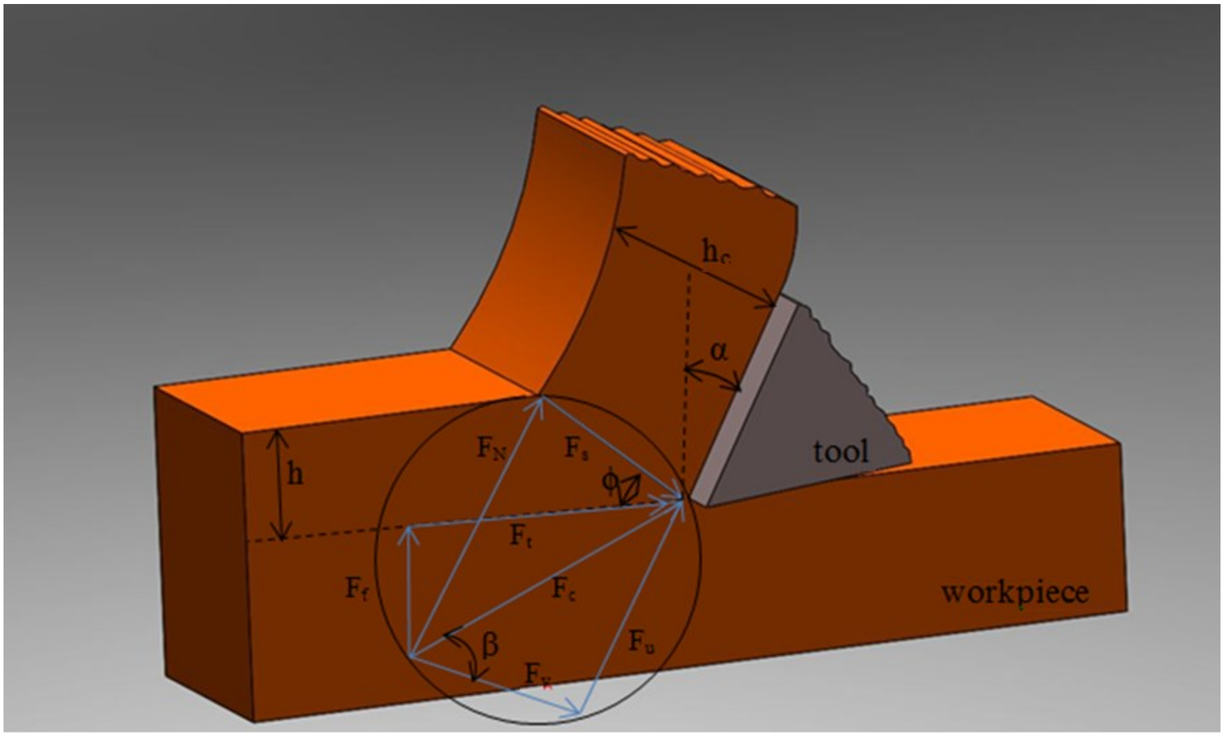

Figure 2.5 – Merchant's circle force diagram

where:

- Friction force F_u: it is the component of the resultant force applied by the single tooth to the chip which is parallel to the contact surface between the chip and the single tooth.
- Normal force F_v: it is another component of the resultant force applied by the single tooth to the chip which is perpendicular to the contact surface between the chip and the rake face of a single tooth.
- Shearing force F_s: shear force applied by the uncut workpiece to the chip which is parallel to the shear plane.

- Normal force F_n: normal force applied by the uncut workpiece to the chip which is normal to the shear plane.
- Resultant cutting force F_c: the resultant force applied to the chip by the individual tooth is decomposed to:
- F_t: tangential or power force which is in direction of cutting velocity.
- F_f: feed or thrust force which is in direction of uncut chip thickness.
- α: the rake angle
- ϕ: the shear angle
- β: the mean angle of friction between chip and tool

it should be noted that F_u and F_v are in balance with F_s and F_n.

The friction angle is related to friction coefficient of the chip sliding on the tool, μ, such that.

$$\mu = tan\beta = \frac{\mathrm{Fu}}{\mathrm{Fv}} \tag{2.1}$$

The friction coefficient is often taken as an average constant value in orthogonal cutting analyses. However, in actual cases the chip sticks to the rake face for a short time and slides over the face with at a constant value [12].

Ernst and Merchant's theory is based on minimum cutting energy principle to reduce the cutting work to a minimum. Since the main factor is cutting force, two steps should be involved in the analysis. Establishing the relationship between cutting force and shear angle should be done first followed by identifying the shear angle to keep the cutting force at the minimum. From Figure 2.5 it can be seen that:

$$F_s = F_c \cos(\phi + \beta - \alpha) \tag{2.2}$$

$$F_s = \tau_s \, A_s = \tau_s \, \frac{w\, h}{sin\phi} \tag{2.3}$$

where, τ_s is the shear stress, A_s is the shear plane area, w is the width of cut, and h is the uncut chip thickness.

From equations (2.2)and (2.3):

$$F_c = \tau_s \frac{w\,h}{sin\phi} * \frac{1}{\cos(\phi + \beta - \alpha)} \tag{2.4}$$

The tangential and feed forces can then be written as:

$$F_t = F_c \cos(\beta - \alpha) = \tau_s \frac{w\,h}{sin\phi} * \frac{\cos(\beta - \alpha)}{\cos(\phi + \beta - \alpha)} \tag{2.5}$$

$$F_f = F_c \sin(\beta - \alpha) = \tau_s \frac{w\,h}{sin\phi} * \frac{\sin(\beta - \alpha)}{\cos(\phi + \beta - \alpha)} \tag{2.6}$$

From the equilibrium of cutting forces, the total power consumed in cutting (the sum of energy spent in the shear and friction zones) equals the cutting power drawn from the spindle motor so that:

$$P_t = F_t\,.V \tag{2.7}$$

where, P_t is the cutting power, and V is the cutting velocity. According to Merchant's minimum energy principle in predicting the shear angle, by taking the partial derivative of the cutting power it can be written that:

$$\frac{dP_t}{d\phi} = \frac{dF_t.V}{d\phi} = \frac{-V\tau_s\,w\,h\,\cos(\beta - \alpha)\,\cos(2\phi + \beta - \alpha)}{sin^2\phi\,cos^2(\phi + \beta - \alpha)} = 0 \tag{2.8}$$

It can therefore be said that:

$$\cos(2\phi + \beta - \alpha) = 0 \tag{2.9}$$

$$\phi = \frac{\pi}{4} - \frac{\beta - \alpha}{2} \tag{2.10}$$

The theory by Ernst and Merchant has its own drawbacks of being over simplified which is attributed to the assumption of constant friction coefficient and the consideration of only continuous chip formation. The velocity and force diagrams presented by Ernst and Merchant also have some deviations from actual conditions. The effect of cutting speed on the material behavior during machining was also not explained in this theory. However, it is possible to apply the theory as a logical beginning to predict shear angle and develop preliminary understanding of the relation between shear angle, tool rake angle, and friction angle of the chip-tool interface. Approximations with respect to continuous chip formation with built-up edge can also be obtained by applying this theory. Direct measurement of either shear angle or thrust force to evaluate other existing parameters and phenomenon presents much difficulty. It is therefore easier to determine the shear angle c using experimental (indirect) methods so that the shear angle ϕ, such that:

$$tan\phi = \frac{r_c \; cos\alpha}{(1 - r_c \; sin\alpha)} \tag{2.11}$$

where, r_c is the chip thickness ratio (cutting ratio) defined as the ratio of the uncut chip thickness to the deformed chip thickness (h_c) as:

$$r_c = \frac{h}{h_c}, \qquad 0 < r_c < 1 \tag{2.12}$$

Contrary to the range indicated to limit the chip thickness ratio to be between 0 and 1, there can be where the value exceeds 1. Machining at high cutting speed can be mentioned as a particular case. An argument for this hypothesis for the chip thickness ratio given by Merchant has been forwarded by Kronenberg [32].

Accounting for physical properties of the workpiece to control plastic behavior has been considered in [21]. In this work, it is assumed that the shear stress on the shear plane equals to the shear strength of the material. It is also assumed that constant shear strength applies on the shear plane during machining. Making substitution into the derived equations based on the assumption that having material plasticity dependent on shear strength led to the concluding equations that are free of all force components.

Merchant has also considered the condition where only compressive shear stress on the shear plane influences the shear strength. Again, based on minimum energy principle, Merchant derived the following equation for the shear angle.

$$\phi = \frac{1}{2} cot^{-1} k - \frac{1}{2}(\beta - \alpha) \tag{2.13}$$

where, k is a material constant relating shear stress and compressive stress and:

$$\tau_s = \tau_{s0} + k\,\sigma_s \tag{2.14}$$

where, τ_{s0} is shear strength of the material under zero compressive stress, and σ_s is the normal stress on the shear plane. Equation (2.14) has a good approximation for SAE 4340 steel [21] according to results from experiments, although some parameters such as strain and temperature rise on the shear strength were not involved.

The works by Krystof [34], Lee and Shaffer [31] adopted the slip-line field theory to develop shear angle relations base on maximum shear stress principle which implies that shear occurs in the direction of maximum shear stress. This model is suitable for either continuous chip formation or continuous chip formation with built-up edge. It was mentioned before that the angle between resultant force and shear plane is $(\phi + \beta - \alpha)$, and the angle between the maximum shear stress and the principal stress must be $\left(\frac{\pi}{4}\right)$, so:

$$\phi = \frac{\pi}{4} - \beta - \alpha \tag{2.15}$$

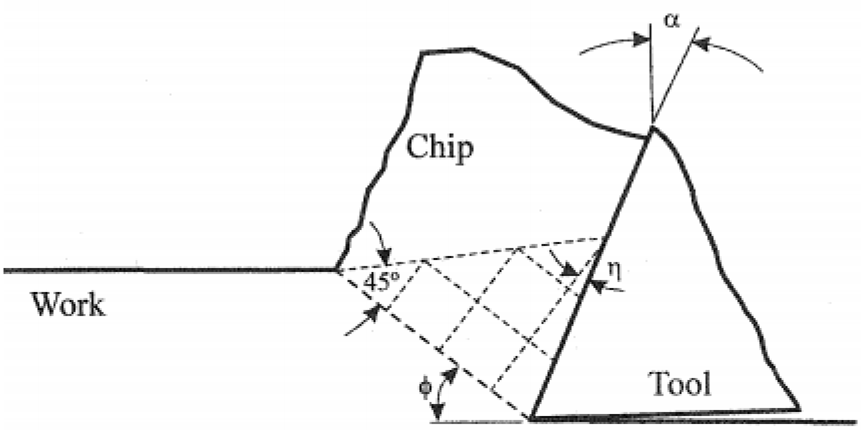

Figure 2.6 – Slip-line field configuration[31]

Following the slip-line field theory, Palmer and Oxley [33] has included the variation of the flow stress during machining process by adapting Hencky plasticity which considers work-hardening. The study was based on shear plane model which has been simplified to exclude the determination of the cutting forces. However, some important parameters could not be quantified without finding the cutting forces. Oxley [35] has later developed a more realistic model by including data for strain rate, strain hardening, and effects of temperature to predict conditions in built-up edge formation during cutting of steel as depicted in Figure 2.7. The new model has also proceeded to cover extreme conditions existing at the deformation zones. Equilibrium of forces has also been considered in this model for the shear plane force and the tool-chip interface force.

The relationship for the shear angle can accordingly be given as [19]:

$$tan\theta = 1 + 2\left(\frac{1}{4}\pi - \phi\right) - Cn \tag{2.16}$$

where, θ is the angle between resultant force and shear plane $(\phi + \beta - \alpha)$, C is the constant in an empirical strain-rate relation based on Stevenson and Oxley's [19] which gives:

$$\dot{\Upsilon}_s = \frac{C\ V_s}{l_s} \tag{2.17}$$

where, $\dot{\Upsilon}_s$ is the maximum shear strain-rate at the shear plane, V_s is the shear plane velocity, and l_s is the length of the shear plane. In (2.16) n is the strain-hardening index defined in [19] as:

$$\sigma = \sigma_1\ \varepsilon^n \tag{2.18}$$

where, σ and ε are the uniaxial (effective) flow stress and strain, respectively. σ_1 is a constant.

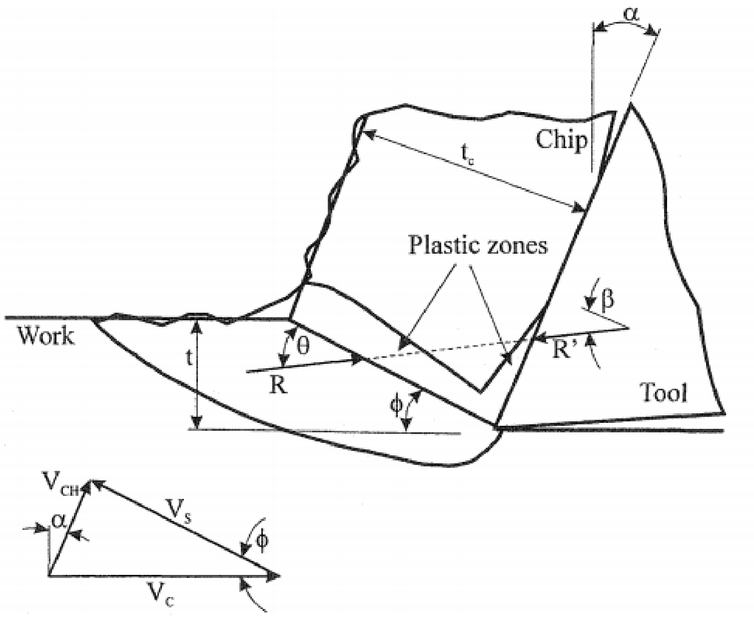

Figure 2.7 – Chip formation by Oxley [19]

Oxley's models [22] show some drawbacks when dealing with high speed cutting operations due to inadequate data on stress-strain relations in the flow zone at the tool-chip interface and difficulty of contact length measurement [19].

Considering energy consumption similar to the minimum energy principle by Merchant [21], Rowe and Spick [20] developed a model for shear angle by applying a graphical approach. It was concluded that the temperature, tool wear rate, and machinability of the work material are affected by the contact area at the tool rake face.

A non-exhaustive list of some of the developed predictive models the shear angle is given in Table 2.1. The most common solutions are those based on single shear plane and shear zone assumptions. All shear angle solutions do not provide high levels of accuracy and some oversimplify the conditions. These shortcomings may in particular be with respect to accounting for the physics and mechanics of metal cutting mainly due to lack of enough data for changing material properties for common tests and machining processes.

Table 2.1 Shear angle models[5][36]

Model	**Equation**	**Year**
Zvorkin	$\phi = \frac{\pi}{4} + \frac{\alpha}{2} + \frac{\beta}{2} + \frac{\beta'}{2}$	1890
Ingenious Text	$\phi = \frac{\pi}{4} - \frac{\alpha}{2} + \frac{\beta}{2}$	1896
Lindner	$\phi = \frac{\pi}{4} + \frac{\alpha}{2} + \frac{\beta}{2} + \frac{\beta'}{2}$	1907
Ernst and Merchan	$\phi = \frac{\pi}{4} + \frac{\alpha}{2} - \frac{\beta}{2}$	1941
Merchant	$\phi = \frac{C}{4} + \frac{\alpha}{2} - \frac{\beta}{2}$	1945
Stabler	$\phi = \frac{\pi}{4} + \frac{\alpha}{2} - \beta$	1951
Lee and Shaffer	$\phi = \frac{\pi}{4} + \alpha - \beta$	1951
Hucks	$\phi = \frac{\pi}{4} - \frac{tan^{-1}2\mu}{2} + \alpha$	1951

Model	Equation	Year
Hucks	$\phi = \frac{cot^{-1}k}{2} - \frac{tan^{-1}2\mu}{2} + \alpha$	1951
Black and Hung	$\psi = \frac{\pi}{4} - \phi + \frac{\alpha}{2}$	1951
Shaw, Cook, and Finnie	$\phi = \frac{\pi}{4} + \alpha - \beta + \eta$	1953
Sata	$\phi = \frac{\pi}{4} - \alpha \pm \frac{\alpha - 15^{\circ}}{2}$	1954
Weisz	$\phi = 54.7^{\circ} + \alpha - \beta$	1957
Kronenberg	$\phi = cot^{-1}\left[\frac{e^{\mu\left(\frac{\pi}{2}-\alpha\right)} - sin\alpha}{cos\alpha}\right]$	1957
Colding	$\phi = tan^{-1}\left[-\frac{2\left(\frac{F}{H}+2\right)}{\left(\frac{F}{H}+1\right)} cot(2\Omega) - (\beta - \alpha)\right]$	1958
Oxley	$\phi = tan^{-1}\left[1 + \frac{\pi}{2} - 2\phi + \frac{cos2(\phi - \alpha)}{tan\rho} - sin2(\phi - \alpha)\right] - (\beta - \alpha)$	1961
Sata and Yoshikawa	$\phi = cot^{-1}\left[cot\theta + \frac{cos\theta}{sin(\theta + \alpha)} kL\right]$	1963
Das and Tobias	$D = \frac{cos(\beta - \alpha)}{cos(\beta - \alpha + \phi)}$	1964
Payton	$x + \beta = \frac{\pi}{4} + \frac{\alpha}{2} = \psi + \phi$	2002

2.4 Numerical analysis of orthogonal metal cutting

Direct experimental techniques used to study cutting processes are usually costly and time consuming. Therefore, analytical and numerical approaches may appeal the researcher. It should, however, be noted that the mechanics of machining cannot be fully explained by using only analytical approaches. This is the main reason behind the application of numerical methods such as finite element analysis in conjunction with analytical models. There are various explicit and implicit software packages that are commonly used to perform finite element analysis including

ABAQUS, ANSYS, DEFORM-2D/3D, ADVANEDGE, FEMAP, NASTRAN) for the modeling of metal forming processes, metal cutting, and contact mechanics problems.

In implicit analysis, solution of each step requires a series of trial solutions (iterations) to establish equilibrium. In explicit analysis, no iteration is required as the nodal accelerations are solved directly. In explicit analysis, the time increment has to be small with no requirement for iteration or convergence checking. On the other hand, iteration and convergence checking are required in implicit analysis and the time increment can be large after achieving convergence.

Implicit FEA analysis is performed by using a numerical solver that inverts the stiffness matrix. The inversion may be only once or several times which defines the cost of the overall operation. Explicit analysis, however, does not require this step. Explicit analysis can easily handle nonlinearities including those due to contact and material. [37]

2.1.1 Material formulations

Lagrangian, Eulerian, and newer Arbitrary Lagrangian-Eulerian (ALE) are the three basic numerical formulations used in finite element simulations of metal cutting. In modeling processes with little deformations, Largrangian approach is usually used. The mesh used in the Lagrangian approach the mesh is given in Figure 2.8 which shows that the mesh is attached to the material. When the cutting tool moves on the workpiece for machining process, the deformation the material undergoes follows the mesh which results in the simulation of the chip formation. To obtain finite element solution, the displacement increment of the tool or workpiece should be defined in advance. In an explicit approach, the time step defines the displacement increment of the mesh which is related to the material removal rate. In an implicit formulation, stability of the solution has no effect on the time step which has no physical significance. Lagrangian method suffers from mesh distortion because of the plastic deformation in the cutting zone which may result in the failure of the model. The model should therefore be inspected for large deformations and changing material properties. Pre-distorted meshes and re-meshing techniques can overcome mesh deformation. This method also takes more time to reach steady-state conditions. Separation mechanism is needed to separate the chip from the workpiece. [19][15]

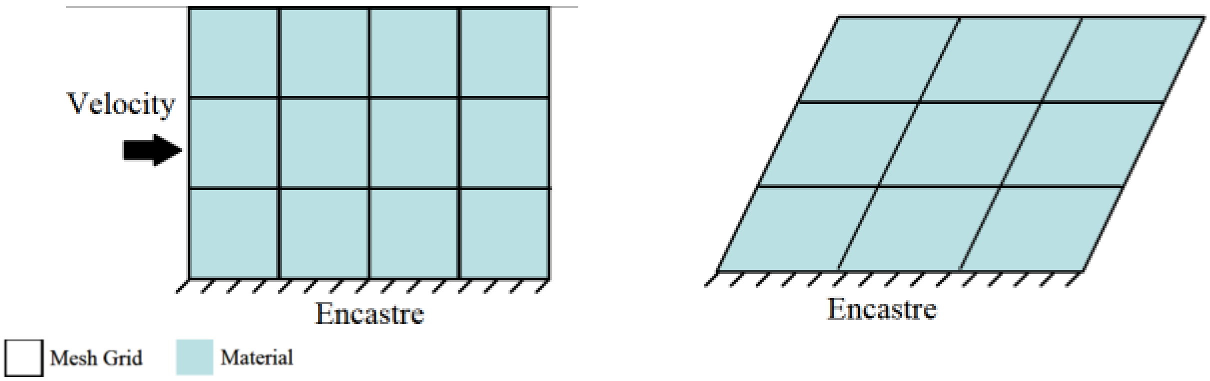

(a) (b)

Figure 2.8 – Lagrangian formulation. (a) initial position (b) deformed mesh [38]

In the Eulerian formulation shown in Figure 2.9, the workpiece material is assumed to pass through a finite element mesh which is spatially fixed over a control volume. From the Eulerian viewpoint, one point in apace is picked and the phenomena occurring at that point is analyzed. Convergence of variables is performed by an iterative procedure which has three cycles. Viscoplastic equations are solved for velocity and strain-rate distribution in the chip and workpiece in the first cycle. After determination of velocities and temperature dependence of both workpiece and material properties, temperature is calculated in the second step. The chip geometry is determined and updated until the computed velocities on the chip surfaces are parallel to the free surfaces. Since the chip formation occurs due to material flow, the shape of the chip, shear angle and the contact conditions must be predicted based on experiments or assumptions in advance [19][15].

For Eulerian models, the chip parting criteria occurs at the stagnation point at the tool tip. There is no chip distortion and no chip separation criterion and hence re-meshing is required. Eulerian formulation is suitable for the simulation of steady-state cutting with continuous chip formation. A shorter computational time than the Lagrangian formulation is required because less number of elements is needed to model the workpiece. This method is not suitable for discontinuous chips as strains are derived from the integration of strain rates along stream lines. It lacks the physical assumption of the chip thickness and the whole outcome of the cutting process. Difficulties corresponding to actual deformation procedure in metal cutting process can be expected.[19][15]

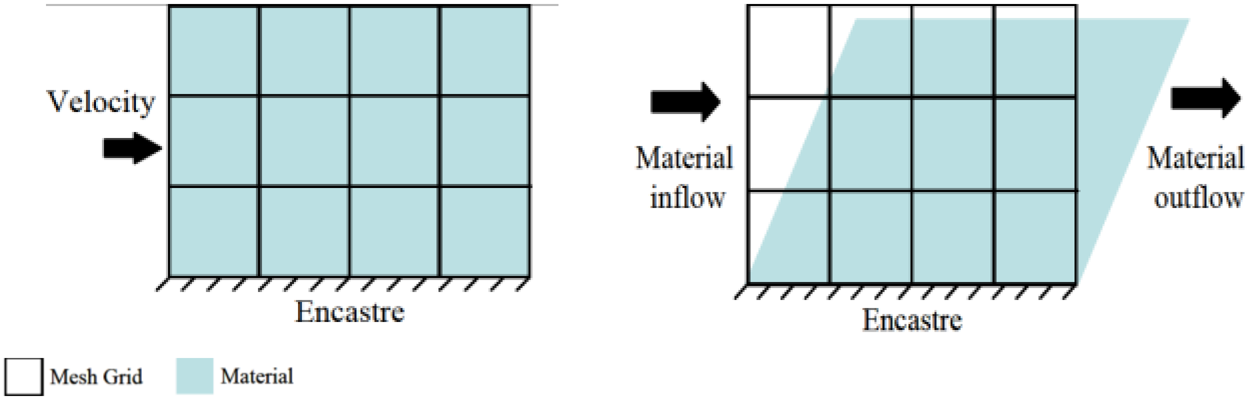

(a) (b)

Figure 2.9 – Eulerian formulation. (a) initial position (b) final position of mesh grid [38]

The mesh in the arbitrary Lagrangian-Eulerian formulation shown in Figure 2.10 is neither fixed nor attached to the material. This approach is rather based on the arbitrary movement of the mesh relative to the material with the total displacement. The total displacement is the sum of a Lagrangian displacement increment and an Eulerian displacement increment. Material flows first at the free boundaries in a Lagrangian step causing mesh displacement. The mesh displacement results in material deformation followed by chip formation. The distortions are then compensated during deformation because of the repositioning of the reference system in an Eulerian step. The ALE formulation has less distortion compared to Lagrangian mesh which means that neither extensive re-meshing nor any separation criterion is required. However, complete re-meshing must be applied for the case of inaccurate re-mapping of state variables.[19][15]

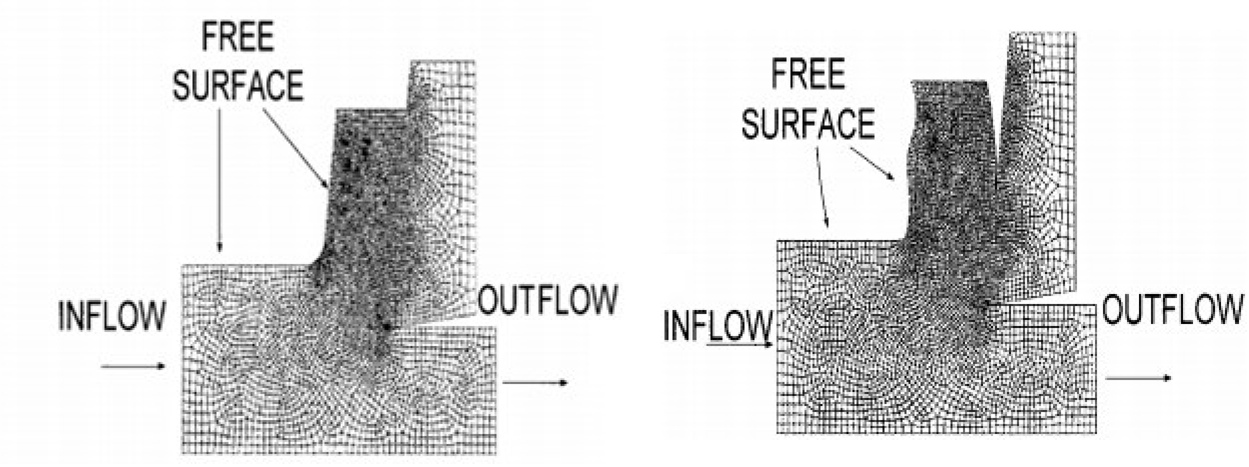

(a) (b)

Figure 2.10 – Arbitrary Lagrangian Eulerian approach (a) undeformed shape, (b) deformed shape

Material properties of both workpiece and tool are important to describe plastic deformation of the work material [13]. The workpiece material flows plastically in the cutting zone because the plastic strains are much bigger than elastic strains in metal cutting. The material properties can be defined by several different models such as rigid perfectly plastic, rigid plastic, elastic perfectly plastic, elasto plastic, thermo elastoplastic, thermos viscoplastic, and viscoplastic [13].

In the rigid perfectly plastic model, no strain occurs until the equivalent shear stress reaches the yield strength, σ_y, of the material and then the plastic flows. Plastic strain is so large in this model so that elastic deformation and work-hardening are neglected. Although elastic strain is also neglected in the rigid plastic model, work-hardening is considered as shown in the work by Iwata et al. [39]. Similar to the rigid perfectly plastic model, there is no work-hardening in the elastic perfectly plastic model. However, this model includes elastic strains and therefore a combination of elastic and plastic strains occur after yielding as adapted by Komvopoulos and Erpenbeck [40].

Unlike the other models described above, elasto plastic material model allows for elastic strains, plastic flow at the yield strength and includes possibility of work-hardening and plastic strain-rate dependency [41][42][43][44]. It can be said that this model is a combination of the above three models. thermo viscoplastic material model [45] [46] [47], Thermo elasto plastic model [48], and rigid viscoplastic [49] [50] are also other material models.

Although the above material models can be used for both workpiece and tool, most authors have assumed the tool as a rigid body extremely harder than the workpiece [46], [51], [52], [53].

2.1.2 Criteria for chip separation

It is generally considered that only plastic deformation occurs during chip formation and that there is no fracture [15]. However, it was argued that cracks cannot be observed in laboratory tests because they are suppressed due to compressive stresses in the tool edge or cracks moves as the same speed as the tool [15]. Therefore, chip separation criterion is another crucial aspect in finite element of metal cutting. One chip separation technique is to predefine a chip separation plane and apply separation criterion called node-splitting technique as described in Figure 2.11 [e.g., [17][39][41] [40]].

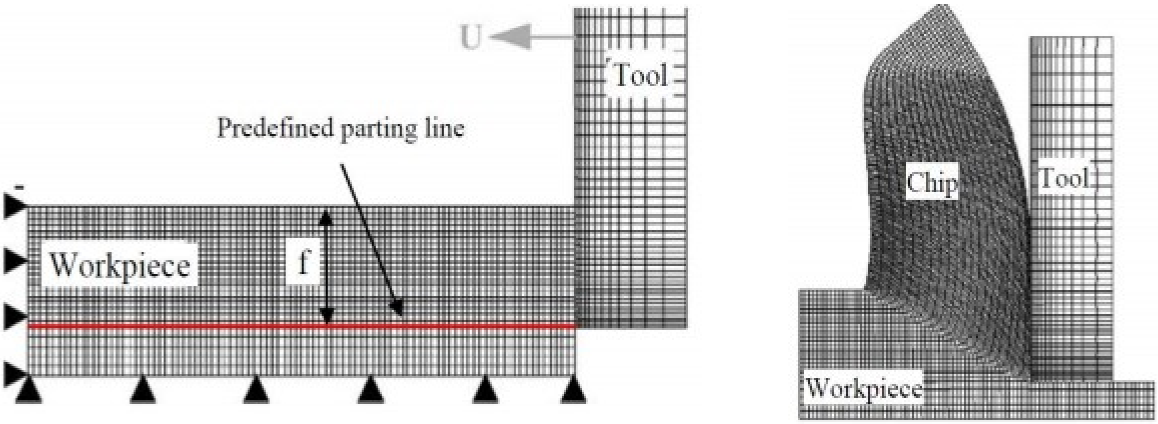

(a) (b)

Figure 2.11 – FE cutting model applying Lagrangian formulation and predefined parting line separation (a) initial boundary condition and geometry (b) continuous chip formation [38]

There are geometrical and physical types of separation criteria. The geometrical criterion is based on a critical distance *D* between the tool tip and the node *a* located immediately ahead as shown in Figure 2.12. As the tool progresses, the distance between the tool tip and the node ahead decreases. When the distance is less than a critical value, the two nodes separate from the workpiece material and flows along the tool rake face. Determination of the critical distance is important as it can cause wrong separation time for the two nodes ahead of the tool due to choosing too small distance. If the nodes do not separate at the right time, serious mesh distortion and convergence problem will occur as it was observed by Komvopoulos et al.[40]. In the case of having too large distance, an opening gap creates in front of the tool tip which alters the real physical behavior. The value of the distance can be obtained by trial and error [13]. Some other authors proposed chip separation criterion based on the critical distance. The work by Zhang et al. [54] has shown that the distance should be 10 to 30 percent of length of an element. Although this mechanism is simple to control and can be applied for the tools with round edge, it has no physical meaning and the breakage outside the cutting line cannot be accounted for.

The physical separation criteria are based on value of physical properties, such as stress, strain, or strain energy in the elements or nodes immediately ahead of the tool tip. The critical values of the nodes' physical quantities are used to estimate the separation and the nodes separate, when the magnitude of the controlled variable in an element is larger than the critical value. Applying physical mechanism can result in an undesired event where node separation may be faster than cutting speed leading to chip formation before the tool has reached.

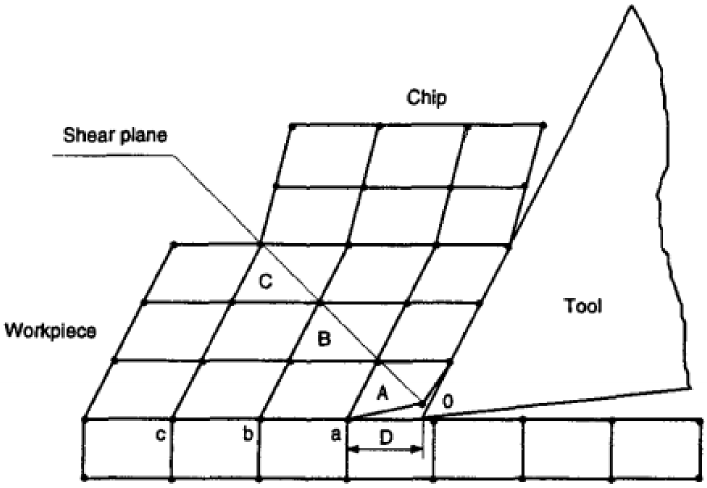

Figure 2.12 – Geometrical separation criterion of chip formation[55]

Haung and Black [55] proposed a method of combination of both geometrical and physical criteria since the result of either method were not completely satisfied. The reason was that the effect of friction at the chip-tool interface, and effects of strain rate and temperature on the material properties were neglected. A chip separation criteria developed by overcoming mesh distortion using a trial and error method was proposed to identify the physical properties of the material under machining.

A continual periodic re-meshing technique between displacement increments of the cutting tool was proposed by Madhavan [56] to avoid extreme mesh distortion and inability of convergence of the solution to an equilibrium stress state. The work also argues against the point of arbitrary separation criteria in finite element simulations of machining processes which has no real material behavior representation in the deformation zones. The similarity between work material deformation in metal cutting and indentation of ductile metals was used to replace the stress and strain fields of the old mesh as an initial condition of a new mesh. Satisfactory experimental results have only been only observed in simulations of ductile materials.

Shi et al. [42] proposed stress-based chip separation criterion using ABAQUS. When the stresses along the cutting path reach a critical value of a combination of shear, normal stresses and failure stresses under pure tensile and shear loading conditions, in front of the tool tip, chip separation occurs. This method is shown in Figure 2.13 where the cutting path in workpiece is defined by the contact pair 1. After a separation criterion is met and while the tool moves, the pair of finite elements above the contact surface immediately before the tool tip separates and moves into contact pair 2. The finite elements below the contact surface moves into contact pair 3.

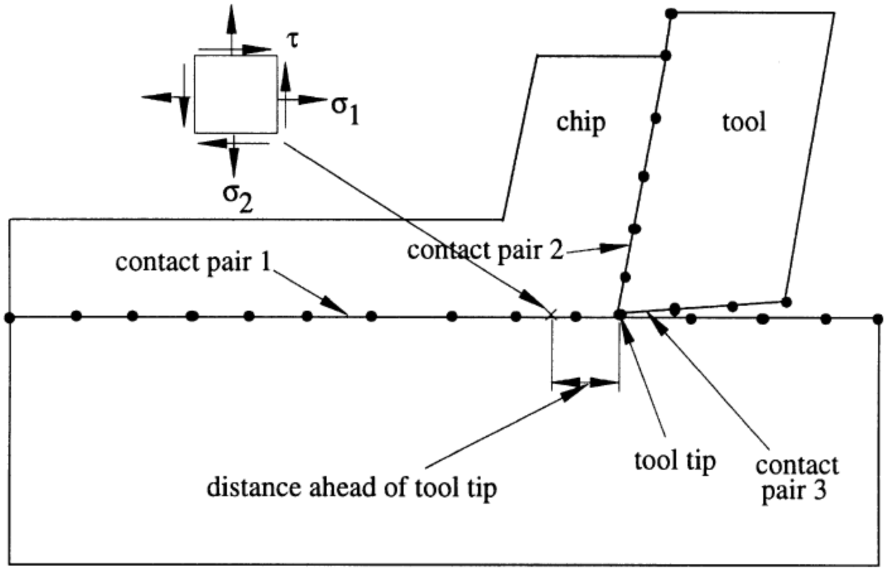

Figure 2.13 – Chip separation by Shi et al. [42]

Johnson-Cook plasticity and damage model with element deletion technique is gaining popularity to be often applied as separation criteria to finite element simulation of cutting [e.g., [57], [58], [52], [59], [60], [61]]. It considers the separated effects of strain hardening, strain-rate (viscosity) and thermal softening. Itis a relatively simple model and defines the general response of material deformation. [61]

2.1.3 Friction model

Friction is a crucial phenomenon in metal cutting which is very complex to model. It has a significant effect on the amount of power required for removing a given volume of metal, surface quality of the finished product, and the extent of tool wear. However, many studies assume no friction in the metal cutting process due to lack of experimental techniques to directly measure the coefficient of friction.

Sticking and sliding regions are the two contact regions along the tool-chip interface. A critical friction stress τ_c and coefficient of friction μ are assumed to exist in the sticking and sliding regions, respectively[42]. Most analyses have applied classical friction situation following Coulomb's laws which is based on coefficient of friction [e.g., [55], [62]]. Frictional sliding force F is proportional to the force N normal to the interface at which sliding is taking place. This model can be expressed by:

$$F = \mu N , \tau = \mu \sigma \tag{2.19}$$

where, τ is the frictional, and σ normal stresses.

However, the above equation fails to give accurate prediction in high normal stress conditions. Several studies applied modified Coulomb friction law [e.g., [42], [40], [63],[41]] in which critical friction stress depends on pressure normal to the tool-chip interface, coefficient of friction, and threshold value for the conventional Coulomb friction stress. In this model the contact point is in the sticking region and there is no relative motion between the chip and rake face of the cutting tool and shear stress parallel to the tool-chip interface is less than the critical friction stresses. On the other hand, if the parallel shear stress is the same or more than the critical value, the contact point is in the sliding region and the relative motion occurs between the chip and the tool.

Another model is Zorev's stick-slip temperature independent friction model [64] in which sticking occurs near the tool edge assuming the shear stress be constant and equal to maximum shear stress of the material, and sliding takes place beyond the sticking region at the interface where normal and shear stress decreases to zero and coefficient of friction is assumed to be constant.[15]

Followed by Zorev's model, Usui and Shirkashi [65] proposed the following empirical non-linear expression in which the sticking region occurs in high normal stress and sliding region for smaller value of normal stress.

$$\tau = k[1 - \exp\left(-\frac{\mu \sigma}{k}\right)] \tag{2.20}$$

where, k is the shear strength of the material.

Iwata et al. [39] tested various combinations of tool and workpiece materials including Vickers hardness H_v and derived with the following equation which had close approximation to Usui's model.

$$\tau = \frac{H_v}{0.07}\tanh\left(\frac{\mu\,\sigma}{\frac{H_v}{0.07}}\right) \tag{2.21}$$

There has been much investigation in this topic, such as the study of the effects of friction model by applying arbitrary Lagrangian-Eulerian approach which concluded that thrust forces have more influence on friction more than cutting forces. Some other parameters such as contact length and thermal properties have also been studied to understand their relation to the friction model.[15]

2.1.4 Mesh consideration

Another crucial aspect that affects simulation results is finite element selection. It is important that the mesh represent the workpiece geometry in an accurate way to obtain reasonable numerical convergence and variables prediction. Size, number, and type of elements used in the mesh determine the mesh properties. Having larger number of small elements is often desired to obtain better results. However, this way is time consuming, which makes coarser mesh preferable usually for the first step to check the model after which finer mesh can be used for final results. There are some cases where the region of interest is a small part of the model, and it is possible to use both fine and coarse mesh for the primary and other regions, respectively. Since primary and secondary deformation zones are the main area that should be investigated in metal cutting simulations, finer mesh is suitable. Modeling large workpieces is preferred to avoid the effect of boundary conditions on the physical behavior at the deformation zones during simulation of cutting process.

Eight-node trilinear coupled temperature displacement elements [57], four nodes thermal coupling plane strain quadrilateral element [66] [52] [55] four-node plane strain elements[42], 4-node bilinear plane strain quadrilateral[67], linear quadrilateral elements [63] are some of the elements that have been used in different researches to study chip formation.

2.5 Influence of process parameters and tool geometry on mechanics of machining

Parameters such as cutting speed, feed rate depth of cut, and tool material geometry including rake angle, relief angle, number of teeth, cutting edge radius, and cutter width significantly affect the machining operation, quality of finished products, and tool life. Therefore, selection of these parameters is the determining factor for the overall manufacturing cost. A good number of researches have studied about the effect of input variables and process behavior for many decades.

Sarwar and Thompson [68] discussed the process of metal removal at saw blade's tooth tip with very large cutting edge radii (0.405mm). Optical comparator was used to measure the radius on a tooth. The rake angle was 4 degrees while the flank angle was 38 degrees. A dynamometer was used to measure cutting and thrust force. Results showed transient cutting and thrust forces because of discontinuous chip formation. At prescribed depth of cut in steel cutting, the steady state cutting forces were slightly higher than the steady state thrust forces. The cutting and thrust forces became similar by decreasing the depth of cut per tooth. It was also concluded that thrust force occurs before the creation of a chip. The thickness of the workpiece and the pitch of the sawblade have also been seen to influence cutting and thrust forces.

Iwata et al. [39] adapted a rigid-plastic finite element model with an Eulerian formulation to simulate steady-state orthogonal metal cutting. The elastic deformation and temperature rise due to friction have been neglected. The latter one was because of the approximate prediction of the friction conditions on the numerical analysis. A micro-scale cutting experiment with a scanning electron microscope has also been included to compare the results with numerical predictions. Predictions of chip shape, contact length between chip and tool, distributions of strain rate, stress, and equivalent strain have shown a good agreement with the experimental results.

Komvopoulos and Erpenbeck [40] applied constitutive material behavior models and interfacial friction mechanisms close to real application scenarios for metal cutting simulation of AISI 4340 steel with ceramic-coated tools. An assumption has been made to take the tool material and the built-up edge to be perfectly rigid. Both elastic-perfectly plastic and elasto-plastic constitutive models with isotropic strain hardening and strain rate sensitivity material behavior, realistic contact modelling, built-up edge formation at the tool tip and crater wear have been covered investigated. They discussed the influence of interfacial friction, metal flow characteristics, and wear at the tool rake face on the cutting forces, shear plane angle, chip thickness and chip-tool contact length.

Zhang and Bagchi [54] presented an updated Lagrangian formulation with adoption of true stress-strain curve for large deformation simulation of low speed orthogonal cutting. Low cutting speed machining includes small inertial effects, which has been the reason to apply a quasi-static analysis procedure. The chip separation was conducted based on developed conditional two-mode link elements. For sliding and sticking regions, constant coefficient of friction and constant frictional stress were used. While the effect of temperature was ignored, the study compared the results from experiment and finite element model for forces, shear angle, and plastic deformation. There was no limitation for friction coefficient during steady-state cutting; however it had to be kept below 0.4 to avoid non-continuous chip formation during incipient cutting.

Marusich and Ortiz [44] developed an up-dated Lagrangian formulation of orthogonal high speed machining accounting for fracture mechanism to overcome the limitation of predetermined line separation mechanism. In the previous method, when tool tip was close enough or certain level of some physical data was reached, the immediate nodes ahead of the tool tip would be separated. Although the initial method was simple and had advantages, it was not capable of surface roughness prediction and account for fracture. The method predicted different types of chip morphology, such as continuous chip, shear localized chip with and without complete chip detachment.

Tool rake angle influences the performance of the cutting tool and the surface integrity of the workpiece [15]. Shih [69] observed the effects of the rake angle on the finite element mesh, temperature, plastic strain, plastic strain rate, effective stress, yield stress and hydrostatic stress and chip morphology. Large element distortion was noticed under cutting simulation with small (zero or negative) rake angle. Therefore, the tool-chip interface was assumed frictionless at the first stage, and then gradually restoring the desired cutting conditions until the steady-state chip formation was achieved. The larger the rake angle, the larger the cutting, feed and resultant forces observed. Smaller rake angle resulted in smaller shear angle and longer contacts length.

It has also been reported that unreformed chip thickness has an effect on cutting coefficients [70]. It should be noted that the feed rate defines the uncut chip thickness in orthogonal metal cutting. The ratio of undeformed chip thickness to cutting edge radius also has a significant influence on the cutting coefficients, especially in the case of larger cutting edge radius than undeformed chip thickness [71]. Another factor that plays a significant role in machining is cutting edge radius. It is common that in the case of having a perfect sharp edge, there is no ploughing and the shear force resulting from the interaction between the sharp tool and workpiece forms the chip because there is no contact between the cutting tool and workpiece along the clearance face as shown in Figure 2.14 (a). By increasing the cutting edge radius especially as compared to the undeformed chip thickness, chip separation becomes difficult due to the prevailing negative effective rake angle as shown in Figure 2.14 (b). Although cutting speed has a considerable effect in tool life in slotting process using circular saw blades, changing the cutting speed does not have a comparable influence on cutting forces as tooth edge radius and feed rate. However, all process parameters and tool geometry should be chosen to increase machinability and minimizing cost.

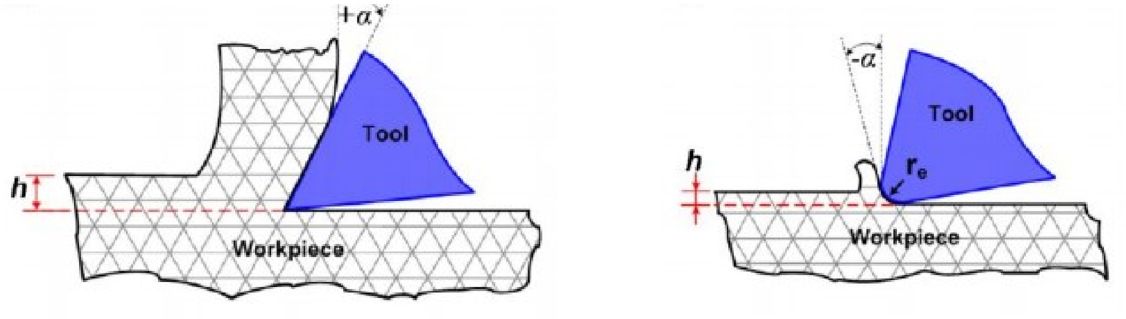

(a) (b)

Figure 2.14 – Considering cutting edge in cutting process[38]

The effect of tool edge geometry was also studied by Lei Wan et al. [72] in orthogonal metal cutting. They adopted ALE approach for simulation in ABAQUS/Explicit and considering P20 as the workpiece material. The input variables were taken as the angle and length of the carbide tool along with different cutting speeds. It was shown that cutting forces increase chamfer angle increase and cutting speed decrease. However, during machining at very high cutting speeds, the effects of tool edge geometries were not significant on the chip removal process and cutting force.

Awadhesh Pal et al. [73] experimentally observed that cutting forces increase with the increase in both depth of cut and material hardness of the workpiece. Analysis of variance (ANOVA) was used in the analysis of data for AISI 4340 steel and TiC mixed alumina ceramic as workpiece and tool, respectively. It was also showed that higher values of the workpiece hardness resulted in a decrease in the surface roughness.

2.6 Dynamics of metal cutting

One of the significant factors that significantly influence tool wear, material removal rate and surface finish is vibration [12]. Energy is transformed two-way between kinetic and potential during vibration untill all the energy is lost through damping [74].

Displacement, velocity, acceleration and frequencies are vibration's components and they can be measured in the time domain, or frequency domain, or just a single number for total vibration.. Generally, stress is the failure mode which causes displacement. Velocity is related to the fatigue mode and measures how often the displacement is being applied in a given time period. Above the 2000 Hz the failure is normally force related. Acceleration meassures of the likelihood of force being the mode of failure[74].

There are three general categories of mechanical vibrations:

1- Free vibration: when a body is disturbed from its equilibrium position and there is no long-term external force acting on the system.
2- Forced vibration: unbalance rotating that forcing frequency is equal to the system's natural frequency (resonance). When the excitation stops, the vibration acts similar to free vibration and ends due to damping. In machining, forced vibration can be due to unbalanced spindle (bearing), spindle run-out, improper torque for circular blade make-up, and pipe clamping.
3- Self-excited vibration: is caused by a long-term external force leading to a steady excitation for vibration to occur near the natural frequency. Chatter in milling is one example for self-excited vibration which occurs when the teeth impacting the workpiece causes the steady forced excitation. Since cutting force is proportional to the chip thickness, the variable chip thickness causes viriation in the cutting force which affects the tool vibration called regeneration waviness.

Forced vibration is also referred to as the Frequency Response Function (FRF) to describe the response of a system to different excitation frequencies. The FRF can be measured and the results can be used for performance prediction. There is a very strong correlation between the FRF and the level of speed and power used in milling operations.

Since single degree of freedom systems have one natural frequency, we have 80 natural frequencies for the case considered in this study – one for each spindle. Each natural frequency has a corresponding characteristic deformation pattern (mode shape). Vibration in this thesis (with multiple degrees of freedom) can be assumed as the sum of vibrations in the individual modes (80 spindles). The RPM that would excite a specific forced (impact) vibration frequency is thus calculated as:

$$Hz = \frac{RPM * N}{60} \tag{2.22}$$

where, N is the number of teeth of the cutter.

On the other hand, self-excited vibration is dependent on the revolutions per minute (RPM) of the spindles and the depth of cut during the cutting process. The louder noise generation at greater depths into the cut is also attributed to this relationship. A quick remediation can be changing the RPM by maintaining the feed rate as a constant variable leading to a linear change in the velocity and forces during the cutting process. Chatter is more similar to a piercing chirp because it is usually a higher frequency and less mass, while forced vibration is more of a shaking condition due to the lower frequency which comes from components of the machine tool structure.

2.1.5 Chatter and regenerative effects

Regeneration of waviness refers to the phenomenon that causes a steady input of energy from a spindle drive into vibration at the cutting edge. A specific wavy surface on the workpiece results when a cutter makes a pass. The cutter removes material from this wavy surface in the subsequent pass leaving behind a new wavy surface. The chip that is created by this cut carries both the waviness from both passes. If the new cut leads to a chip with variable chip thickness (i.e. out of phase waves), this would translate as variable forces on the cutting edge and eventually as vibration. These vibrations are unstable and provide a net negative damping to the system which results in energy which cannot be dissipated. If the waviness of the chip is in phase, it creates a stable cut as shown in the Figure 2.15 (a) where the vibrations may decay due to the contribution of a net positive damping to the system.

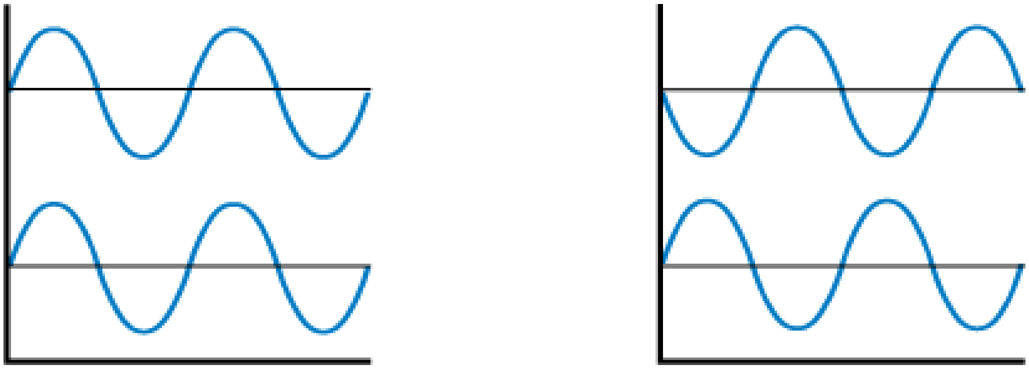

(a) in phase (b) out of phase

Figure 2.15 – Waviness phase

Chatter is the associated loss of dynamic stability which can be created by either regenerative instability mentioned in the previous paragraph. Irregular interactions between workpiece and tool are also causes for driven oscillations that ultimately result in chatter [75]. The stability analysis for the first case is similar to turning process where at least one flute of the tool is engaged with the workpiece at all times. In Figure 2.16the cutting force of the tool depends on the time delay between the tool position $x(t-\tau)$, $x(t)$, feed rate and spindle period. The latter source of chatter occurs when some of the cutting edges are not engaged with the workpiece for a long time as shown in the Figure 2.17. [75]

By obtaining the stability lobe diagram similar to the one shown in the Figure 2.18, it is possible to predict the proper values of spindle speed (RPM) and axial depth of cut to machine efficiently while producing higher quality of products.

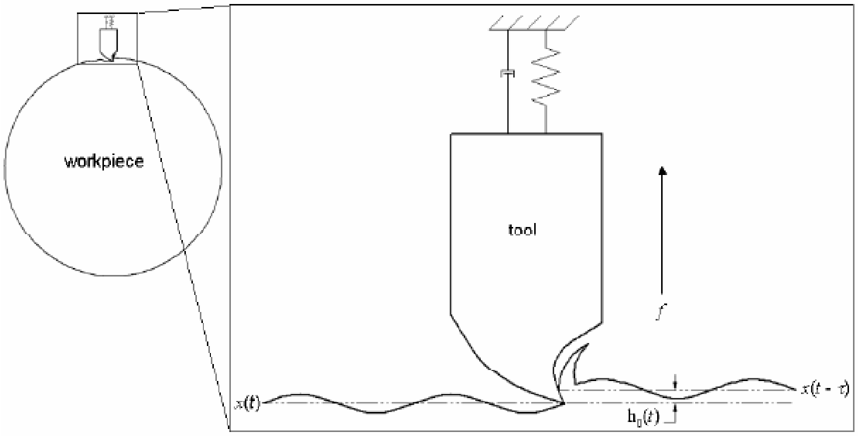

Figure 2.16 – Regenerative effects in turning [75]

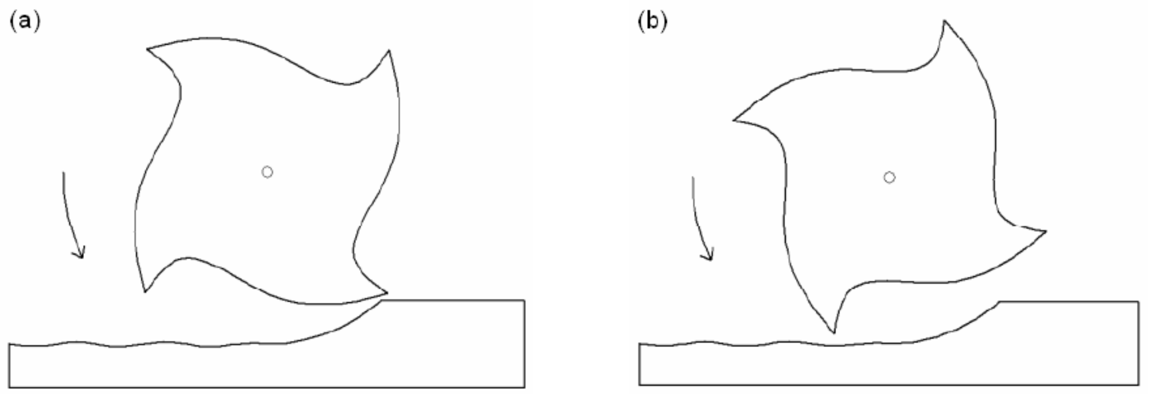

(a) in phase (b) out of phase

Figure 2.17 – Regenerative effects during low immersion cutting [75]

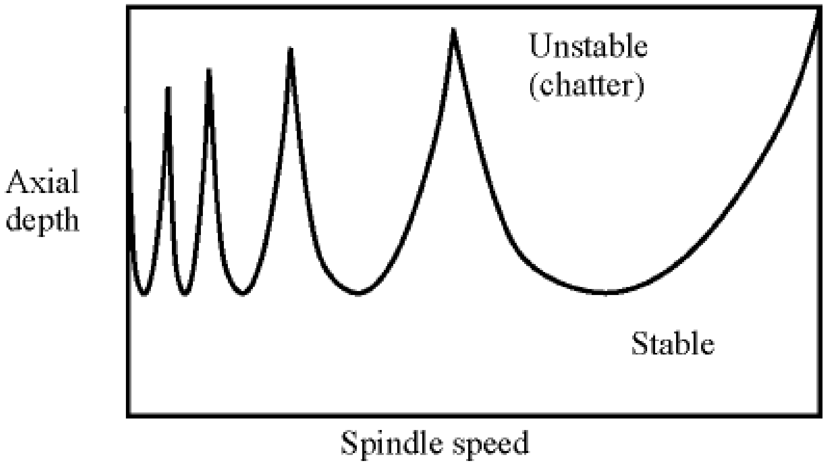

Figure 2.18 – Stability lobe diagram

Early studies including that of Sridhar et al. [76] developed the general formulation of equation and stability algorithms in milling process. Other studies [77] have followed to apply a single degree of freedom structural model to investigate the forced vibration and chatter in horizontal milling process. Altintas [78] developed a model in orthogonal cutting process to predict the radial and axial depth of cut in peripheral milling. Tasi et al. [79] adopted lumped-parameter model to predict a chatter vibration in a two degree of freedom end milling operation. The first non-linear system was studied by Tlusty and Ismail [80]which used a computer simulation to analyze the basic non-linearity in machining chatter for the case of a severe chatter. In this case the cutter is not in contact with the workpiece for the entire process. Smith and Tlusty [81] had a comprehensive overview for various developed models of the milling process. It was confirmed that the regenerative force, dynamic deflection model is a proper method to simulate the milling system in the transient response.

Clancy et al. [82] developed a chatter frequency model for face turning processes. The three dimensional model of this work included the effect of tool wear and process damping as well as nonlinear tool geometries like nose radius. Process damping model was developed based on the slope change along the cutting edge of a tool for tool flank wear simulation. Therefore, the magnitude and direction of the process damping force can be predicted as validated by experimental results.

Solis et al. [83] developed a chatter prediction using combination of analytical model for chatter vibration prediction in milling (referred to [12]), and experimental multi-degree-of-freedom systems modal analysis. The value of natural frequency, damping factor and stiffness of the mechanical system were obtained from the experiments. Chatter frequency was calculated from the transfer function for all dominant modes.

Jin et al. [84] recently proposed the 3D stability lobe in thin-wall milling using higher order time domain. The force model was based on the helix angle effect and run-out effect of the cutter. Computer simulation along with impact experiment was used to obtain the effective stiffness of the thin-walled part followed by experimental validation.

2.7 Concluding remarks

The review of literature for this research has shown evidence for existing techniques that can be used to solve the problem at hand either analytically or numerically. The methods selected from the review, however, propose to use the combination of these two approaches to solve RGL's case. It is believed that analytical solution and numerical simulation not only supplement each other but also give confirmed results for shape optimization when combined.

As it will be discussed in the following chapter, analytical methods are used to perform force analysis. Determination of the force distribution could perhaps be best achieved using experiments. However, given the possible interruption of production time and other required resources along with the difficulty posed by the machines configuration, it was too costly to run the required number of experiments for the study. Therefore, predictive analytical models were developed to be solved and identify the distribution of forces during the slotting process.

3. METHODOLOGY

In view of the reviewed relative theories, the methodology of this study can be summarized in Figure 3.1. After defining the problem as orthogonal cutting process, the cutting parameters along with geometries and material properties of both workpiece and pipe are used as input variables. All input parameters are applied in both numerical and analytical studies. The results from both methods are used for dynamic stability analysis and shape optimization. Finally, the overall results are the optimal values of blade geometries for an improved operation.

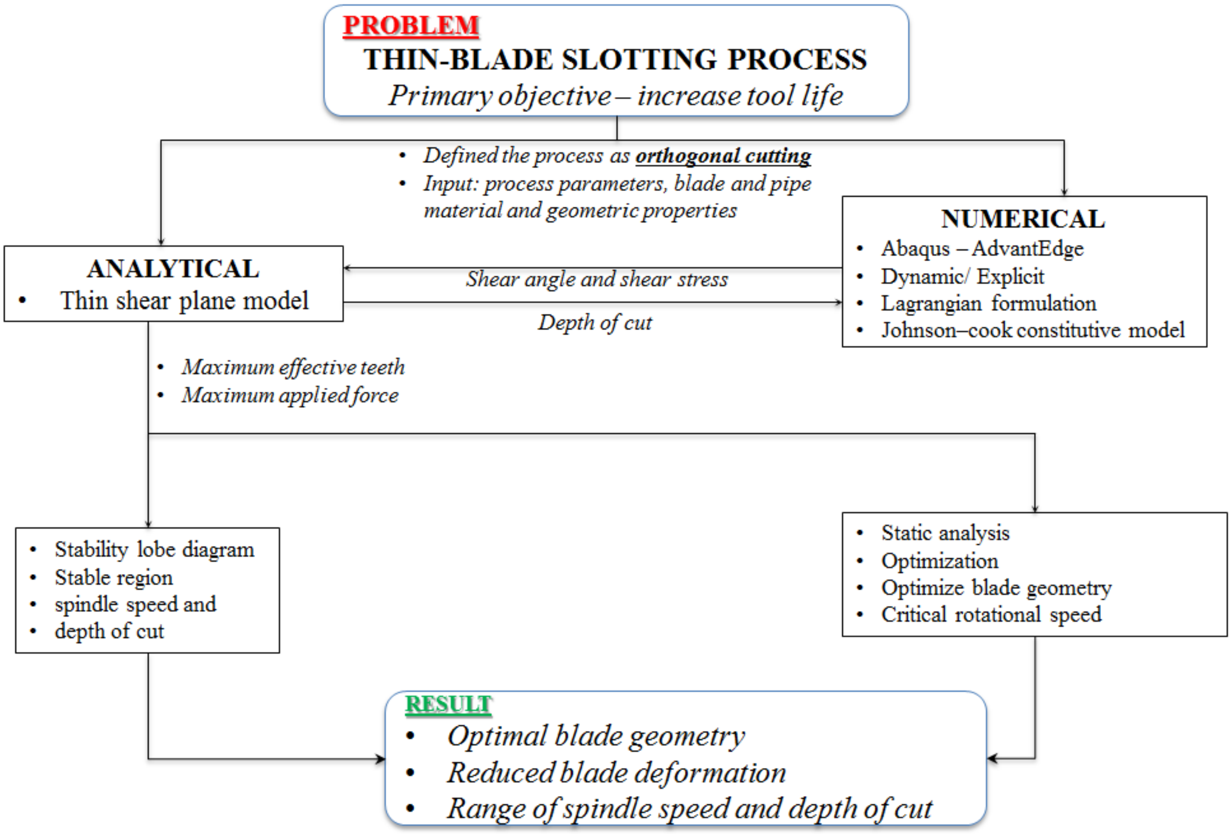

Figure 3.1 – Summary of the methodology

3.1 Orthogonal cutting in slotting process

In this section, the mechanism of the slotting process using circular saw blades for as applicable to the manufacturing of slotted liners for SAGD operations is explained. A mathematical model for the number of teeth that involved in is given as a function of time. In addition, models for calculating the components of the resultant force for each tooth are developed as a function of time, and tooth index on the basis of orthogonal cutting theory. A mathematical model for calculating the force components in circular saw blades as a function of time via summation of relevant force components of all teeth is obtained. The results for number of effective teeth, the force components of individual tooth, and the force components of overall circular saw blade are then computed in MATLAB to get a comprehensive expression. It should be noted that the shear angle for the analytical model is calculated by numerical method using finite element simulation. The force calculated from the mathematical model along with the process parameters and tool geometries are used for dynamic stability analysis of the machine operation.

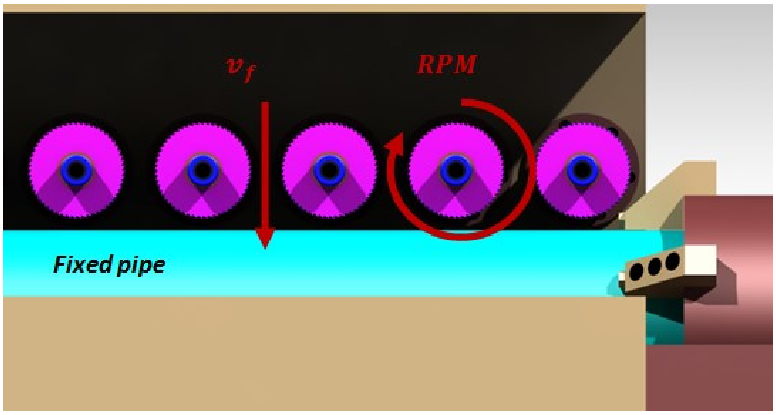

Figure 3.2 – Movement of the blade and pipe

The working mechanism of RGL's customized multi-spindle slotting machine is illustrated in Figure 3.2. To make the slots on the pipe, multiple high-speed circular steel saws cut into the pipe. The multi-spindle slotting machine simultaneously creates the number of slots required along the length of the pipe (typically 80 slots, since it has 80 spindles). With the indexing machine (chuck), all the slots are created in the same way. The workpiece (pipe) is fixed by the clamp for the circular saw blades to slot into the pipe with a downward feed to the pipe.

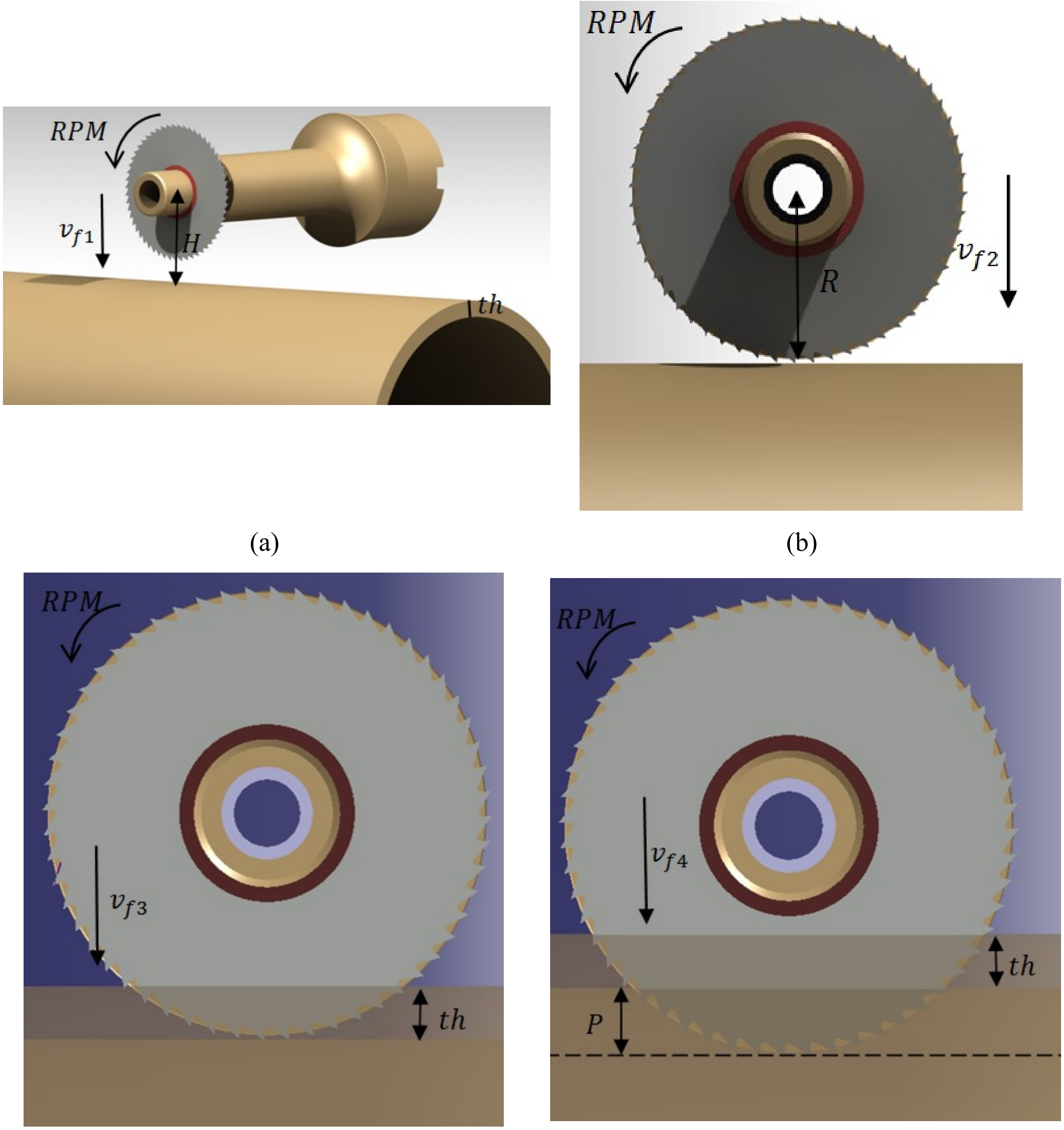

(a) (b)

(c) (d)

Figure 3.3 – Different phases of a complete slotting

Figure 3.3 gives a closer look at each phase of the slotting process. The blade starts from the original position with an initial feed rate of v_{f1} and finishes at the moment when the circular saw blade just reaches the workpiece. At this time the feed rate reaches Outer Diameter (OD) v_{f2} from v_{f1}. During the next phase, the circular saw blade just breaks through the workpiece with an outer diameter (OD) feed rate of v_{f2}. The blade then starts cutting until the blade touches the inner surface of the pipe where the feed rate changes to an inner diameter (ID) feed rate of v_{f3}. Finally, the blade reaches a defined plunge distance where the final feed rate is v_{f4} and, at this time, the slotting process completes. After finishing cutting the first row, the spindles return to their initial position with a fast feed rate.

It can be noticed here that the multi-spindle slotting machine has a similar process to horizontal milling machine and that is the main reason for the model to follow the milling process. However, the machine tool is not atypical milling tool. Therefore, during the whole slotting process, the teeth of the circular saw blade are not always cutting on the workpiece that there is no contact with the workpiece during some time period. Thus, the effective cutting/slotting time period is the time that the circular blade teeth have a contact with the workpiece which depends on the number of the teeth. It is also important to know that feed rates are gradually changing (increasing or decreasing) i.e. the blade starts the process with v_{f1} and its feed rate at positions (b), (c) and (d) in Figure 3.3 are v_{f2}, v_{f3} and v_{f4}, respectively.

3.2 Blade geometry

A typical circular saw blade used in RGL's slotting machine is shown in Figure 3.4. The blade's bore dimeter (*d*) is already fixed and selected based on the arbor diameter. The diameter of the blade (*D*) must be selected to meet the required slot length and to prevent clash between the bore and workpiece. The blade thickness (*W*) is very small (0.02 ~ 0.04 in) and it is selected as per specifications provided by the clients as the desired slot width. The number of teeth should be optimum since it affects tool life and resonant frequency of the machine. Having more teeth leads to smaller tooth pitch and gullet area. The gullet fills up rapidly with chips and increasing surface contact which generates more heat. Having less than the required number of teeth also affects the tool life because of the tooth-load since teeth will keep contact with a workpiece for a longer period of time. In addition, having a thin blade requires more number of teeth to compensate the loss in blade width and minimize the machine vibration.

In this study, a blade with 56 teeth is selected as it is the most common one used by RGL and gives a better tool life. The rake angle (α) is typically positive. It should be noted that the relief angle (Υ) decreases as the rake angle increases to maintain the material angle on the blade. The values of rake and relief angles vary and will be defined later in the chapter.

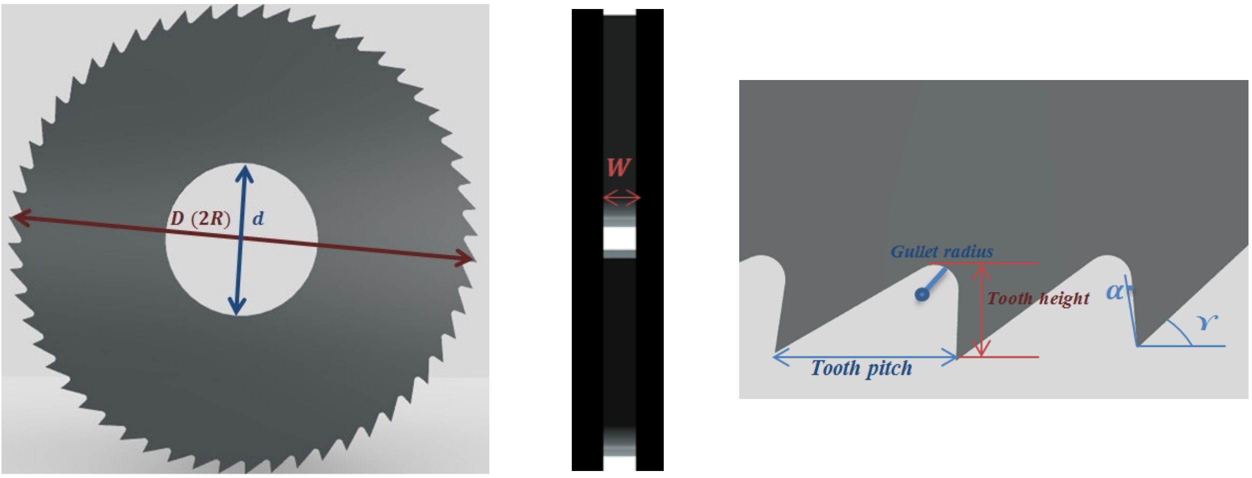

(a) Front (b) Right (c) Teeth

Figure 3.4 – Geometry of the blade

3.3 Coordinate system

The coordinate system should be defined first so that the key time points can be described and each tooth can be positioned at a given time point. Some parameters such as angle per tooth are measured with reference to the centre of the circular saw blade, while others such as the feed rate are measured based on the space transformation of the circular saw blade. Therefore, a single type of coordinate system cannot express all these parameters simultaneously. Two types of coordinate system, namely global coordinate system and local coordinate system are employed in this study.

As shown in Figure 3.5, the downward direction is set as the positive x-axis and the rightward direction as the positive y-axis for the global coordinate system. An important feature to note here is that this coordinate system moves with time, i.e., the absolute physical position of the circular saw blade keeps changing during the slotting process. Figure 3.5 shows the starting moment (t=0) of the slotting process.

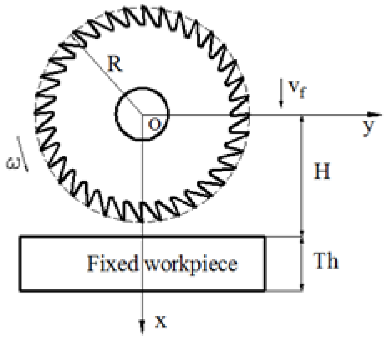

Figure 3.5 – Schematic of global coordinate system

When analysing the forces applied to the single tooth, the local coordinate system defined in Figure 3.6 is used. The *x*-axis is along the cutting direction (tangential direction of the outer circle) and the *y*-axis is the radial direction pointing to the centre of the circular saw blade. Likewise, this coordinate system is also dynamic, i.e. the origin of this local coordinate system keeps changing with time.

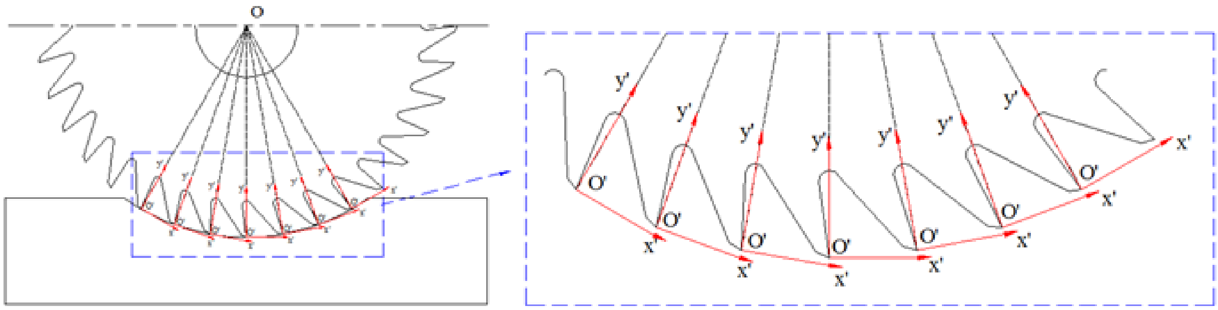

Figure 3.6 – Schematic of local coordinate system

3.4 Key time point measurement

First Touching Time of Outer Circle

At time $t = 0$, the distance between the center of the circular saw blade and the workpiece is H. When the outer circle touches the workpiece for the first time, the center of the circular saw blade travels a distance of $H - R$ (where R is the radius of the blade), thus, the first touching time of outer circle can be calculated as:

$$t_0 = \frac{2(H - R)}{v_{f1} + v_{f2}} \tag{3.1}$$

First touching time of teeth

Generally, the first touching time of teeth is different from that of the outer circle, i.e., $t_1 \neq t_0$, because there is not always one tooth that touches the workpiece when the outer circle just reaches the workpiece. Only when $t_0 = \frac{2(H-R)}{v_{f1}+v_{f2}} = m.T_{tooth}$ (where m is an integer and T_{tooth} is the time in seconds taken by one tooth to travel to the position of its adjacent front tooth), that $t_1 = t_0$ holds. Otherwise, $t_1 > t_0$, i.e., at this condition, the tooth touches the workpiece for the first time at the left hand side (LHS) of the positive *x*-axis as shown in Figure 3.7. The time per tooth (T_{tooth}) and angle per tooth (or pitch angle) (θ_{tooth}) can be calculated as:

$$T_{tooth} = \frac{T}{N} = \frac{2\pi}{\omega N} \tag{3.2}$$

$$\theta_{tooth} = \frac{2\pi}{N} \tag{3.3}$$

where, N is the number of tooth, ω is angular speed of the spindle, and T is the rotational period of the circular saw blade. The values for ω and T can be calculated as:

$$\omega = \frac{2\pi}{60\ RPM} \tag{3.4}$$

$$T = \frac{2\pi}{\omega} \tag{3.5}$$

Figure 3.7 (a) shows the locations of the circular saw blade at time t_0 and t_1, respectively, with Points O and O' as the corresponding centers of the circle. It is obvious that the time period $(t_1 - t_0)$ is less than T_{tooth}. The focus here is on the immediate tooth on the LHS of the positive *x*-axis. At time t_0, this immediate tooth is at $P_1$and the outer circle of the circular saw blade just touches the workpiece at P_3 Figure 3.7 (b) and (c). At time t_1, the circular saw blade moves and the immediate LHS tooth of the positive *x*-axis travels from P_1 to P_2. At this time point, this immediate LHS tooth just touches the workpiece at P_2. During this time period $(t_1 - t_0)$, the center of the circle travels a distance of $v_{f2}\ (t_1 - t_0)$. Drawing a perpendicular line from P_2 to the *x*-axis shows the perpendicular foot to be at P_3. The angles $\theta_0$and θ'_0 define the radial angles of this immediate LHS tooth at time t_0 and t_1, respectively.

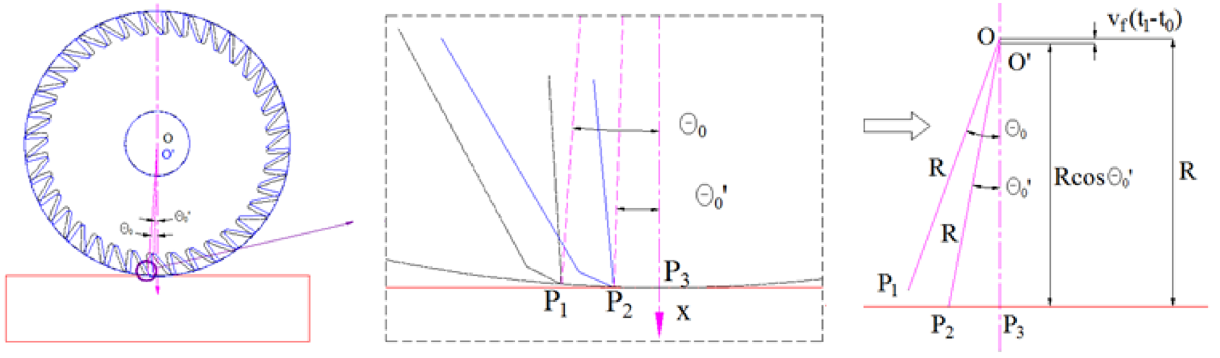

(a) (b) (c) Not proportional to (a) and (b)

Figure 3.7 – Schematic of key time points $t_1,\ t_0$

Since the line segment P_2P_3 is perpendicular to the x-axis:

$$|O'P_3| = Rcos\theta'_0 \tag{3.6}$$

Considering the change of the radial angle and by knowing that ω is angular speed of the spindle:

$$\theta'_0 = \theta_0 - \omega(t_1 - t_0) \tag{3.7}$$

Given that the center travels from O to O' within $t_1 - t_0$:

$$v_{f2}\ (t_1 - t_0) = |OP_3| - |O'P_3| = R - Rcos\theta'_0 \tag{3.8}$$

Combining (3.1) through (3.8), gives:

$$v_{f2}\ (t_1 - t_0) = R - Rcos(\theta_0 - \omega(t_1 - t_0)) \tag{3.9}$$

By solving (3.9) the first toughing time of outer circle can be calculated.

Cut-through time

When the circular saw blade cuts through the workpiece, the center of the circular saw blade travels a distance equal to Th (pipe thickness)such that :

$$t_2 = t_1 + \frac{2Th}{v_{f2} + v_{f3}} \tag{3.10}$$

End time

When the circular saw blade completes cutting the workpiece, the targeted slot length is met as shown in Figure 3.3 (d). Therefore,

$$t_3 = t_2 + \frac{2P}{v_{f3} + v_{f4}} \tag{3.11}$$

where P is the plunge distance which is the distance between the deepest point of blade and inner diameter of pipe when the blade reaches its deepest position.

$$P = R - \sqrt{R^2 - \left(\frac{L}{2}\right)^2} \tag{3.12}$$

where L is the slot length on the outer surface of the pipe.

Calculation of key time points using MATLAB

From equations (3.1), (3.10), and (3.11), t_0, t_2, and t_3 can be directly calculated. However, from (3.9), t_1 cannot be solved directly. Through polynomial transform, (3.9) becomes:

$$v_{f2}\,(t_1 - t_0) + R\cos(\theta_0 - \omega(t_1 - t_0)) - R = 0 \tag{3.13}$$

Let:

$$y = v_{f2}\,(t_1 - t_0) + R\cos(\theta_0 - \omega(t_1 - t_0)) - R \tag{3.14}$$

After solving t_0, an initial value has to be given for t_1 to begin iteration to approximate the true value of t_1 until y reaches the setup precision. The MATLAB algorithm developed to calculate the key time points is given in Figure 3.8. The original version of this algorithm [85] was modified to enable usage of variable feed rates. The MATLAB code is shown in the Appendix A.

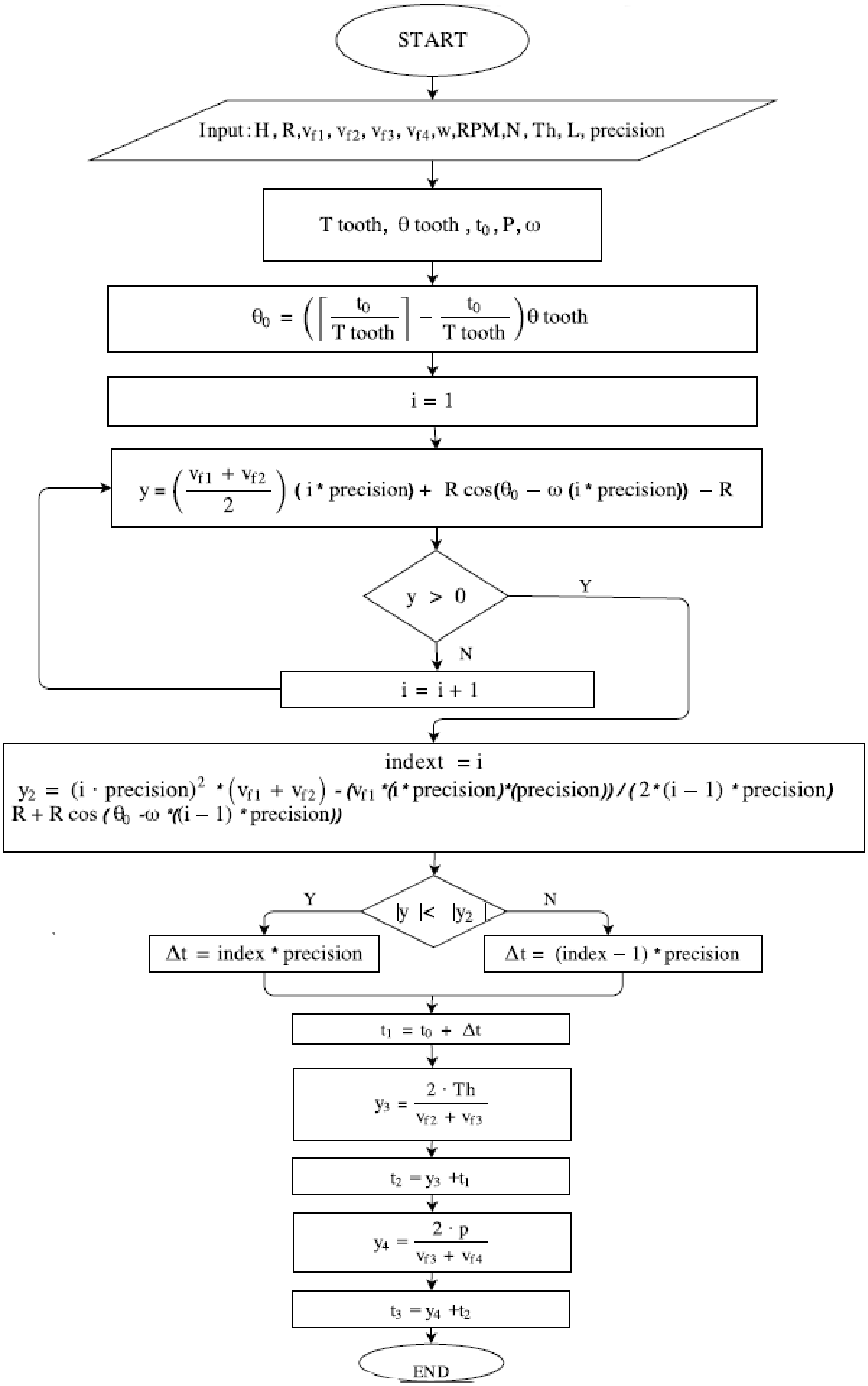

Figure 3.8 – Key time points' algorithm

To validate the mathematical model, key times obtained from MATLAB are compared with measurements from experiments ran by operating the machine with different spindle speed and feed rate as shown in Table 3.1. The results shown in Figure 3.9 represents a good match with analytical and experimental results which validate the key time points algorithm.

Table 3.1 Experiment and mathematical time

	Independent/input variables				**Time results (s)**					
Run	**Spindle speed (rpm)**	**Feed rates (in/min)**			**Analytical solution**			**experiment**		
		O.D.	*I.D.*	*Final*	*T1*	*T2*	*T3*	*T1*	*T2*	*T3*
1	255	2.1	1.4	2.8	0.76	13.17	21.94	0.56	12.79	21.56
2	285	2.35	1.6	3	0.45	11.45	19.46	0.52	12.11	19.45
3	315	2.1	1.8	3.2	0.46	11.59	18.9	0.62	11.71	18.76
4	255	2.6	1.4	3.2	0.95	11.8	19.82	0.42	11.57	19.78
5	315	2.6	1.8	2.8	0.45	10.33	18.34	0.46	10.39	17.77
6	255	2.1	1.8	2.8	0.76	11.89	19.9	0.59	11.77	19.38
7	315	2.1	1.4	3.2	0.46	12.87	20.88	0.59	13.03	21.26
8	255	2.6	1.8	3.2	0.95	10.83	18.19	0.46	10.42	17.47
9	315	2.6	1.4	2.8	0.45	11.31	20.09	0.42	11.57	20.27

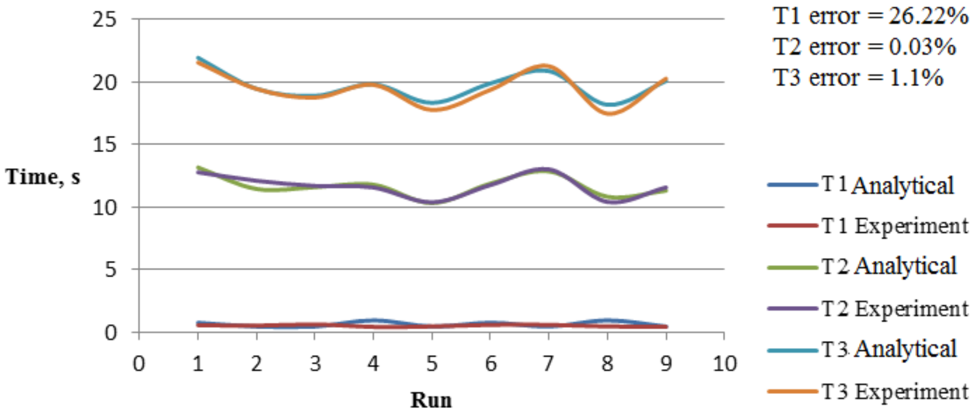

Figure 3.9 – comparison of calculated and measured time

3.5 Developed Mathematical model for effective teeth and chip load

The number of teeth involved in the slotting process at a transient time point is defined as the effective teeth which is a function of time. Effective teeth are closely related to the forces applied on the circular saw blade by the workpiece. The first requirement in the force analysis is, therefore, to develop a mathematical model so that the number of effective teeth at any given time point *t* can be determined.

Figure 3.10 shows the dynamic change of the effective teeth during the slotting process for the times before and after cut-through. The effective arc is the marginal line of the cutting face. It can be seen that the number of effective teeth is increasing in Figure 3.10 (a) and decreasing in Figure 3.10 (b). The immediate way to get the number of the effective teeth is to divide 2π by the radian corresponding to the effective arc. However, in the actual case, the condition involves more complexity since the number of effective teeth is not exactly proportional to the length of the effective arc. For example, there exists such a time point when one tooth is just leaving the effective arc and another tooth has not reached the effective arc.

Both the location of each tooth and the length of effective arc can be expressed by the radial angle in the global coordinate system and they are all functions of time. Thus the effective teeth can be identified as the teeth that are in the effective arc. To determine the number of effective teeth, the key point is to express the location of each tooth and the length of the effective arc as a function of time, respectively.

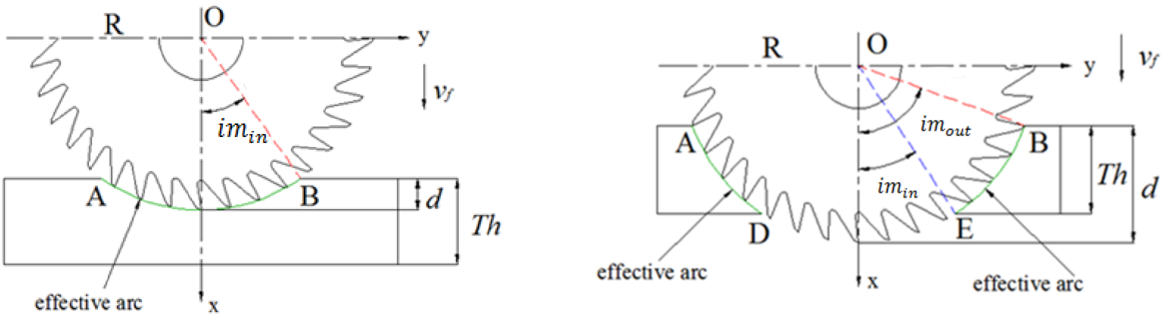

(a) $t_1 <= t <= t_2$ (b) $t_2 <= t <= t_3$

Figure 3.10 – Effective teeth before and after time t_2

The location of each tooth at a given time point can be denoted by θ_{phase} which is the global radial angle of each tooth in reference to the positive *x*-axis. Its value can be calculated as:

$$\begin{cases} \theta_{im}(n,t) = \dfrac{2\pi n}{N} + \omega t \\ where\ n\ is\ index\ of\ teeth, \quad n = 0,1,2,3,\dots,N-1 \\ where\ t\ is\ index\ of\ time, \quad t = 0,0.1,0.2,0.3,\dots,t_3 \end{cases} \tag{3.15}$$

The length of the effective arc as illustrated in Figure 3.10 can be expressed by im_{in} and im_{out} such that:

$$im_{in}(t) = arcos\frac{H - v_f(t)\,t}{R} \tag{3.16}$$

$$im_{out}(t) = arcos\frac{H + Th - v_f(t)\,t}{R} \tag{3.17}$$

The feed rate, v_f, is expressed as a function of time in (3.16) and (3.17). The feed rate $v_f(t)$ at time t, can be calculated as .

$$v_f(t) = \left(\frac{v_{f3} - v_{f2}}{t2 - t1} * t(t) - t1\right) + v_{f2} \quad when\ t1 < t < t2 \tag{3.18}$$

$$v_f(t) = \left(\frac{v_{f4} - v_{f3}}{t3 - t2} * t(t) - t2\right) + v_{f3} \quad when\ t2 < t < t3 \tag{3.19}$$

As discussed above, both the location of each tooth and the length of effective arc are expressed as a function of time. Direct comparisons between equations (3.15),(3.16), and (3.17) is not possible since they are is time cumulative whereas. Through (3.20), θ_{im} can be transformed to $\theta_{ju.}$, which can then be compared with (3.16) and (3.17).

$$\theta_{ju.}(n,t) = \frac{\theta_{im}(n,t)}{2\pi} - \left[\frac{\theta_{im}(n,t)}{2\pi}\right] \tag{3.20}$$

Let $N_e(t)$ and $X_i(t)$, respectively, represent the number of effective teeth and the status of tooth i at time t (whether it belongs to effective teeth or not). Therefore, the mathematical model for number of effective teeth calculation becomes:

$$\begin{cases} N_e(t) = \sum_{i}^{N} X_i(t) \\ where\ X_i(t) = 0\ or\ 1,\ \ 1\ represents\ yes\ and\ 0\ represents\ no \end{cases} \tag{3.21}$$

An algorithm in Figure 3.11 was developed to solve for the number of effective teeth according to this equation. The corresponding MATLAB script written to achieve the solution is given in Appendix A.

Because of time varying immersion angle, the uncut chip thickness in slotting process is similar to that in a milling process and varies periodically [12]. It is based on feed-per-tooth but changes due to the tool rotation. The instantaneous uncut chip thickness, dt_0 in milling can be calculated as:

$$dt_0 = v_f\ \theta_{ju.} \tag{3.22}$$

where, v_f is the feed rate (mm/rev-tooth) and $\theta_{ju}.$ is the instantaneous angle of immersion. It should be noted that (3.22) only applies to the situations where the axis of the spindle rotation coincides with the cutter geometrical axis [86]. Due to different moving mechanism and tool geometry, the instantaneous uncut chip thickness of each tooth at time t can be obtained by:

$$dt_0(n,t) = \frac{2\pi v_f(t) \sin(\theta_{ju.}(n,t))}{\omega\ .N} \tag{3.23}$$

Uncut chip thickness is an important factor as it is used to express all forces (tangential, radial and axial). Therefore, calculation of uncut chip thickness should be a prerequisite for force calculation. The mathematical algorithm used to calculate the chip thickness is also shown in Figure 3.11 together with the number of effective teeth.

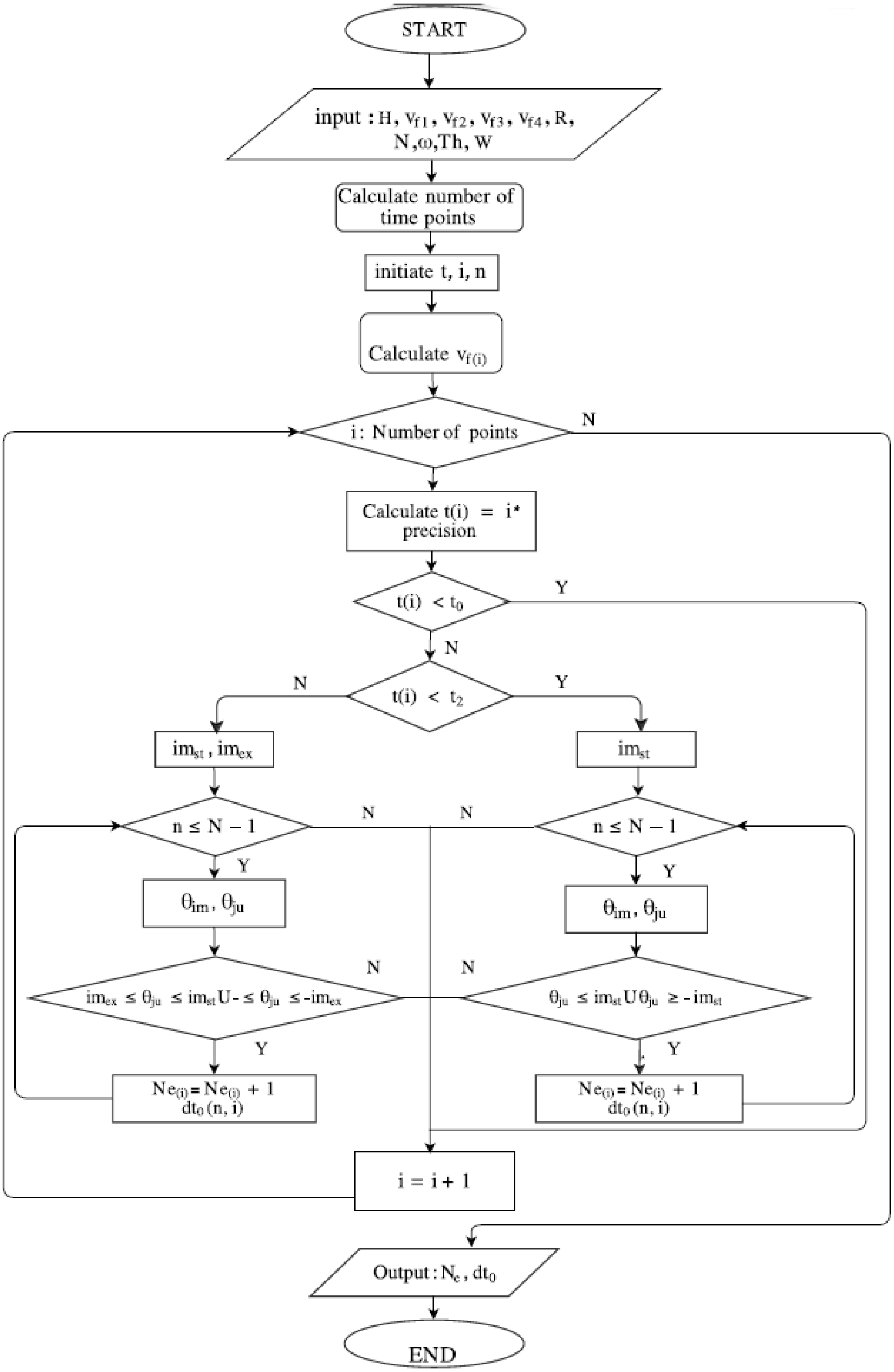

Figure 3.11 – Number of effective teeth and chip thickness algorithm

3.6 Analytical force calculation

There are various types of forces involved in an orthogonal cutting process as shown in the Figure 2.5. To obtain the overall force applied to the circular saw blade, the force acting on a single tooth is first considered by making use of the local coordinate system defined in Section 3.3. Referring to Figure 3.6, $x'o'y'$ is denoted as the local coordinate system and the resultant force (F_c) has two force components in directions of x' and y'. The force equilibrium that applies to a single tooth is shown in the Figure 3.12 where there is a balance between the resultant force (F_c) on the chip applied at the shear plane and the force ($\acute{F}c$) over the chip-tool contact zone applied to the rake face of the tool. The force acting in the x' direction is the tangential force (F_t) which is in the same direction as the cutting velocity, and the force acting in the y' direction is the feed force (F_f) which is in the same direction along the uncut chip thickness.

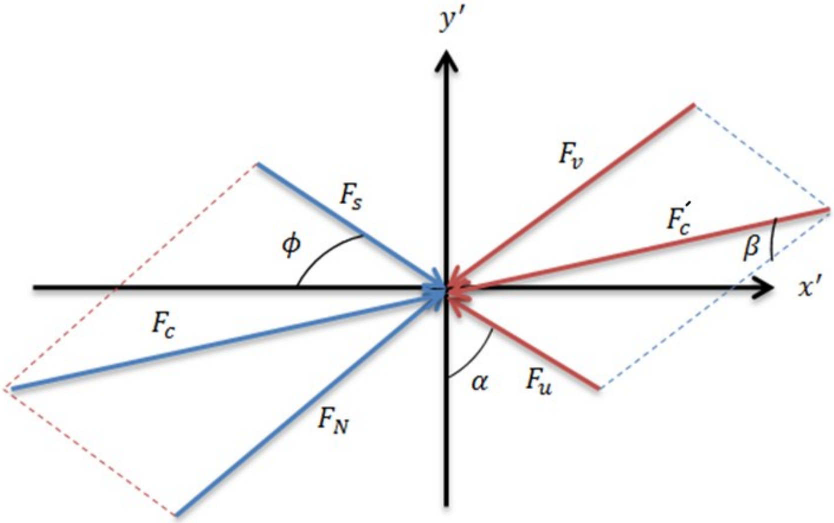

Figure 3.12 – Schematic of force equilibrium

As can be seen from Figure 2.3, the chip first sticks to the rake face of the tool called *sticking region* [12]. Then the chip starts sliding over the rake face. The sliding occurs with a constant *sliding friction* and, therefore, without contact between the rake face of the tool and the chip when the chip leaves the tool [12]. In the present work, the author assumed the model of primary shear deformation zone as a thin plate developed by Merchant [21] to gain simplification of the problem. The assumption entails considering the deformation as one that occurs in an infinitely thin shear plane.

The shear force (F_s) applied on the shear plane in the primary shear zone is obtained from [12]:

$$F_s = F_c \cos(\phi + \beta - \alpha) \qquad 3.24)$$

where, ϕ is the shear angle, β is the friction angle, and α is the rake angle of the tool. By having the assumption of uniform stress distribution on the shear plane, the shear force can also be expressed in terms of the shear stress (τ_s) and shear plane area (A_s) as [12]:

$$F_s = \tau_s \,.\, A_s \qquad (3.25)$$

In (3.25) τ_s assumed to be constant and the shear plane area can be expressed as:

$$A_s = \frac{dt_0 \,.\, W}{sin\phi} \qquad (3.26)$$

where, dt_0 is the uncut chip thickness calculated in the previous section, and W is the width of the slot (blade thickness).

By combining (3.23) with 3.24) to (3.26) the resultant force (F_c) can be calculated as:

$$F_c = \frac{\tau_s\, W\, 2\pi\, v_f(t) \sin(\theta_{ju.}(n,t))}{\omega\, N\, sin\phi\, \cos(\phi + \beta - \alpha)} \qquad (3.27)$$

Two components of the resultant force, tangential (F_t) in x' direction and feed (F_f) forces in y' direction, can be expressed [12] , respectively as:

$$F_t = F_c\, cos(\beta - \alpha) = \frac{\tau_s\, W\, 2\pi\, v_f(t) \sin\left(\theta_{ju.}(n,t)\right) cos(\beta - \alpha)}{\omega\, N\, sin\phi\, \cos(\phi + \beta - \alpha)} \qquad (3.28)$$

$$F_f = F_c\, sin(\beta - \alpha) = \frac{\tau_s\, W\, 2\pi\, v_f(t) \sin\left(\theta_{ju.}(n,t)\right)\, sin(\beta - \alpha)}{\omega\, N\, sin\phi\, \cos(\phi + \beta - \alpha)} \qquad (3.29)$$

The tangential and feed forces can also be given as:

$$F_t = K_t\, \frac{2\pi\, v_f(t) \sin\left(\theta_{ju.}(n,t)\right)}{\omega\, N} \qquad (3.30)$$

$$F_f = K_f\, \frac{2\pi\, v_f(t) \sin\left(\theta_{ju.}(n,t)\right)}{\omega\, N} \qquad (3.31)$$

where, K_t and K_f are *tangential* and *feed cutting force coefficients,* respectively and are equal to [12]:

$$K_t = \frac{\tau_s\, W\, cos(\beta - \alpha)}{sin\phi\ \cos(\phi + \beta - \alpha)} \tag{3.32}$$

$$K_f = \frac{\tau_s\, W\, sin(\beta - \alpha)}{sin\phi\ \cos(\phi + \beta - \alpha)} \tag{3.33}$$

Resultant force of the circular saw blade is the total force that is applied to the whole of the circular saw blade by the workpiece. It can be expressed by its *x*- and *y*-components, respectively. These two force components can be acquired by the summation of the relevant force components applied to the single effective tooth along the corresponding direction. Since the direction of the resultant force is changing with time in the global coordinate system, the *x* and *y* components of this resultant force also change with time. The resultant force applied to the circular saw blade in *x* and *y* directions can be calculated as:

$$F_x = \sum_{n=1}^{N} (-F_t \cos(\theta) - F_f \sin(\theta)) \tag{3.34}$$

$$F_y = \sum_{n=1}^{N} (+F_t \sin(\theta) - F_r \cos(\theta)) \tag{3.35}$$

Since the slotting machine has eighty spindles, the overall force applied to the machine during the cutting of one slot can be calculated as the sum of the resultant forces applied to all blades. However, there is a phase difference between spindles in reality. Therefore, the summation of forces has to take the phase difference in rotation of all the blades into account of. For this study the phase difference is implemented in MATLAB by adding random numbers (between 0 to 5 degree) to $\theta_{ju.}$. It should be noted that the new $\theta_{ju.}$ ($\theta_{ju.1}$) is used only in force calculation of the whole machine.

Power, torque and material removal rate

The instantaneous cutting torque on the spindle depends on both the cutter radius and instantaneous tangential force. The time varying torque (T) on only one spindle during cutting a single slot can be calculated as [12]:

$$T = \frac{D}{2} \sum_{n=1}^{N} F_t(\theta_{ju.}) \tag{3.36}$$

$$when,\ \theta_{ju.} \leq im_{st} \cup \theta_{ju.} \geq -im_{st}\ \ or\ im_{ex} \leq \theta_{ju.} \leq im_{st} \cup -im_{st} \leq \theta_{ju.} \leq -im_{ex}$$

Material removal rate (MRR) is another important factor in machining. An increase in its value, while reducing machining time and cost, is desirable [87]. MRR for a volume of material removed per unit time can be obtained as:

$$MRR = W\ .\ \ v_f(t)\ .\ dt_0\ .\ N\ .\ RPM \tag{3.37}$$

It is possible to obtain the friction power (P_u) on the tool chip contact face as [12]:

$$P_u = F_u\ .\ V_c \tag{3.38}$$

where, V_c is the deformed chip velocity that slides on the rake face of the tool which can be calculated as:

$$V_c = \frac{sin\phi}{cos(\phi - \alpha)} V \tag{3.39}$$

where, V is the cutting velocity which for the case of a circular saw blade is obtained by [12]:

$$V = \frac{2\pi\ .\ R\ .\ RPM}{60} \tag{3.40}$$

There is also another type of power on the shear plane named shear power (P_s) [12].

$$P_s = F_s\ .\ V_s \tag{3.41}$$

where, V_s is the shear velocity by which material shears away from the workpiece and it can be calculated as [12]:

$$V_s = \frac{cos\alpha}{cos(\phi - \alpha)} V \tag{3.42}$$

Now, by having friction and shear powers, it is possible to know the total power spent on the cutting process such that:

$$P_{tc} = P_s + P_u \tag{3.43}$$

Since there is a balance of forces and velocities in the cutting process, the total power that the spindle motor generates is also equal to the summation of shear and friction power.

$$P_{tc} = F_t \, . V \tag{3.44}$$

To obtain a mathematical solution for the forces as per the above series of discussion, input data that correspond to the specific properties and geometries of the workpiece and tool were used along with the machine parameters that are used by RGL. Friction angle, shear angle, and shear stress values are typically obtained from empirical investigations. The literature and small-scale numerical simulations were thus used to determine the values of these three parameters. The measured shear angles from finite element simulations were compared with the Atkins shear angle model [88]. Atkins showed that shear angle for the least tangential force satisfies the following relation:

$$\begin{aligned} &\left[1 - \frac{sin\beta \, sin\phi}{cos(\beta - \alpha)\, cos(\phi - \alpha)}\right] \left[\frac{1}{cos^2(\phi - \alpha)} - \frac{1}{sin^2\phi}\right] \\ &\qquad = -[cot\phi + tan(\phi - \alpha) \\ &\qquad + Z] \left[\frac{sin\beta}{cos(\beta - \alpha)} \left\{\frac{cos\phi}{cos(\phi - \alpha)} + \frac{sin\phi \, sin(\phi - \alpha)}{cos^2(\phi - \alpha)}\right\}\right] \end{aligned} \tag{3.45}$$

where, $Z = \frac{Q}{\tau\, dt_0}$. Q is the fracture toughness of the workpiece making the shear angle to be dependent on the material type. MATLAB was used to solve the non-linear shear angle equation.

The shear angle and shear stress obtained from the numerical simulations were used as inputs to the analytical model for calculation of the forces. The algorithm that was used to solve forces, torque, MRR, and powers is shown in Figure 3.13. The corresponding MATLAB script used to get the solutions and plots is given in Appendix A.

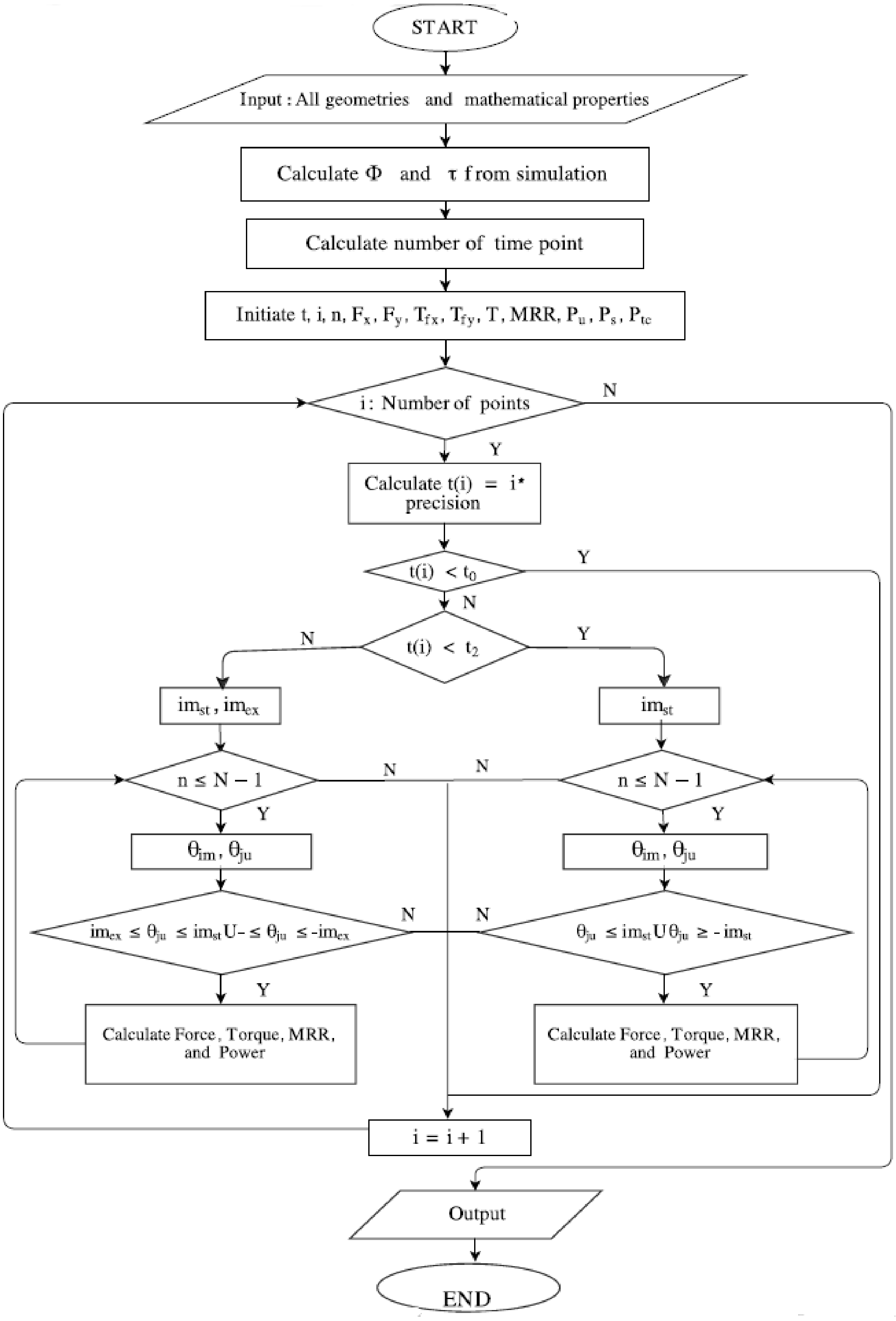

Figure 3.13 – Force calculation algorithm

3.7 Finite element simulation

Finite element is a powerful method that has been applied in different simulations of metal cutting processes. Both ABAQUS (Dassault Systemes) and AdvantEdge (Third Wave Systems) are used for the metal cutting simulations conducted for this study. The simulations were developed under three-dimensional and two-dimensional models in ABAQUS and AdvantEdge, respectively.

The element type used in ABAQUS was eight-node linear brick with reduced integration and hourglass control. The dynamic explicit method was applied using ABAQUS to avoid long run times, since implicit method has high number of iterations which poses difficulty in attaining convergence. Lagrangian approach was used in ABAQUS/Explicit to idealize the chip formation as the mesh nodes are moving with the material movement. The Lagrangian model included the element deletion as the failure criteria to remove chip from the workpiece.

AdvantEdge is a software package developed solely for the purpose of performing cutting simulation. It is also simpler to implement since an in-depth knowledge of finite element methods is not a requirement. In all simulations the tool wear and the effects of coolant were neglected to reduce the simulation time.

Simulation of cutting processes is complex due to large plastic deformation and material removal at large strain rates and high temperatures [38]. Johnson-Cook material model is one of the commonly used orthogonal cutting models, since it depends on strain rate and temperature. The Johnson-Cook martial model which is used in this study can be represented as:

$$\sigma = (A + B\varepsilon^n)\left(1 + C\, ln\left(\frac{\dot{\varepsilon}}{\dot{\varepsilon}_0}\right)\right)\left(1 - \left(\frac{T - T_r}{T_m - T_r}\right)^m\right) \tag{3.46}$$

where, σ is the equivalent stress, A is the initial plastic flow stress at zero plastic strain, B is the strain hardening coefficient, n is the strain-hardening index, C is the strain rate index, ε is the plastic strain, $\dot{\varepsilon}$ is the plastic strain rate, $\dot{\varepsilon}_0$ is the reference plastic strain rate, T is the current temperature, T_r is the reference temperature, T_m is the melting temperature, and m is the thermal softening index. These values are usually obtained from Split Hopkinson Pressure Bar (SHPB) impact testing data [89].

Material properties

Two different materials were chosen for the workpieces which correspond to the L-80 alloy steel, and K-55 alloy steel pipes as they are the most common slotted liner materials handled by RGL. The L-80 and K-55 alloy steels have similar chemical compositions and properties to AISI 4140 alloy steel and AISI 4340 alloy steel, respectively. The Johnson-Cook plasticity model parameters and general thermal and mechanical properties of the workpieces obtained from literature are shown in Table 3.2 [90][58].

Table 3.2 Material properties of the workpieces

Properties	AISI 4140	AISI 4340	Units
Density	7850	7830	kgm^{-3}
Young's modulus	219	200	Gpa
Poisson's ratio	0.29	0.29	-
Thermal expansion	13.7	12.3	$\mu m\, m^{-1}\, K^{-1}$
Melting temperature	1820	1793	K
Bulk temperature	300	-	K
Thermal conductivity	42	38	$W\, m^{-1}\, K^{-1}$
Specific heat capacity	-	477	$J\, kg^{-1}\, K^{-1}$
A	595	792	Mpa
B	580	510	Mpa
C	0.023	0.014	-
n	0.133	0.26	-
m	1.03	1.02	-

Since the elastic moduli of cutting tools are usually higher than those of the workpieces, rigid elastic cutting tool was assumed with the mechanical properties shown in Table 3.3.

Table 3.3 HSS M2 cutting tool properties

Density (kgm^{-3})	**Young's modulus** (Gpa)	**Poisson ratio**
8160	214	0.3

Boundary conditions

Figure 3.14 shows the typical finite element model used for cutting processes' simulation. The rake angle, relief angle, and tool edge radius are different for each case of simulation and will be defined in the next chapter. The length and height of the workpiece were chosen as 5 and 3 mm, prospectively. The width of the workpiece in the three-dimensional model was selected as 0.4 mm. The different depths of cut used were obtained from the mathematical models presented in Section 3.5. The workpiece is fully fixed and the tool moves with the cutting speed from right to left to create the chip. The reference point was defined at cutting tool edge to measure the cutting forces.

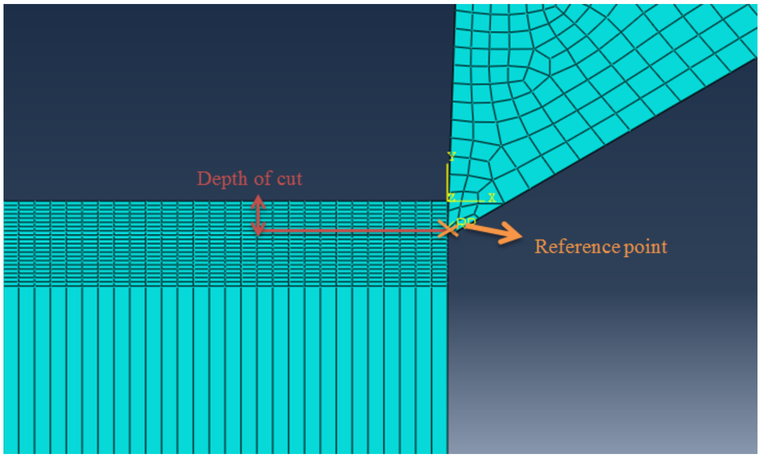

Figure 3.14 – Typical simulation model

Chip separation criteria

Johnson-Cook damage law was used for chip separation in this study as given by [58]:

$$D = \sum \left(\frac{\Delta\varepsilon}{\varepsilon_f} \right) \tag{3.47}$$

where, D is the damage parameter, $\Delta\varepsilon$ is the increment of the equivalent elastic strain which is updated at every load step, and ε_f is the equivalent strain at failure and can be expressed as [58]:

$$\varepsilon_f = \left[D_1 + D_2 \exp D_3 \left(\frac{P}{\sigma} \right) \right] \left[1 + D_4 \ln \left(\frac{\dot{\varepsilon}}{\dot{\varepsilon}_0} \right) \right] \left[1 + D_5 \left(\frac{T - T_r}{T_m - T_r} \right) \right] \tag{3.48}$$

where, $\frac{P}{\sigma}$ is the ratio of hydrostatic pressure to equivalent stress. When D (damage parameter) of an element reaches 0.1, the failure occurs and the FEM algorithm deletes the element. The damage parameters for AISI 4140 and AISI 4340 are presented in Table 3.4 [58][90].

Table 3.4 Damage parameters for the workpieces

	D_1	D_2	D_3	D_4	D_5
AISI 4140	1.5	3.44	-2.12	0.002	0.1
AISI 4340	0.05	3.44	-2.12	0.002	0.61

Contact and friction modeling

Kinematic contact algorithm is used in ABAQUS/Explicit and defined by the forces between two surfaces called master and slave surface. As shown in the Figure 3.15 the nodes of the slave surface that penetrate the master surface are determined at each time increment and the resistance force will be applied to them [91].

Sticking and sliding are two zones that contact interactions occur in. Both normal and shear forces are transmitted for the cases where friction contact interaction between bodies exist [13]. When there is no contact between the chip and tool, the normal and shear stresses are tend to zero. A constant friction coefficient, μ, is assumed in the sliding region. In the analytical model, the coefficient of friction was also considered constant based on the assumption that the chip slides with a constant friction coefficient on the tool. This friction coefficient is related to the friction angle such that [12]:

$$\mu = tan\beta = \frac{F_u}{F_v} \tag{3.49}$$

Stresses are maximum at the tool edge which is due to sticking friction. Sticking region was modeled by using Coulomb friction law which is defined by:

$$\begin{cases} \tau_f = \mu\, \sigma_n \quad when \;\; \mu\, \sigma_n < \tau_{max} \\ \tau_f = \tau_{max} \quad when \;\; \mu\, \sigma_n > \tau_{max} \end{cases} \tag{3.50}$$

where, τ_f is the frictional stress, σ_n is the normal stress along the tool-chip interface, τ_{max} is the maximum value of the frictional stress which is assumed to be equal to yield shear stress of the material (τ). The friction coefficient used in ABAQUS simulations was 0.15. The friction model was selected as default of the software in AdvantEdge by having the coefficient of friction of 0.5.

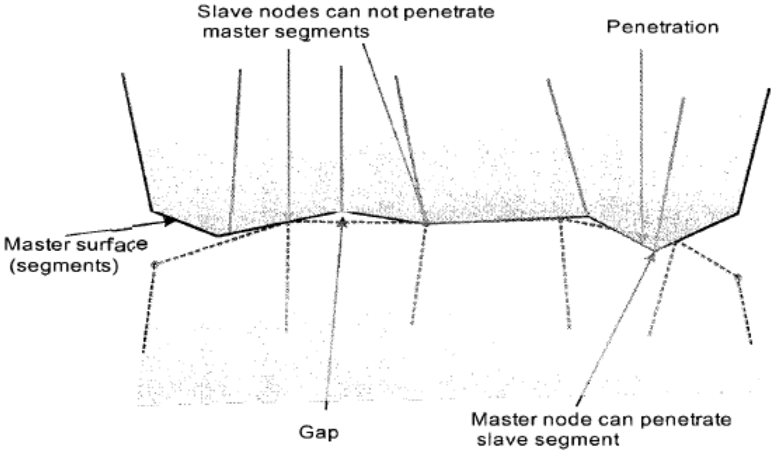

Figure 3.15 – Kinematic contact algorithm between master and slave surfaces [91]

3.8 Dynamic analysis of slotting process

The conditions of audible noises and tool breakage at RGL's facility indicated the existence of significant vibration during cutting. This observation motivated the study of vibration by determining the stability lobe diagram. By having the stability lobe diagram, it is possible to know the range of minimum depth of cut and spindle speed for a stable machining process. The depth of cut is also a crucial parameter that depends on the feed rate. Ranges of optimal values for feed rate and spindle speeds can therefore be obtained by avoiding chatter vibration in the process.

Regenerative chatter is one of the most common but undesirable phenomena in cutting processes. In real applications where the assumption of having a rigid tool does not hold, the cutting forces from chip cause tool deflection resulting in vibration. The vibration results in wavy surfaces on the workpiece. As shown in Figure 3.16, material left by a tooth on the surface of the workpiece, has to be removed by the one immediately following it. Therefore, the instantaneous chip thickness varies due to vibration and the time between one tooth to the next [87]. The differences in instantaneous chip thickness cause chatter vibration, poor quality of surface, tool wear and instable cutting.

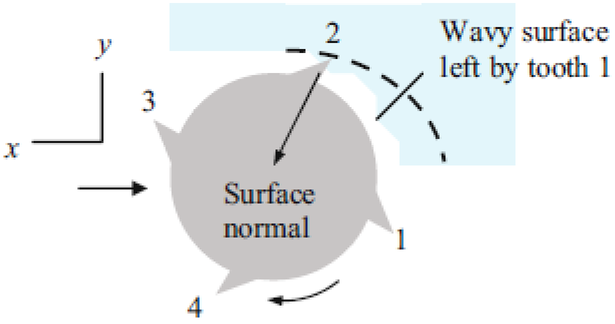

Figure 3.16 – Regenerative chatter in milling [87]

Figure 3.17 shows the instantaneous chip thickness in the presence of vibration. This chip thickness can be calculated as $f_t sin\phi + n(t-\tau) - n(t)$. In this equation, $f_t sin\phi$ represents the value of the mean chi thickness, τ is the tooth passing frequency which leads $n(t-\tau)$ to be vibration along the surface normal causes by the previous tooth [87].

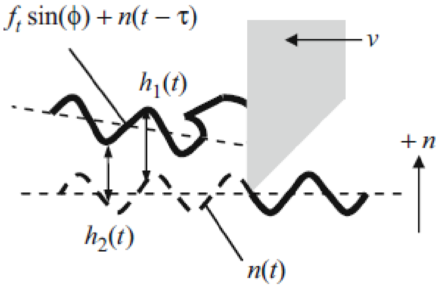

Figure 3.17 – Instantaneous chip thickness in milling [87]

Stability lobe diagram

Cutting force direction in milling process is time dependent which makes the analytical solution difficult. Tlusty [81] overcomes this difficulty by assuming average force direction during milling process. Therefore, this assumption causes the system to be time invariant. Tlusty then projected the assumed average force to the *x* and *y* directions using directional orientation factors. Then the projected results can project onto the surface normal (Figure 3.16). The force studied in this section for stability lobe is the maximum force applied to the circular saw blade. In this case the stability is investigated at the most vulnerable time of the slotting operation. The reason for selecting the maximum force is based on the logic that the blade will be stable for the whole process if it is stable at the highest applied force. In addition, the number of teeth that are in touch with the workpiece and the immersion angle at the time step the force taken should be determined. It is worth to mention that the teeth of the circular saw blade are spaced equally in the whole of this study.

The process of generating stability lobe diagram is [87]:

- Defining the oriented Frequency Response Function (FRF). The oriented FRF can be determined by summation the products of orientation factors and force in *x* and *y* directions. Orientation factor can be obtained by knowing the angle between force and corresponding *x* or *y* directions, and then after projecting in the desire direction, it should be projected onto the surface normal.
- Solving the following equation

$$\varepsilon = 2\pi - 2tan^{-1}\left(\frac{RE[FRF_{orient}]}{IM[FRF_{orient}]}\right) \tag{3.51}$$

The above equation determines the difference between tooth vibrations over the frequency range.

- Finding depth of cut limit (b_{lim}) for the frequency range from:

$$b_{lim} = \frac{-1}{2K_s RE[FRF_{orient}]N_e} \tag{3.52}$$

where, K_s is the applied force coefficient.

- Solving the spindle speeds in a frequency range.

$$\frac{f_c}{\Omega N} = K + \frac{\varepsilon}{2\pi} \tag{3.53}$$

where, f_c expressed in *Hz*, Ω expressed in *revolution/second*, and K is the integer value (*K=0, 1, 2, ...*). In (3.53), ΩN represents tooth passing frequency, and $\frac{f_c}{\Omega N}$ represents the ratio of the chatter frequency to the forcing frequency. b_{lim} vs Ω should be plotted for several K.

In (3.52), instead of using $K_s.N_e$ in the denominator which is the average cutting force coefficient times the number of teeth in the cutting, the summation of cutting force coefficients when highest force due to the maximum number of teeth in the process is used. Therefore, by selecting the values for spindle speed and feed rate in the stable region results a free chatter operation, since the stability lobe shows the stable region for the maximum applied force.

The oriented FRF in (3.52) can be calculated as:

$$FRF_{orient} = \mu_x FRF_x + \mu_y FRF_y \tag{3.54}$$

where, μ_x and μ_y are directional orientation factors. If the direction of the surface normal (n) be towards the center of the circular blade, $F_n = F_y \cos(0) = Fcos(\beta - \alpha)\cos(0) = Fcos(\beta - \alpha)$, so the directional orientation factor μ_y becomes $\mu_y = \cos(\beta - \alpha)$. To find the other directional orientation factor, F_x needs to be projected onto the surface normal, so $F_n = F_x \cos(90) = Fsin(\beta - \alpha)\cos(90) = 0$, and μ_x becomes zero.

3.9 Remarking points

By the methodology presented in chapter 3, it is possible to obtain the values of applied force to the blade in both x and y directions from the combination of analytical and numerical models during cutting process. The resulting maximum applied force with the greatest number of blade teeth that are in contact with the workpiece during cutting operation are used to draw the stability lobe diagram. The stable region for chatter free metal cutting is obtained from the stability lobe diagram by the combination of desirable values of spindle speed and depth of cut.

The resulting applied force and maximum numbers of teeth that are in touch with the workpiece are also used in chapter 5 to conduct static analysis of the blade. The results from static analyse is used for comparison with the new design of the blade from the shape optimization.

4. RESULTS AND DISCUSSION

The methods presented in the previous chapter are applied for different cases of blade geometry, machine parameters, and workpiece material for force calculation. Since the results obtained for RGL custom made machine are specific, the comparison with literature was difficult to achieve. However, great effort is put into validating the general trends to previous works.

4.1 Different rake and relief angles

In this case, the HSS M2 circular saw blade is chosen with the numerical parameters' and applicable models specified in 3.7. The cutting parameters for all cases presented in this section are kept the same. Two different workpieces materials for L-80 and K-55 pipes are selected. All process parameters and geometries are shown in Table 4.1. The obtained shear angles and shear stresses from simulations conducted in ABAQUS/Explicit are applied on the mathematical model for comparison. For simplification, the shear angle is assumed to be constant in mathematical model for each case.

Table 4.1 Input parameters for different blade angles

Blade diameter (in)	3.227	**Depth of cut (in)**	0.03
Blade rake angle (degree)	2, 10, 20	**Pipe thickness (in)**	0.362
Blade relief angle (degree)	5, 15, 30	**Pipe diameter (in)**	7
Teeth edge radius (mm)	0.01, 0.02, 0.03, 0.04, 0.05	**O.D. slot length (in)**	1.842
Blade teeth number	56	**Friction coefficient**	0.15
Blade thickness (in)	0.023	**RPM**	255
Cutting speed (in/sec)	43	**Feed rate (in/min)**	1

The tooth form for all cases in this thesis is triangular Ratchet form which has only one primary relief angle. Another tooth form is curvilinear Parrot tooth form which has primary and secondary relief angles. The blade with curvilinear tooth form has more strength. However, more heat generates during cutting process because this blade has more material and makes more contact and friction during slotting [92]. The depth of cut which is selected for these cases is from mathematical calculation for uncut chip thickness. It is known that during the cutting process the uncut chip thickness varies and which changes the shear angle. However, a constant shear angle is assumed here and the obtained forces for the same uncut chip thickness from both analytical and simulations are compared. The forces in the mathematical model are time variant. Therefore, selection of forces is based on their uncut chip thickness. It means that the forces are chosen to be able to compare with forces which have the same uncut chip thickness with the FEM model. In addition shear angles are compared with the shear angle for the least cutting force presented in equation (3.45). The fracture toughness in (3.45) was only found for L-80 as $65\ ksi\sqrt{in}$.

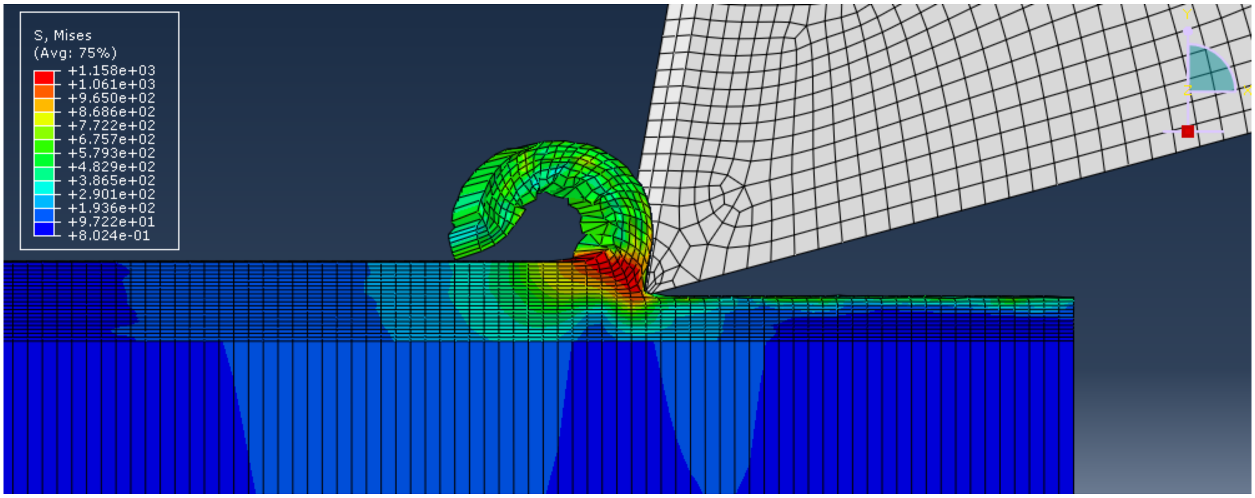

Figure 4.1 – L-80 pipe with 2 rake and 15 relief angles

Figure 4.1 shows one of the simulation results related to pipe L-80, rake angle of 10 and relief angle of 15. In addition to shear angle, shear stress also needs to be calculated. as:

$$\tau_Y = \frac{\sigma_Y}{\sqrt{3}} \tag{4.1}$$

where, τ_Y is the yield shear stress of the material and σ_Y is the yield stress under tension stress which is the Von-Mises stress available from the results in ABAQUS.

The results for the shear angles and cutting forces for 0.01 round edges are presented in Table 4.2 and Table 4.3. The shear angle was measured as an angle between the cutting direction originating from the tooth tip and shear plane.

Table 4.2 Results of shear stresses (mpa)

	L-80	***K-55***
2 rake – 30 relief – 0.01 round	653	496
10 rake – 15 relief – 0.01 round	668	493.6
20 rake – 5 relief – 0.01 round	666	486.7

Table 4.3 Results for sharp tools

<table>
<tr><th rowspan="2"><i>L-80</i></th><th colspan="2"><i>Φ</i></th><th colspan="2"><i>Fx (N)</i></th><th colspan="2"><i>Fy (N)</i></th></tr>
<tr><th><i>FEM</i></th><th><i>Analytical</i></th><th><i>FEM</i></th><th><i>Analytical</i></th><th><i>FEM</i></th><th><i>Analytical</i></th></tr>
<tr><td>2 rake – 30 relief – 0.01 round</td><td>31</td><td>31.4</td><td>72</td><td>68.6</td><td>9</td><td>7.8</td></tr>
<tr><td>10 rake – 15 relief – 0.01 round</td><td>34.5</td><td>33.9</td><td>70</td><td>66.1</td><td>10</td><td>1.7</td></tr>
<tr><td>20 rake – 5 relief – 0.01 round</td><td>37</td><td>36.4</td><td>60</td><td>54.7</td><td>10</td><td>11.1</td></tr>
<tr><th rowspan="2">K-55</th><th><i>Φ</i></th><th colspan="2"><i>Fx (N)</i></th><th colspan="3"><i>Fy (N)</i></th></tr>
<tr><th><i>FEM</i></th><th><i>FEM</i></th><th><i>Analytical</i></th><th><i>FEM</i></th><th colspan="2"><i>Analytical</i></th></tr>
<tr><td>2 rake – 30 relief – 0.01 round</td><td>34.07</td><td>54</td><td>52.7</td><td>7</td><td colspan="2">6.01</td></tr>
<tr><td>10 rake – 15 relief – 0.01 round</td><td>37.5</td><td>51</td><td>45.6</td><td>7</td><td colspan="2">1.2</td></tr>
<tr><td>20 rake – 5 relief – 0.01 round</td><td>39.1</td><td>39</td><td>38.8</td><td>3</td><td colspan="2">7.9</td></tr>
</table>

From Table 4.3, it is seen that the predicted shear angles for L-80 pipe was in close agreement with those from simulations. As the rake angle increases, the shear angle increases which is also showed by Fermaniuk [92] who studied the slotting process on the same machine. Shi et al. [42] also presented that the shear angle increased at higher rake angles at the fix friction coefficient. The tangential cutting forces from both models were close which can validate the analytical model.

The feed forces, however, shows some disagreement especially for the tooth having 10 degree rake angle. This can be due to the differences in feed rate between the analytical model and simulations. While a constant downward feed rate of *1 in/min* was assumed in the analytical model, there was no feed rate in the FEM simulations.

In all cases, as the rake angle increases, the tangential cutting forces decrease which is also shown in [93]. Although it has been expected that the feed forces also decrease at higher rake angles, such trend is not seen for L-80 pipe as it is shown at a fixed friction coefficient by Shi et al. [42]. The feed forces are in the same range for different rake angle which again might increase because of undefined feed rate. Higher rake angle is preferred due to the low cutting forces. Lowering the cutting forces also improve the surface quality and decrease the effects of chatter. The only disadvantage of higher rake angle could be insufficient chip breakage which can possibily impair the process [93]. Tooth height should also be considered for rake angle determination. In choosing tooth rake angle, relief angle should be considered in order to avoid possible long time rubbing between the tool and workpiece, and material loss compensation of the blade.

Although the shear angle for cutting L-80 pipe is greater than the ones for K-55 pipe, the opposite is true for their shear stress. Therefore, the force needed to make a slot is higher for the L-80 pipe. This is because of the differences in their material strength which makes the K-55 pipe easier to cut.

All six cases are also simulated using different tooth edge radius to see effects on the shear angle and cutting force. The resultant shear angles are shown in Table 4.4. The effects of tool edge radius on cutting forces are shown in Figure 4.3 and Figure 4.4.

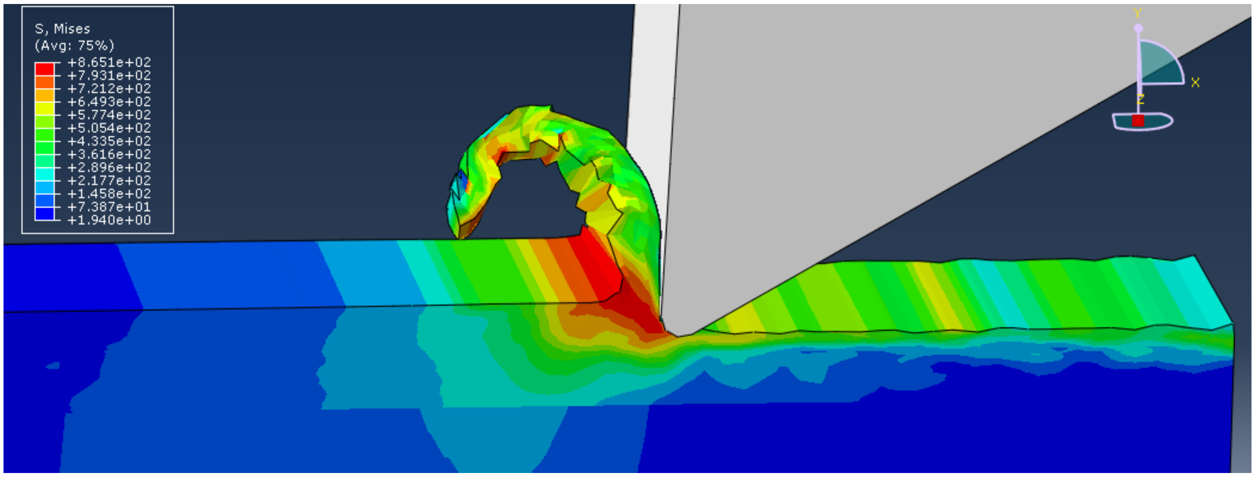

Figure 4.2 – K-55 pipe with 0.05 round tooth edge

Table 4.4 Results of shear angle depending on tooth edge radius

type	***Edge radius***	***L-80 shear angle***	***K-55 shear angle***
2 rake – 30 relief – 0.01 round	0.01	31	34.07
	0.02	25.9	30.8
	0.03	23.7	28.5
	0.04	20.5	25.07
	0.05	17.4	22.4
10 rake – 15 relief – 0.01 round	0.01	34.5	37.5
	0.02	32.4	34.7
	0.03	31	32.4
	0.04	30.1	28.6
	0.05	24.5	22.9
20 rake – 5 relief – 0.01 round	0.01	37	39.1
	0.02	32.4	35.05
	0.03	31	32.3
	0.04	30.1	28.8
	0.05	24.5	25.1

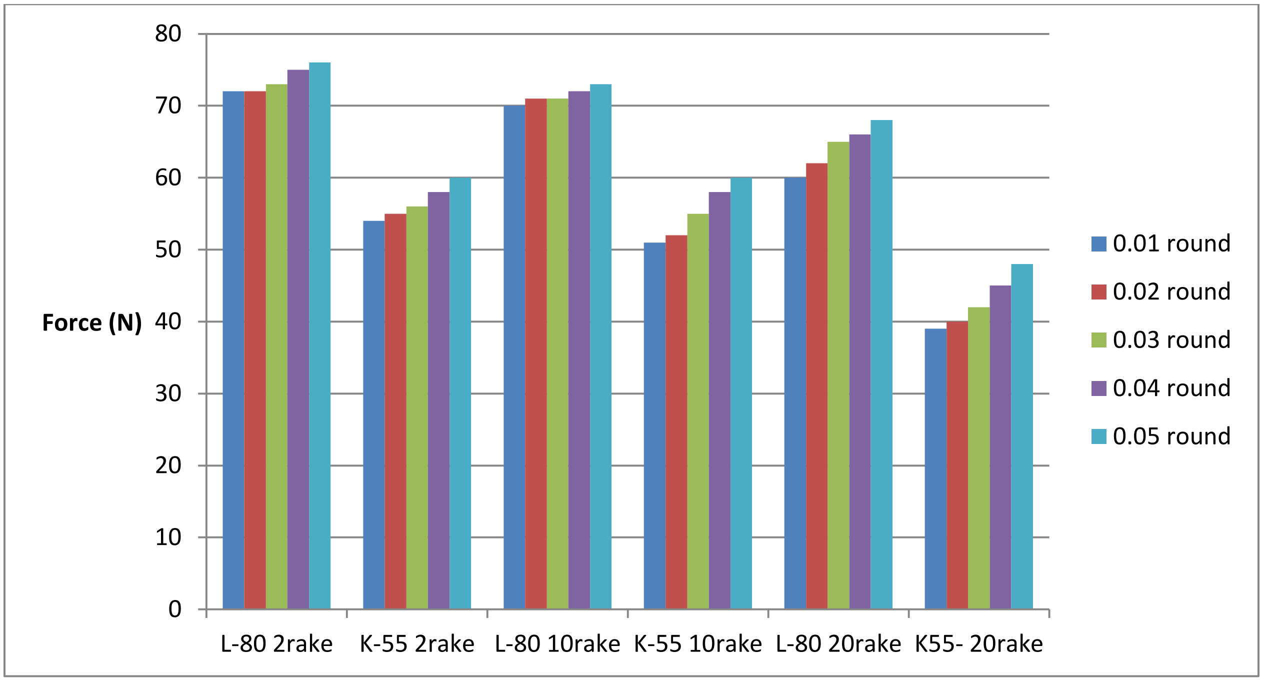

Figure 4.3 – Tangential cutting force depending on tool edge radius

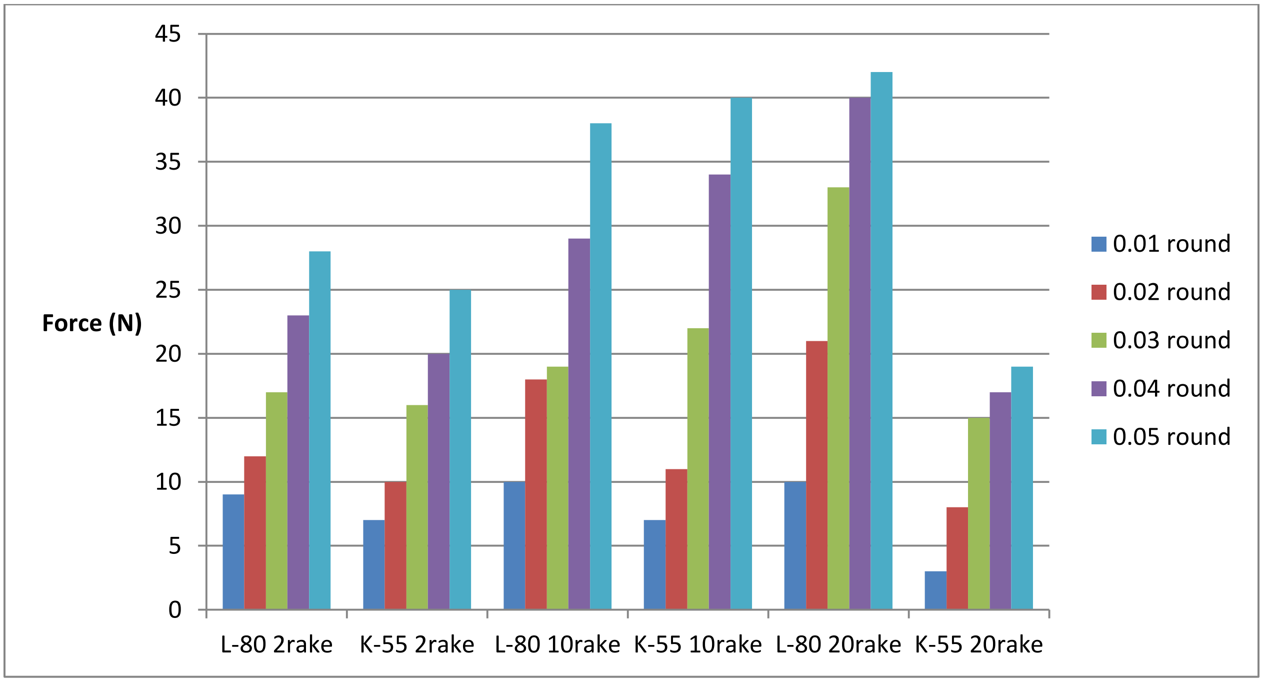

Figure 4.4 – Feed cutting force depending on tool edge radius

Observing Table 4.4, Figure 4.3 and Figure 4.4, it is seen that by increasing the tooth edge radius, both force components are increased because larger forces are needed for material shearing due to the increase in bluntness of the cutting edge. However, shear angle reduced as a result of having larger radius for the rounded edge. These results agree with Altan et al. [46]. Generally, tool edge radius does not have a significant influence on cutting forces. It mostly affects depth of cut and feed rate and consequently the cutting forces. The radius of tip edge is also important for the surface quality. Surface roughness has a direct impact on the chatter in cutting processes. It is accepted that tool edge radius should be less than the feed per tooth [93].

For a blade that has 56 teeth, RPM is 255 *rev/min*, and the feed rate is 1 *in/min*, the feed per tooth would be 0.043 *mm/tooth* ($feed/(no.of\ teeth * RPM)$). It means that the edge radius greater than 0.04 *mm* would have substantial effects on the cutting force and surface roughness.

Another important aspect, especially in micro-machining, is minimum chip thickness. It is considered that the chip does not form unless it gets larger than the minimum chip thickness. If the chip thickness is less than the minimum chip thickness, it implies that the depth of cut is not enough to remove material from the workpiece. In this case, the material experiences elastic deformation due to the compression under the tool and sticks to the workpiece after the tool passes. If the chip thickness is equal to the minimum chip thickness, the material starts to separate from the workpiece as a result of both elastic deformation and shearing force. However, only some part of the material will form the chip and the rest will recover back after the tool has left the position. When the chip thickness is greater than the minimum chip thickness, material removes from the workpiece and forms the chip. Therefore, the ratio of minimum chip thickness to the cutting edge radius is one of the significant factors in cutting processes. The tool edge radius, the depth of cut, and feed per tooth should thus be chosen accordingly. Aramcharoen et al. [94] shows that cutting forces increase as the ratio of unreformed chip thickness to cutting edge radius increases.

4.2 Effect of cutting speed

To investigate the effect of RPM on the cutting force, several FE simulations are run using ABAQUS/Explicit. The same HSS M2 tool blade and L-80 pipe with the same mechanical and material properties are used. It is important to know that all parameters are kept the constant except the cutting speed which is different for each run as shown in Table 4.6.

Table 4.5 Input parameters for different cutting speeds

Blade diameter (in)	3.07	**Depth of cut (in)**	0.004
Blade rake angle (degree)	2	**Pipe thickness (in)**	0.362
Blade relief angle (degree)	30	**Pipe diameter (in)**	7
Teeth edge radius (mm)	0.01	**O.D. slot length (in)**	1.842
Blade teeth number	56	**Friction coefficient**	0.15
Blade thickness (in)	0.023	**RPM**	255, 285, 315, 355, 385
Cutting speed (in/sec)	41, 45.8, 50.6, 57, 61.8	**Feed rate (in/min)**	2

For this analysis, 2D ABAQUS/Explicit with Arbitrary Lagrangian-Eulerian (ALE) approach is applied. ALE approach is a combined method of both Lagrangian and Eulerian approaches which avoids mesh distortion that usually occurs in Eulerian approach while modeling the chip using Lagrangian approach [72]. Figure 4.5 shows the difference in formed chip when using Lagrangian and ALE approaches for cutting at 255 rpm.

In addition to the conventional model used for such cases, simulations that use the model of the whole blade are performed in ABAQUS as shown in Figure 4.6. Analytical models have been used to calculate the forces for similar conditions as the simulations by keeping the shear angle constant. The main purpose here is to compare the resulting forces from different cutting speeds.

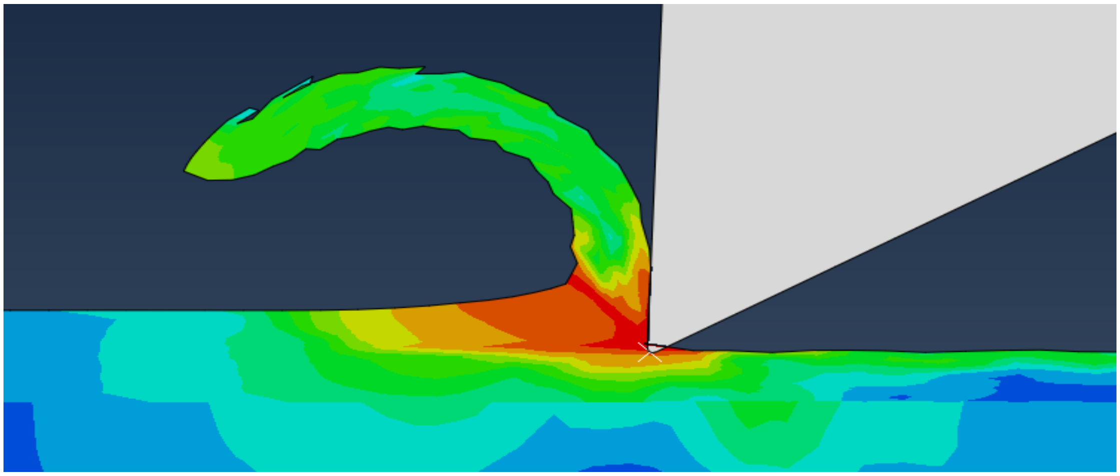

(a) Lagrangian approach

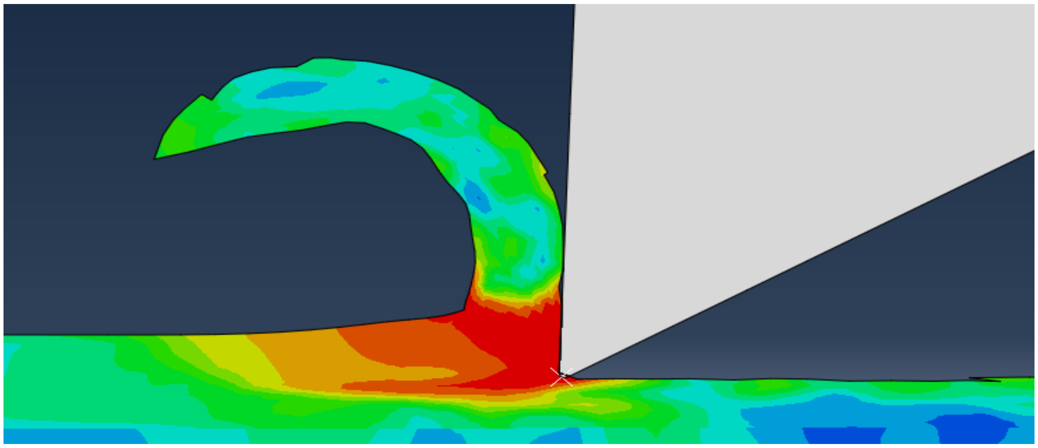

(b) ALE approach

Figure 4.5 – Formed chip in two different approaches

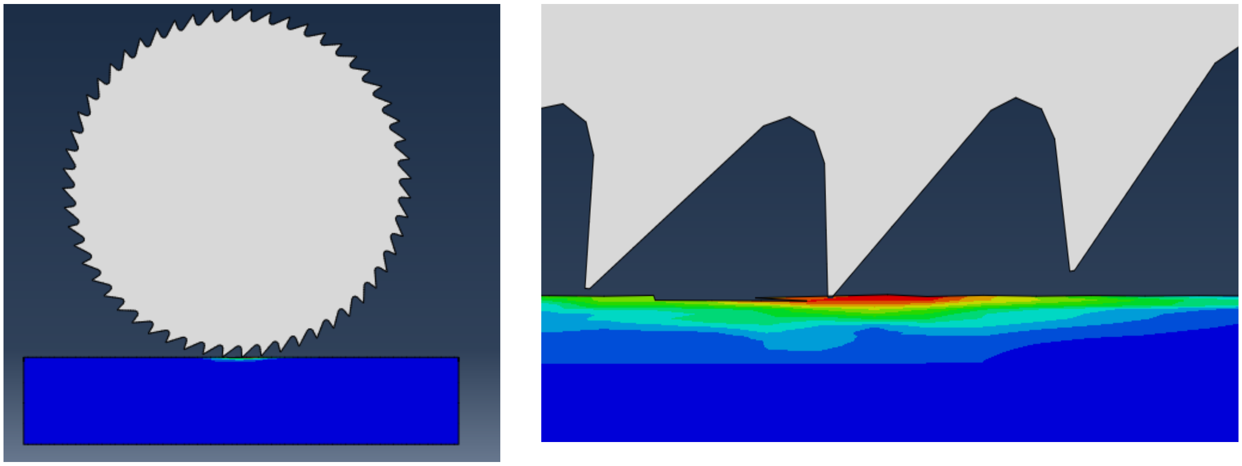

Figure 4.6 – Simulation with the whole blade

Figure 4.7 shows that average cutting and thrust forces vary with cutting speeds. It has been expected that the values obtained from analysis of forces using the three different methods at the same RPM will not be the same due to the differences in geometry and computation. However, all methods follow similar trend where increasing the spindle speed results in decreasing forces. Results from FE simulations that used models for tooth and blade showed insignificant change when the cutting speed increased from 285 to 315 *rpm*. A possible reason for the force to decrease as cutting speed increases can be faster rate of material shearing at higher cutting speeds.

The increase in the shear stress due to an increase in the spindle speed can also be seen in Figure 4.8. Although the increase is not considerable for one tooth simulations, the shear stress for circular blade runs rises especially between 285 to 315 *rpm*. In the modeling of whole blade, the simulation runs for a short time at the beginning of the cutting process. When the first tooth touches the workpiece for the first time and when the blade just starts to rotate, the contact with workpiece will be for a short period. Therefore, this first impact condition is likely to result in difficulty to cut through the material.

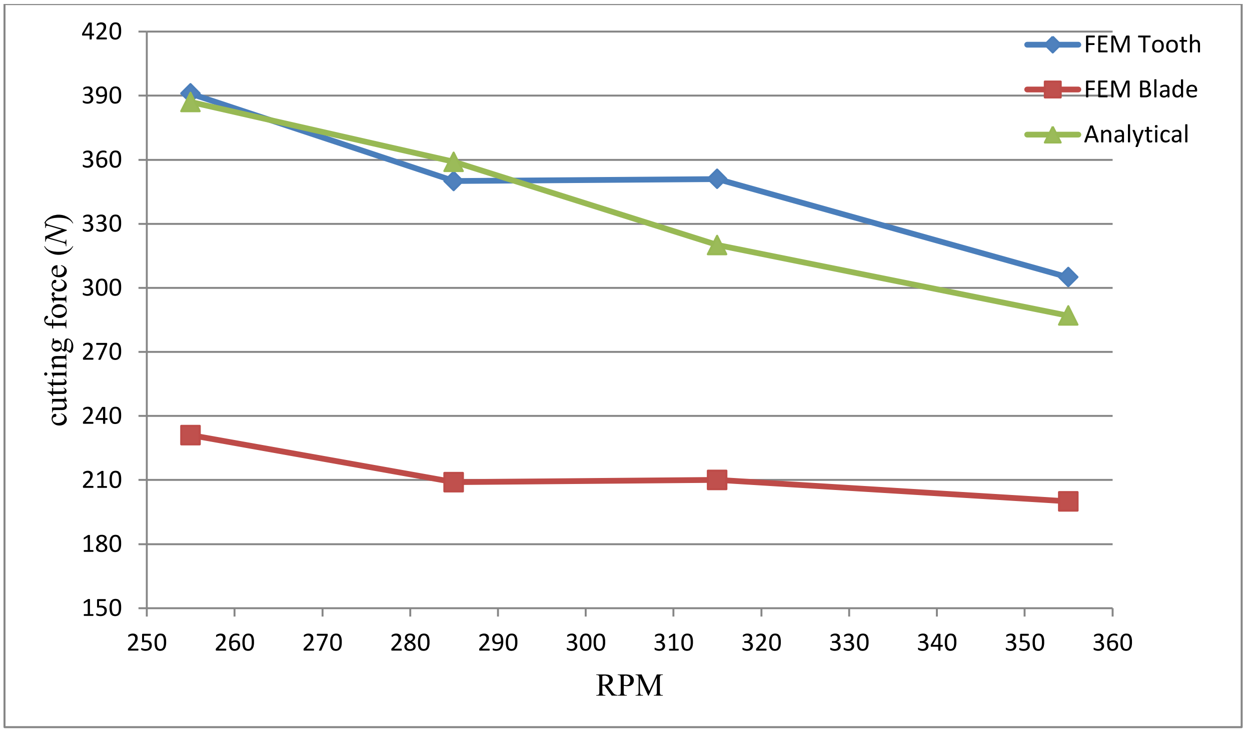

(a) Cutting force

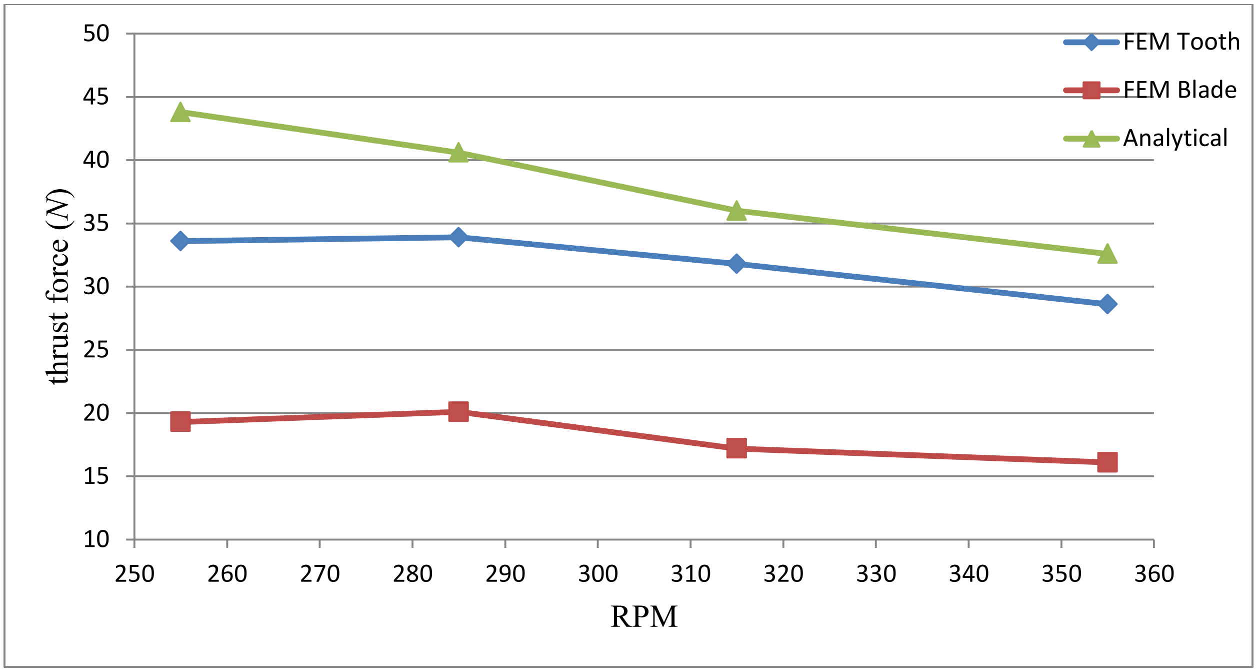

(b) Thrust force

Figure 4.7 – Cutting force for different cutting speeds

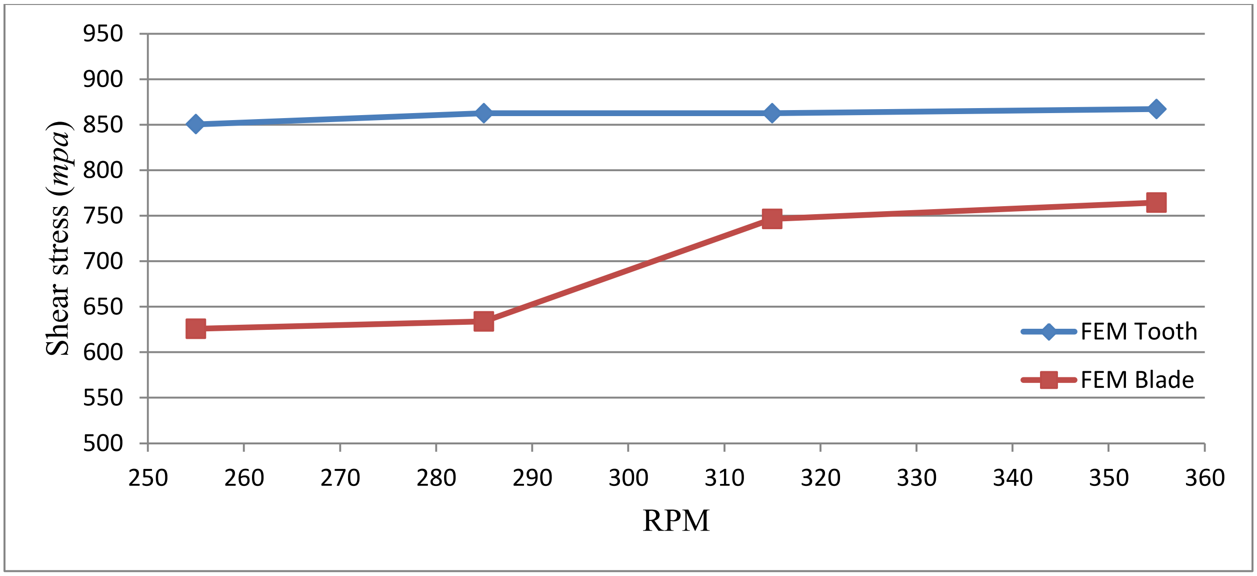

Figure 4.8 – Shear stress variation in depends on cutting speed

Figure 4.9 (a) shows that as the spindle speed increases, the shear angle decreases. To justify this trend, the relation shown in (4.2) is used.

$$\phi = tan^{-1}\left(\frac{dt_0\cos(\alpha)}{dt - dt_0\sin(\alpha)}\right) \tag{4.2}$$

where, *dt* is the deformed chip thickness. It is seen in Figure 4.9 (b) that the chip thickness increases as the cutting speed increases. The uncut chip thickness and rake angle in the above equation are kept constant for all simulations. Therefore, it can be said that the shear angle decreases at higher chip thickness values.

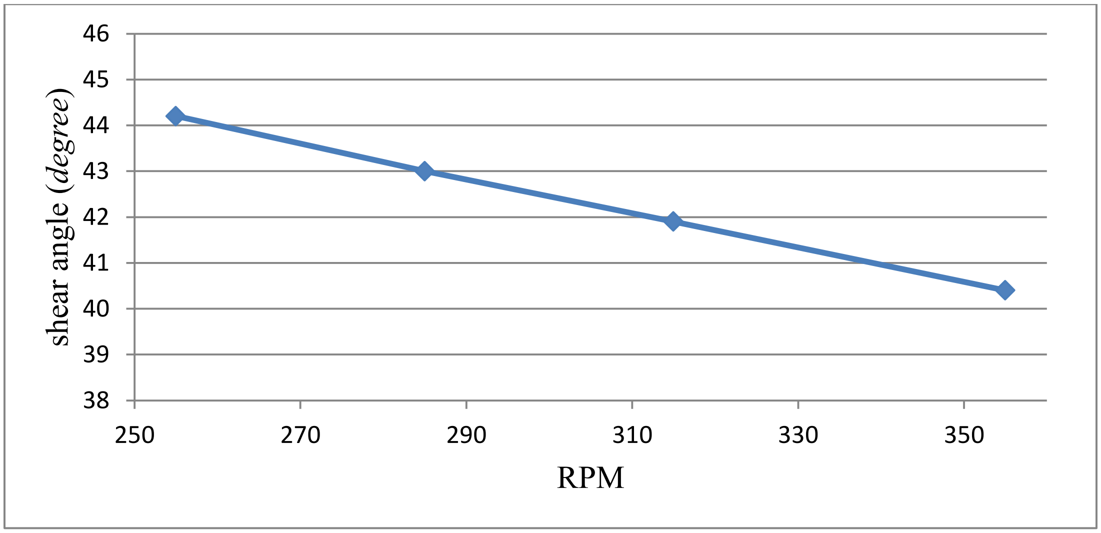

(a) Shear angle

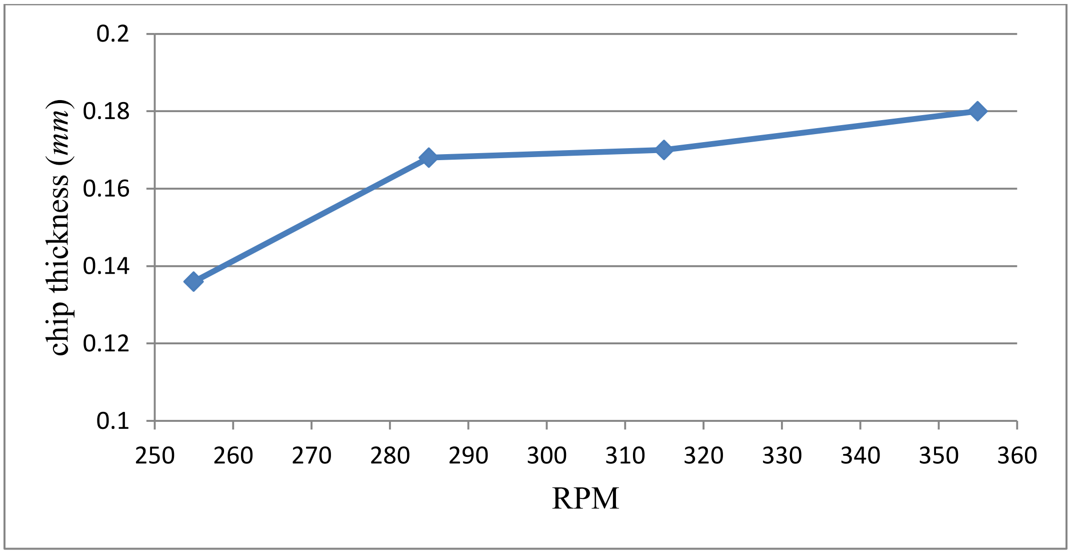

(b) Deforemd chip thickness

Figure 4.9 – Shear angle variation

4.3 Force calculation for a complete slotting process

In this section, results from the force calculation performed for the entire slotting process according to the approach presented in the previous chapter are discussed. In the computations shear angle is related to several parameters including uncut chip thickness. The uncut chip thickness is taken as time varying during the cutting operation. The shear angle for maximum uncut chip thickness determined in the previous section is used. Results from simulations that are done to predict the shear angle for time varying uncut chip thickness are presented. All parameters are fixed in the simulations while shear angle is calculated by changing only depth of cut. The 2D simulations were done in AdvantEdge cutting simulation software by applying its sawing module. The process parameters and geometries pertaining to the simulations conducted are shown in Table 4.6.

Table 4.6 Input parameters for the whole cutting process

Blade diameter (in)	3.07	**Pipe thickness (in)**	0.362
Blade rake angle (degree)	2	**Pipe diameter (in)**	7
Blade relief angle (degree)	30	**O.D. slot length (in)**	1.842
Teeth edge radius	0.01	**Friction coefficient**	0.5
Blade teeth number	56	**Pipe thickness (in)**	0.362
Blade thickness (in)	0.023	**O.D. Feed rate (in/min)**	3
Cutting speed (in/sec)	43	**I.D. Feed rate (in/min)**	2
RPM	255	**Final Feed rate (in/min)**	4

By solving the mathematical model for uncut chip thickness given in (3.23), 1,216 unique data points are obtained from all 8,736 data points by eliminated repeated points. It should be noted that the whole process for this case takes 16 *sec* (t_3) where the simulation increment is 0.1 *sec* for a blade with 56 teeth.

As the resources available for this research did not allow all the 1,216 simulations to run, 20 data points have been selected for simulation. The remaining data points were filled using linear interpolation to predict results based on the 20 data points simulated. The resulting shear angle for the simulated data points along with their forces from both FEM and the analytical model presented in section 3.6 are shown in Table 4.7.

Table 4.7 shear angle and forces from FEM

Depth of cut (mm)	***Shear angle (degree)***	***Fx (N)***		***Fy (N)***	
		FEM	***Analytical***	***FEM***	***Analytical***
0.001	9.2	9	3.2	10	1.5
0.002	10.3	10	4.7	17	2.2
0.0054	16	12	9	20	4.1
0.007	16.8	14	11.2	25	5.1
0.01	16.9	18	16.1	28	7.35
0.02	17.3	37	32.7	35	14.9
0.03	17.6	50	46.5	43	21.2
0.04	18	75	62.1	48	28.3
0.055	18.5	105	87.2	50	36.2
0.07	18.9	118	99.9	54	46
0.09	19.6	130	125.9	57	57.3
0.1	19.8	138	142.6	60	63.4
0.105	20	140	145.4	60	66.2
0.13	20.7	168	176.6	82	80.5
0.16	21.5	215	204.2	95	96
0.19	22.2	260	248.9	115	113.1
0.21	22.6	275	270.5	134	122.5
0.24	23.4	310	304	140	138.2
0.26	23.7	340	322	147	144.6
0.28	24.1	360	348	150	156.3

Based on orthogonal cutting theory, the chip compression ratio (r_c) is defined as [12]:

$$r_c = \frac{dt_0}{dt} \tag{4.3}$$

where, dt and dt_0 are deformed and unreformed chip thickness, respectively.

In general, as the uncut chip thickness increases, the difference between uncut and deformed chip thickness reduces resulting in an increase in chip compression ratio. Shear angle is also related to chip compression ratio according to (4.4). Therefore, it can be said that by increasing uncut chip thickness, the shear angle is increased which is also true in this study as shown in Table 4.7.

$$\phi = tan^{-1} \frac{r_c \cos \alpha}{1 - r_c \sin \alpha} \tag{4.4}$$

Fermaniuk [92] measured formed chip thickness on the same machine configuration and showed the relationship between shear angle and deformed chip thickness as:

$$\phi = tan^{-1} \frac{F_{Tooth}}{dt} \tag{4.5}$$

where, F_{Tooth} is the feed per tooth in microns which can be calculated by using (4.6) for which feed rate can be obtained from (3.18) and (3.19).

$$F_{Tooth} = \frac{v_f(t)}{RPM\ .N} * 25400 \tag{4.6}$$

Fermaniuk [92] measured deformed chip thickness between 15.6 to 45.3 micrometers. The mathematical measured chip thickness for this case is between 9.04 to 59.4 micrometers and two data points were 127.9 and 142.5 micrometers. The deviation of these values can be justified by the small predicted values for the shear angles. The cutting parameters are also different with the blade tooth having a triangular shape in this study while it was curvilinear in the work referred.

Modeling the cutting forces is also considered for a blade which has completed cutting several slots. In this case, the blade teeth are dull, but have not yet been replaced or re-sharpened. Therefore, the cutting process outputs are compared for two different cases. The firs case is for a sharpened blade considered in its first initial cut. Another case is when the blade teeth are not the same shape as their original ones, but still are mounted on the slotting machine to finish cutting slots. The round edge tool for the dull blade case is selected as $0.5mm$ shown in Figure 4.10 as it is close to the observation with the actual blades.

Figure 4.10 – Different shapes of dull teeth

Three FE simulations are conducted to find the values of shear angle and stress. All cutting parameters are kept the same during simulations for the 0.5*mm* and 0.01*mm* round edges, except tooth edge radius. Table 4.8 shows the results for dull tooth shear angle. The difference in shear angle for both cases is between 5.4 to 6.7 degrees. Therefore, an angle of 6^o is subtracted for all shear angle data points in the sharp case to save the cost of simulations. The shear stress for dull is 733 *MPa* which was greater than the previous case (633*MPa*).

Table 4.8 shear angle for the sharp and dull tooth

	0.01*mm* depth of cut	**0.2*mm* depth of cut**	**0.28*mm* depth of cut**
0.01 *mm*	16.9	19.8	24.1
0.5 *mm*	11.4	13.1	18.7

Figure 4.11 shows the numbers of teeth that are in contact with the workpiece during the cutting process. Since the cutting parameters and slot geometry are the same for both cases, the number of teeth is also taken to be similar.

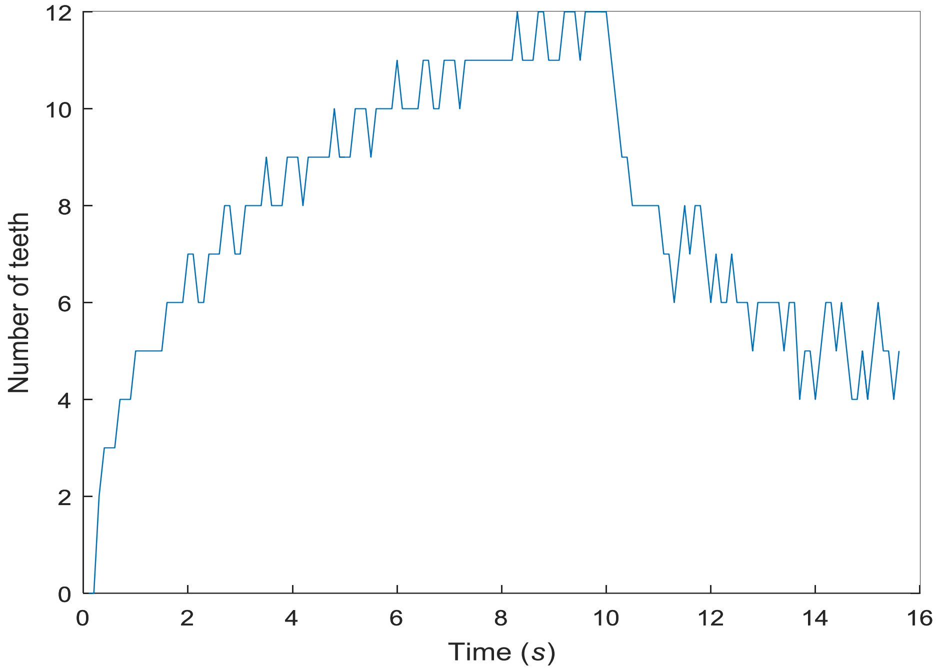

Figure 4.11 – Number of teeth result in contact with the workpiece

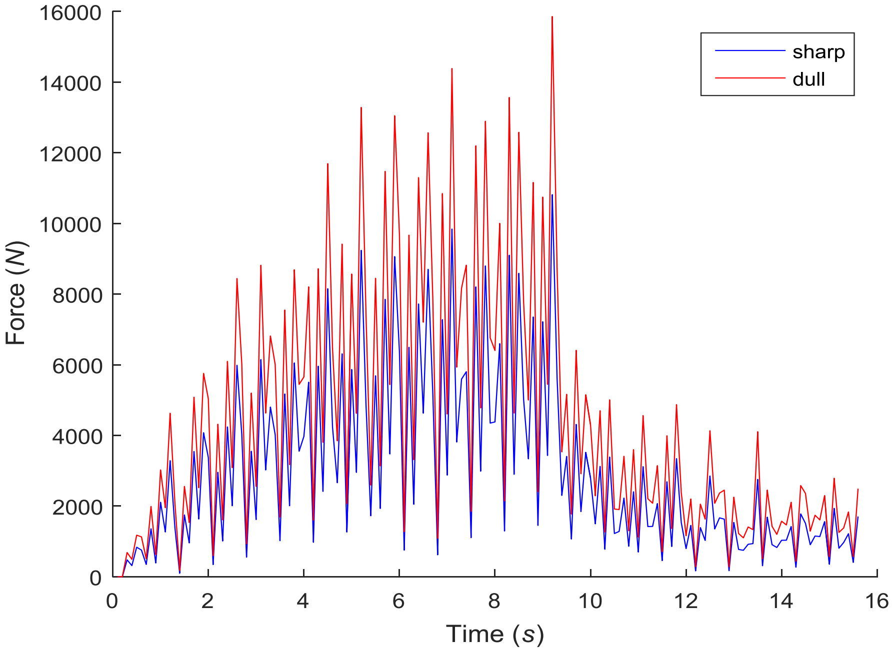

(a) *x* direction

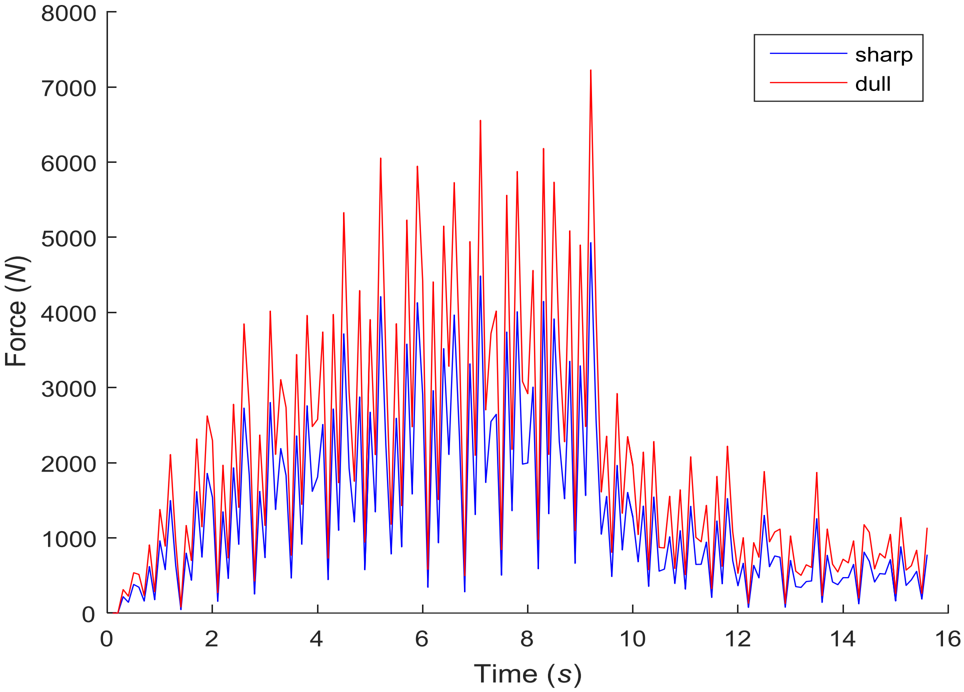

(b) y direction

Figure 4.12 – Cutting force result

As seen from Figure 4.12, the forces are greater when the maximum number of teeth is in the workpiece just before time t_2 and before cutting through the workpiece. It is also shown that a dull blade requires greater force to cut a slot and should be replaced or re-sharpened.

The friction coefficient was selected as 0.5 in this case and the following condition was used to check the validity:

$$\mu = \alpha + tan^{-1}\left(\frac{F_y}{F_x}\right) = \frac{F_u}{F_v} \tag{4.7}$$

In all three cases results from the analytical model confirmed 0.5 can be taken for the friction coefficient.

The resultant shear and friction power are shown in Figure 4.13. Although shear power for the dull blade is greater than that for a sharp blade, the friction power for both cases is similar. This is because the friction coefficient for both cases is the same, but it is expected that cutting process using a dull tooth will have a greater friction coefficient. The cutting power drawn from the spindle is shown in Figure 4.14. In theory this power should be equal to the summation of shear and friction powers. Comparison of corresponding plots shown in Figure 4.13 and Figure 4.14 confirms this expectation.

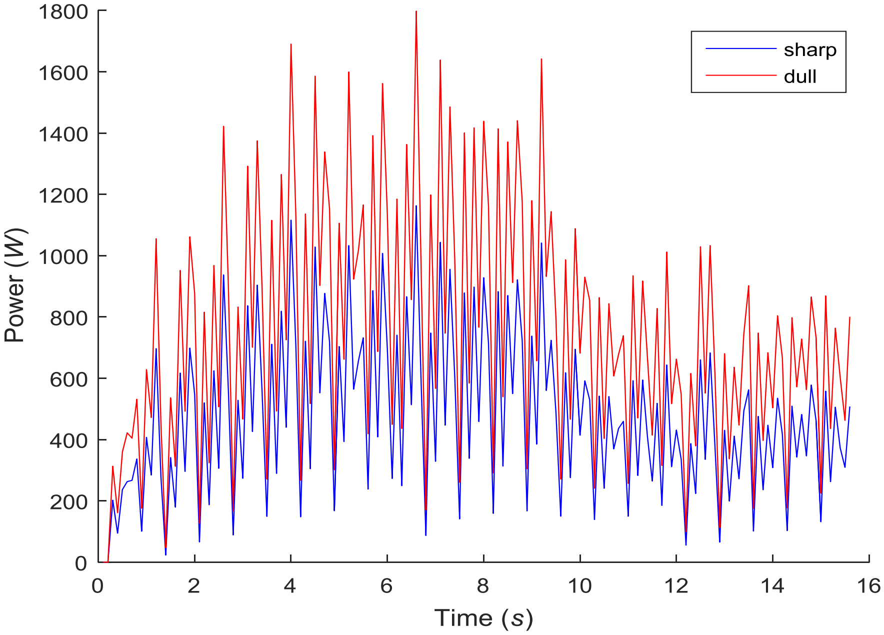

(a) Shear power

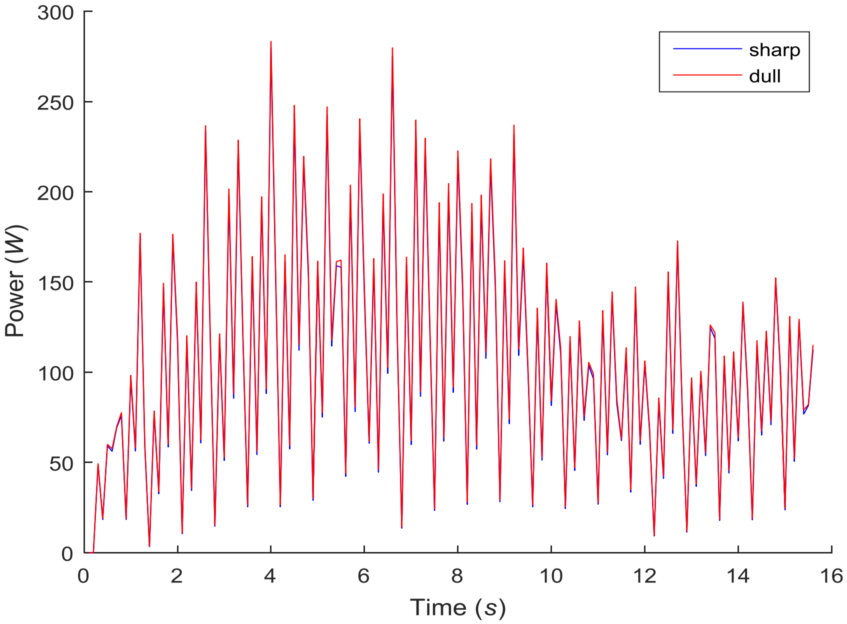

(b) Friction power

Figure 4.13 – Friction and shear powers

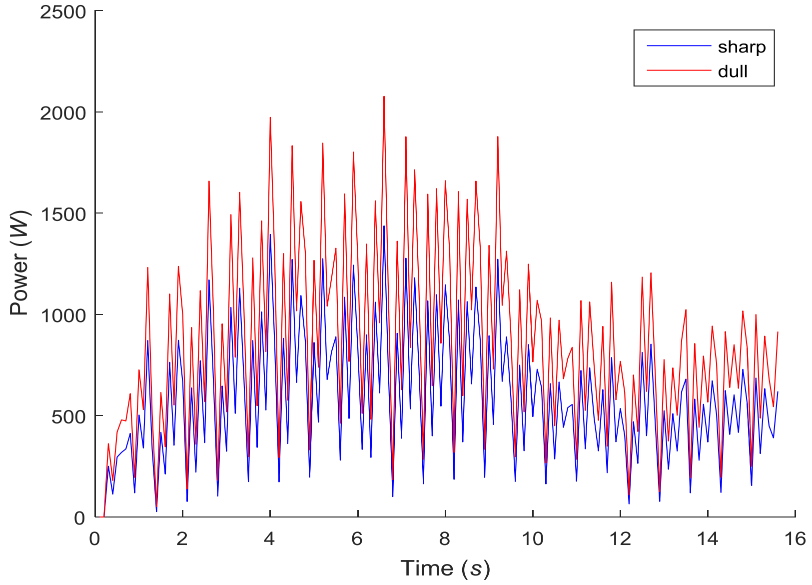

(a) Cutting power drawn from the spindle

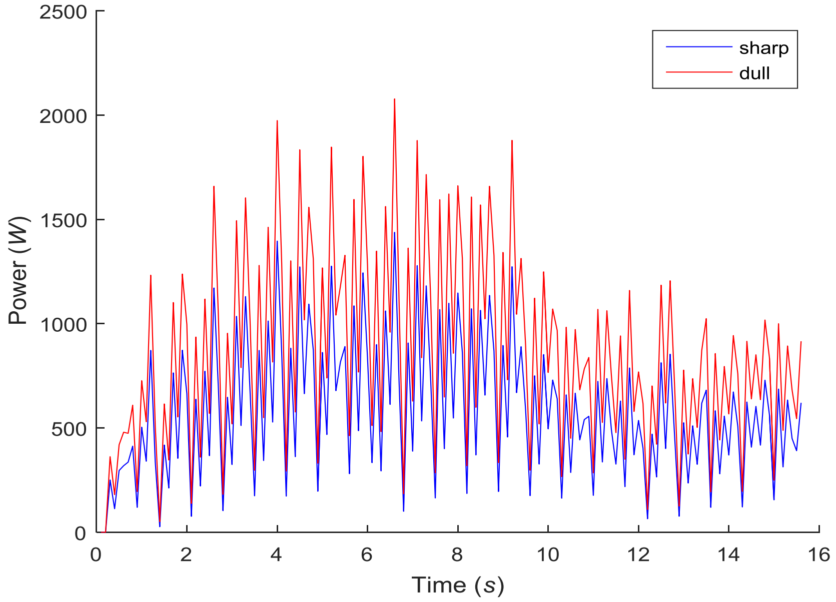

(b) Summation of shear and friction powers

Figure 4.14 – Cutting powers

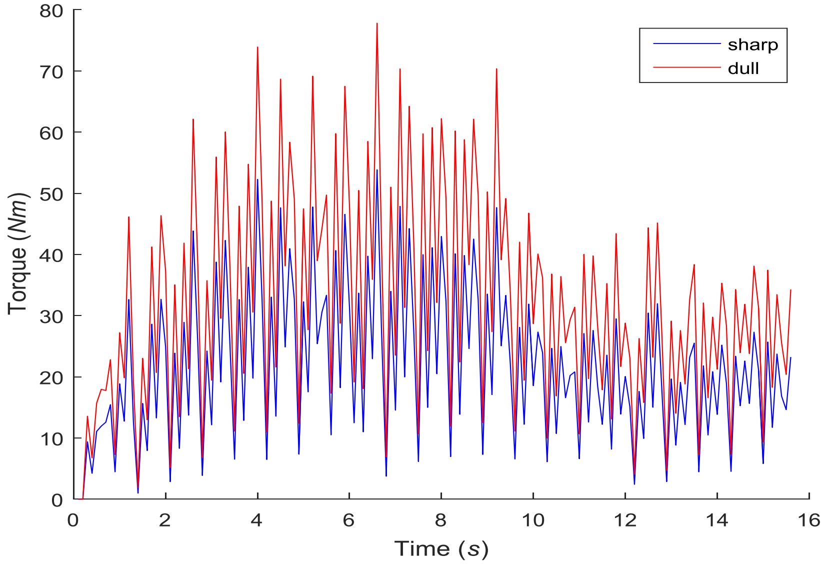

(a) Torque applied by the spindle

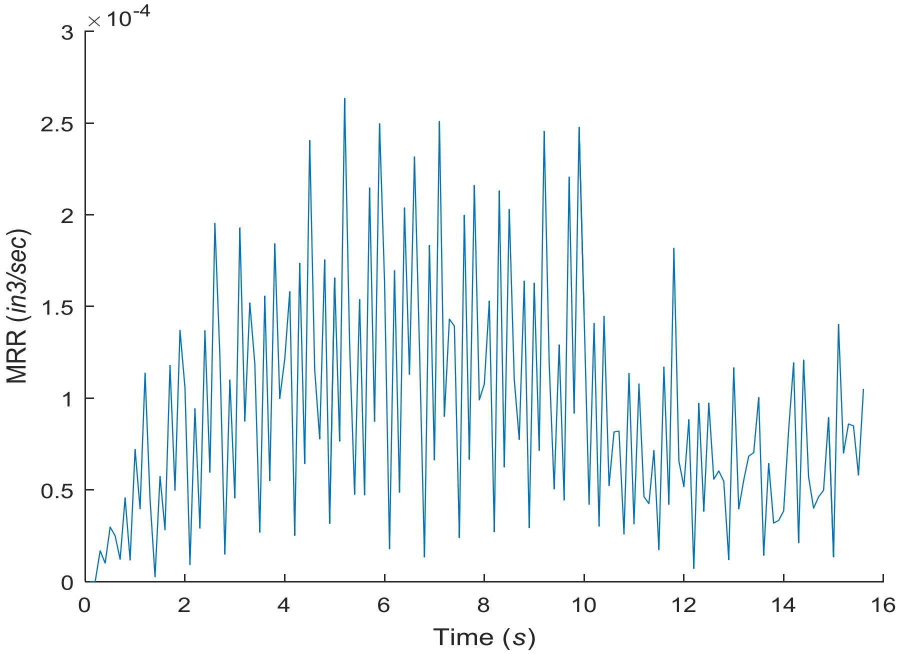

(b) Material removal rate

Figure 4.15 – Torque and MRR

The torque from the spindle and material removal rate are shown in Figure 4.15. Higher torque is drawn from the spindle for blades with greater round edge due to higher applied force in *x* direction. The material removal rate depends on cutting speed, feed rate, slot dimensions, and number of teeth on the blade. Since all these parameters have the same values for both cases, it remains the same. The values for the material removal rate obtained from the calculation also meet expectations since its summation value is close to the volume that should be removed from the pipe to create a slot.

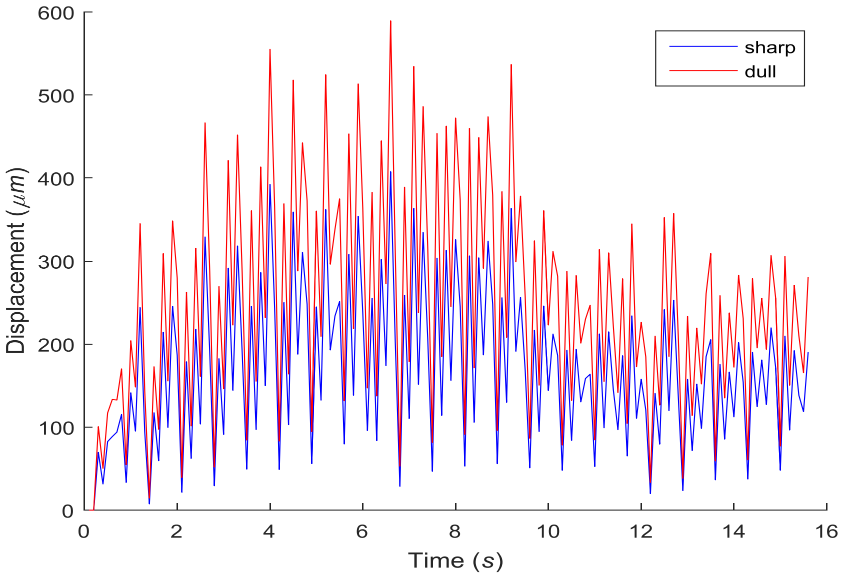

(a) In *x* direction

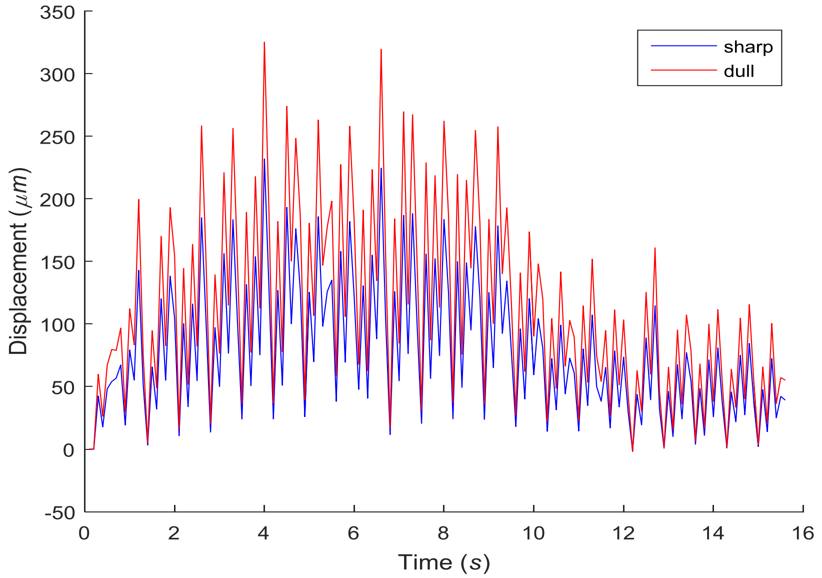

(b) In *y* direction
Figure 4.16 – Blade displacement

Figure 4.16 shows the blades displacement in *x* and *y* directions. As predicted, the displacements in both directions are greater for a dull blade than a sharp one. The reason is that the displacement highly depends on the forces applied to the cutting tool. Monitoring tool displacement is important since it generates chatter vibration and affects the surface quality of the workpiece and also the tool life. In addition, it is obvious that the maximum displacement for both cases in *x* and *y* directions occurs at the time when the maximum number of teeth are in contact with the workpiece and, as a result, the maximum force applied to the blade.

Figure 4.17 shows the stability lobe diagram based on the force calculated for the sharp blade. The blade stiffness is 2.4e7 N/m and dimensionless damping ratio is selected as 0.04. the maximum cutting force coefficient for the time that 12 teeth are engaged is 3.1e10 N/m2. It is possible to determine the stable and unstable regions. These regions are the combination of spindle speed, rpm, and depth of cut. Therefore, it is possible to choose the spindle speed and depth of cut in a stable region to avoid tool chatter. It should be noted that by knowing the maximum value of depth of cut, the value of feed rate can be predicted.

Based on the selection of the rpm value, feed rate, and maximum depth of cut that are selected for the sharp blade in this section, and also looking at Figure 2.18, it can be find that the process is stable (255 rpm and 0maximum 0.01 mm depth of cut) and there is no chatter in a case of having sharp blade.

Figure 4.18 shows the frequency is calculated for the sharp blade using Fast Fourier Transform (FFT). The peaks that are shown in Figure 4.18, are tooth passing frequency due to the spindle speed of 255rpm. Since the process is stable, no chatter can be seen in the picture.

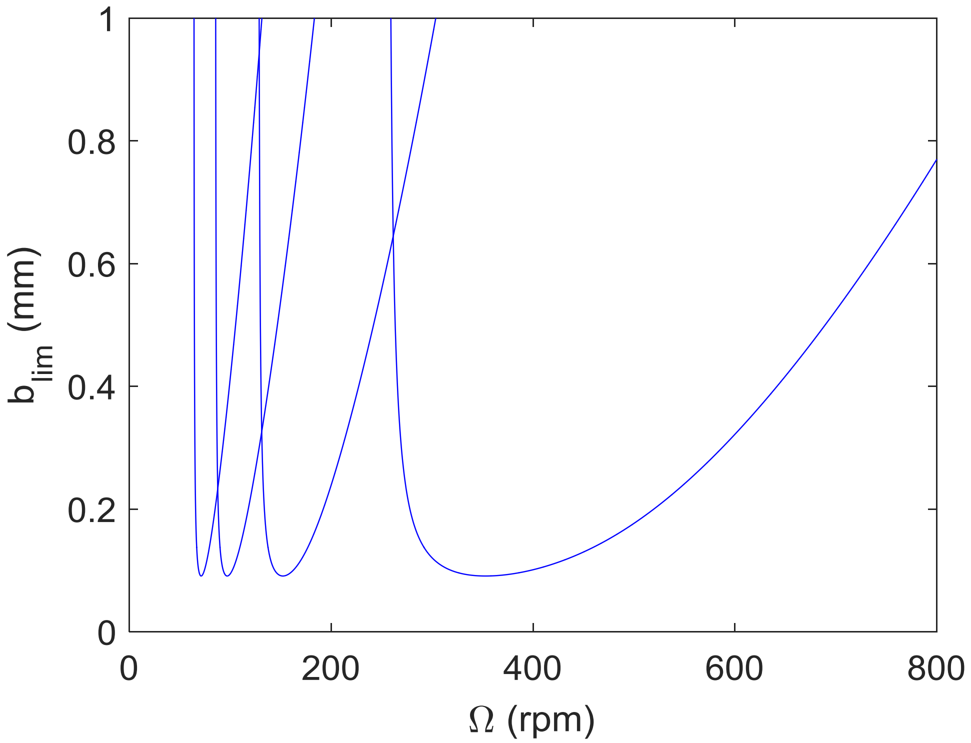

Figure 4.17 – Stability lobe diagram

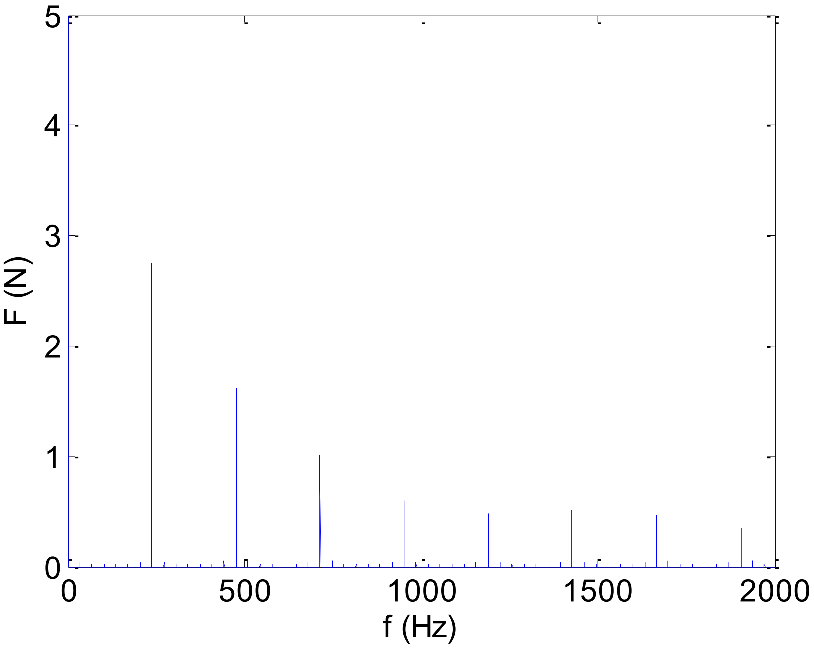

Figure 4.18 – Frequency vs force for the sharp blade

4.4 Comparison between different blades and workpieces

Pipes L-80 and K-55 are the most commonly used for slotted liners produced by RGL. In addition to the HSS M2 blade, the HSS M35 blade is also used to make the slots on the pipes. Therefore, the same cutting parameters and blade geometries presented in Table 4.6, Table 3.2, Table 3.3 andTable 3.4 are applied for the three different cases shown in Table 4.9. The first is the case where a sharp HSS M2 blade is used for slotting an L-80 pipe considered in Section 4.3. Case 2 is for using HSS M35 to slot an L-80 pipe while the last case uses HSS M2 on K-55 pipe.

Table 4.9 Comparison of different blades and pipes

Case	**Tool**	**Workpiece**
1	M2	L-80
2	M35	L-80
3	M2	K-55

Five simulations are conducted for Cases 2 and 3 to predict the shear angle for different depth of cuts. Table 4.10 shows the shear angle measured from finite element simulations. It is found that Case 2 has shear angle that is 1.6° to 3.8° greater than case 1. Based on the same simulations for Case 3, it is observed that it has shear angles that are 0.3° to 1.1° smaller than Case 1. In order to save cost of simulation, by knowing the approximate range of shear angles, and since the error from shear angle calculation does not considerably affect the cutting force calculation, the shear angle for the rest of different depth of cut data is calculated by using linear curve fitting. The measured shear stresses from simulations were 633, 680, and 610 MPa for Case 1, 2, and 3, respectively. These values of shear stress are considered to be within a reasonable range. For instance, as the material of L-80 pipe is harder than the K-55 pipe, more shear stress for Case 1 is expected than Case 2 (note that Case 1 and 2 have the same tool material).

Table 4.10 Obtained shear angle for different Cases

Case	**0.01 mm depth**	**0.1 mm depth**	**0.16 mm depth**	**0.21 mm depth**	**0.28 mm depth**
1	16.9	19.8	21.5	22.6	24.1
2	18.5	21.3	24.5	25.4	27.9
3	16.6	19	20.5	21.9	23

The resulting forces for all three Cases are shown in Figure 4.19. Distinguishing between plots is not easy since the values of forces are close to each other. Therefore, the average cutting, thrust, and total force calculated from analytical model is determined and is shown in Figure 4.20.

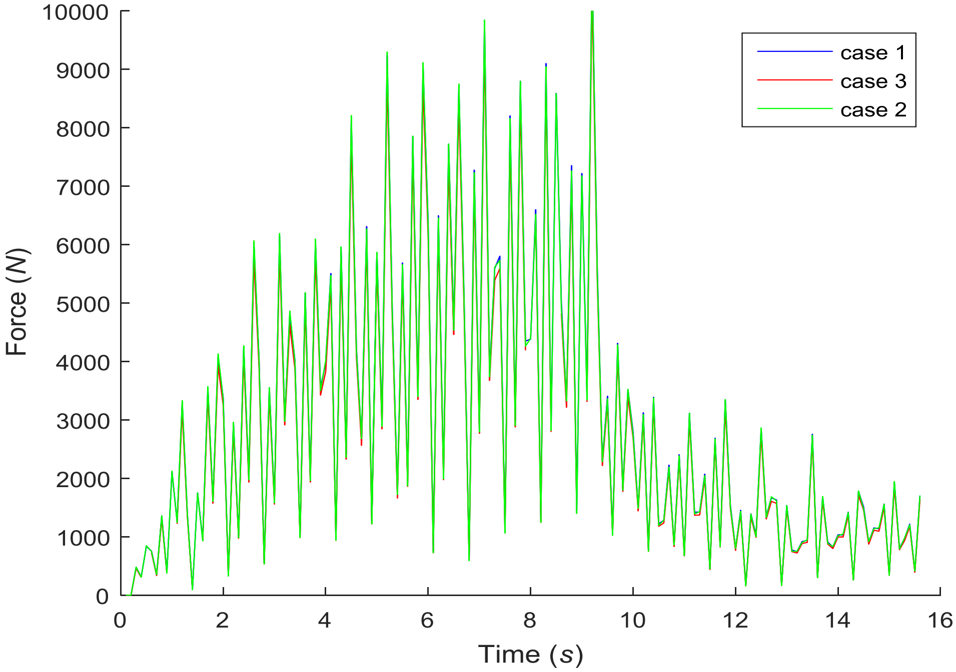

(a) In *x* direction

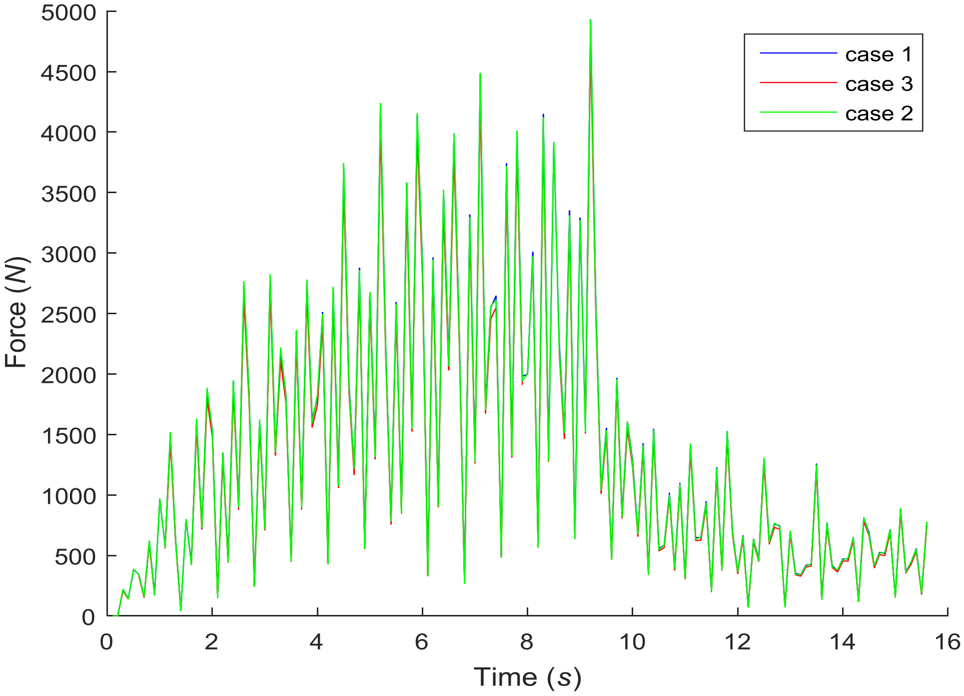

(b) In y direction

Figure 4.19 – Force calculation for different blade and pipe materials

It is seen that using M2 blade as a cutting tool to manufacture slots on the pipe L-80 (Case 1) requires more force than using for pipe K-55 (Case3). This result can be readily justified since the pipe L-80 is of a harder material, requiring a greater force to remove the material from its surface. It is seen that both forces in x and y directions have higher value for the workpiece having higher material strength, and as a result the total force, $F = F_x + F_y$, is greater as well. It is also understood that the main factor which increases the force in case 3 from its value in case 1 is the shear stress, since all other factors are the same and the difference between shear angles is negligible.

From Figure 4.20, it was noticed that the forces between Cases 1 and 2, having the same pipe material (L-80) but different blades (M2 and M35), was close and Case 1 requires a force that is only slightly greater than that in Case 2. In addition, using blade M35 involves higher shear stress than Case 1, but generates lower cutting forces. The reason for this can be the increase in the shear angle when using blade M35 which causes the force to be lower than Case 1.

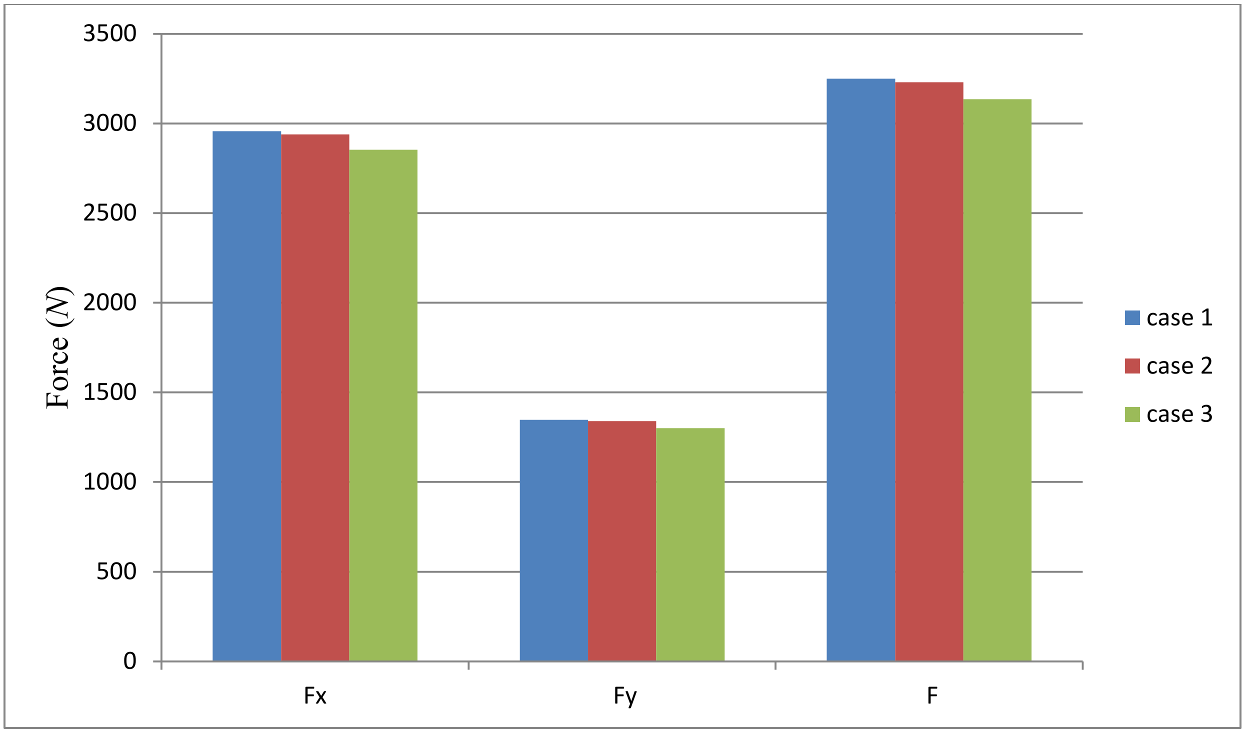

Figure 4.20 – Average calculated force for different tool and pipe material

Since both torque and power drawn from the spindle depend on the cutting force in *x* direction and cutting force case 1 decreases to case 3, it was expected that case 1 will have a higher torque and power. Case 3, on the other hand, has the lowest torque and power as shown in Figure 4.21.

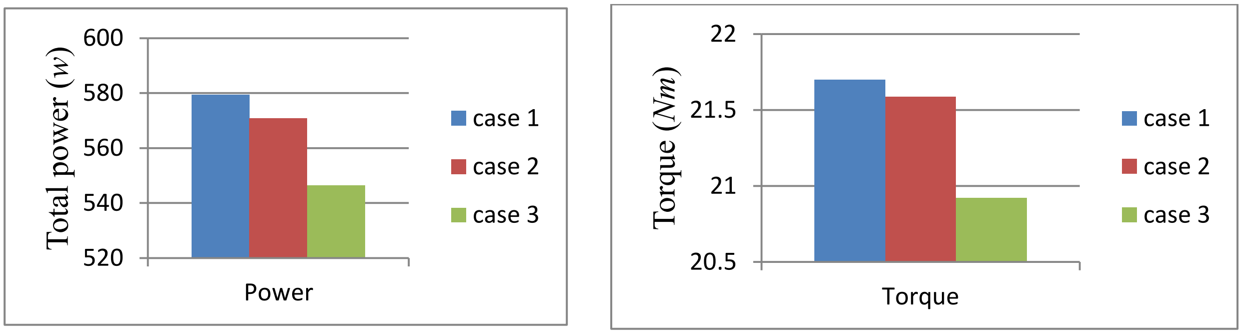

(a) Power drawn from spindle (b) Torque drawn from spindle

Figure 4.21 – Average power and torque for different tool and workpiece material

Figure 4.22 shows the average and maximum displacements in both *x* and *y* directions for all three Cases. Since the displacements are only affected by forces, the average displacements decrease from Case 1 to Case 3. The greatest displacement for all Cases occurs around 7 seconds when the maximum numbers of teeth are in contact with the workpiece. Therefore, higher force is applied to the blade at this time and the angle that shows active teeth to the pipe is large. It was interesting to see that maximum displacement in both *x* and *y* directions for using M35 blade are higher than M2 blade by only a small amount in the case of having L-80 pipe. As all parameters except shear stress and shear angle are kept the same for both Cases, this is attributed to the presence of the trigonometric functions in the analytical models used for the calculations.

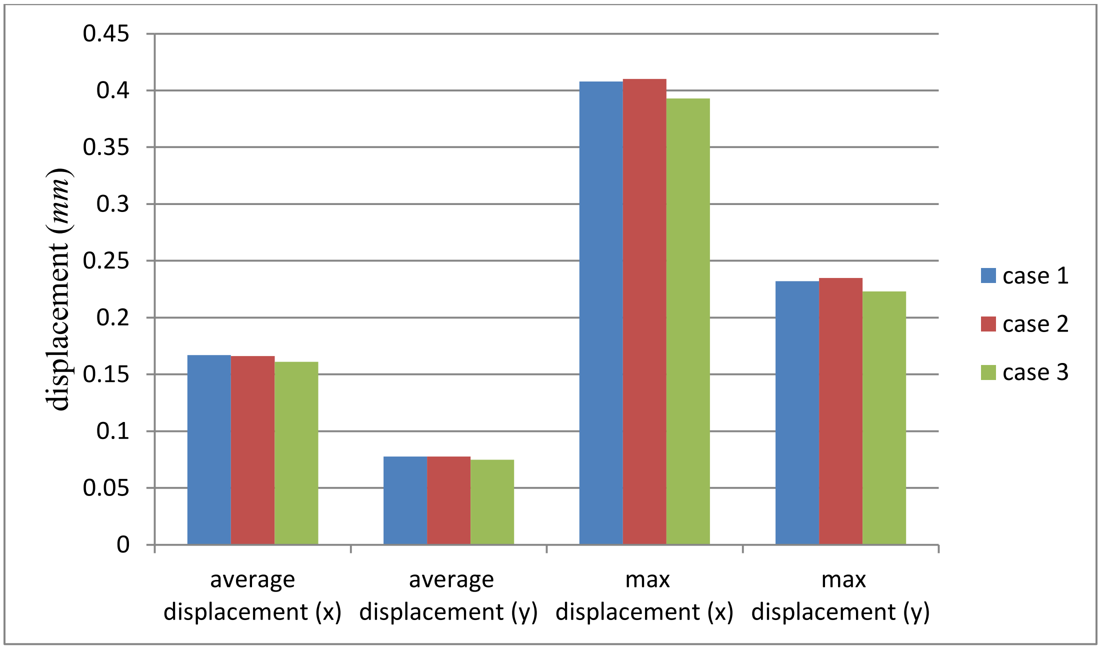

Figure 4.22 – Average calculated force for different tool and pipe material

5. ANALYSIS OF BLADE DYNAMICS

Circular saw blade is the only type of cutting tool used by RGL to manufacture slotted liners. Oscillation of the blades could be seen as the major concern in the cutting process, since it affects surface roughness, tool life, and vibration. When the blade reaches its critical rotation speed or one that is close to its natural frequency, it will no more be stable and actions are required to avoid considerable vibration leading to shorter tool life.

Although rotational speeds of saw blades are higher at lower thicknesses, this affects the lateral stiffness [95]. High vibrations can be expected for a thin blade especially working at the greater speeds. In this case immediate overcoming actions could be reducing both rotational speed and feed rate which adversely affects the cutting efficiency.

It has been recently common to apply circular blades that have radial or annular slots on themselves. The main purposes of using these blades to make slots that are symmetrical about the blade center are to reduce vibration and noise as well as increasing thermal dispersion efficiency especially when operating at high rotational speeds. Experimental measurement have reported that blades having radial slots can reduce vibration due to geometrical discontinuity [96].

Stakhiev [97] presented three rotational speeds for a stable circular saw blade as:

$$n_u = 0.31 - 0.4\, n_{cr} \tag{5.1}$$

$$n_0 = 0.59 - 0.696\, n_{cr} \tag{5.2}$$

$$n_p = 0.85\, n_{cr} \tag{5.3}$$

where, n_u, n_0, n_p, and n_{cr} are universal, optimal, permissible, and minimum critical rotational speeds, respectively.

Permissible rotational speed is the maximum speed that a blade can rotate at when it is at stable condition. Permissible speed is usually specified by the blade manufacturer. However, it has been seen that, in most cases, the specified permissible speed is higher than the actual one obtained from measurement. Therefore, minimum critical rotational speed which depends on the blade's natural frequency has to be defined in order to obtain permissible speed.

5.1 Blade natural frequency calculation

Natural frequency of the considered circular saw blade is obtained by both analytical and finite element software. The geometries and mechanical properties for the selected blade are shown in Table 5.1.

Table 5.1 Properties of blade HSS M2

Outer diameter	3.073 *in*	**Young's modulus**	214 *GPa*
Bore diameter	1 *in*	**Poisson ratio**	0.3
Number of teeth	56	**Density**	8160 kg/m^3
Blade thickness	0.023 *in*	**Tooth pitch**	0.172 *in*
Tooth height	0.082 *in*	**Gullet radius**	0.023 *in*
Rake angle	2 *degree*	**Relief angle**	30 *degree*

Analytical method

The vibration of circular blades can be expressed using classical theory of the thin plates [98] which gives the following differential equation:

$$\left(\frac{\partial^2}{\partial r^2}+\frac{1}{r}\frac{\partial}{\partial r}+\frac{1}{r^2}\frac{\partial^2}{\partial \theta^2}\right).\left(\frac{\partial^2}{\partial r^2}+\frac{1}{r}\frac{\partial}{\partial r}+\frac{1}{r^2}\frac{\partial^2}{\partial \theta^2}\right)W(r,\theta,t)+\frac{\rho.h}{D}.\ddot{W}=0 \tag{5.4}$$

where, h is the blade thickness, ρ is the density of the material, and D is the bending stiffness such that:

$$D=\frac{E\,h^2}{12(1-\nu^2)} \tag{5.5}$$

where, E is the young's modulus, and ν is the poisson ratio. Since the above equations have been solved by applying theoretical calculation and Bessel function in previous studies [98], the natural frequency becomes:

$$\omega = \frac{h}{D^2}\sqrt{\frac{E\,\alpha}{12\rho(1-\nu)}} \tag{5.6}$$

where, ω is circular frequency in radians, D is circular saw blade diameter, and α is coefficient which depends on the number of nodal diameters and clamping ratio. Therefore, natural frequency can be obtained from:

$$f_{s(n)} = \frac{\omega}{2\pi} \tag{5.7}$$

where, $f_{s(n)}$ is the natural frequency of an idling blade at nodal diameter *n*.

Two different moving waves are involved in an oscillation of a circular saw blade. These waves travel in opposite forward and backward directions. The frequency of forward and backward waves can be calculated by [99]:

$$f_f = f_{r(n)} + \frac{n.RPM}{60} \tag{5.8}$$

$$f_b = f_{r(n)} - \frac{n.RPM}{60} \tag{5.9}$$

where, f_f, f_b, $f_{r(n)}$ are frequency of forward wave, frequency of backward wave, and natural frequency of rotating saw blade, respectively.

By increasing the rotational speed of the blade to the certain speed (critical rotational speed), the angular speeds of both blade and wave in the blade become equal. The backward travelling wave at this point except nodal diameter 0 and 1 becomes zero. In this time, a lateral force, even a small one can results in a great deflection in the circular saw blade which is known as resonance. It is possible to derive following equation from (5.9).

$$n_{cr} = \frac{60\,f_{r(n)}}{RPM} \tag{5.10}$$

The relationship between spindle speed and natural frequency of the rotating blade becomes:

$$f_{r(n)}{}^2 = f_{s(n)}{}^2 + \lambda \left(\frac{RPM}{60}\right)^2 \tag{5.11}$$

where, λ is centrifugal force coefficient and can be obtained from [99]:

$$\lambda = \frac{m_p - 1}{4m_p} n^2 + \frac{3m_p + 1}{4m_p} n \tag{5.12}$$

where, m_p is the coefficient of Poisson process ($m_p = 1/\nu$).

The critical rotational speed in rpm can be calculated by substituting (5.11) with (5.10) and becomes:

$$n_{cr} = \frac{60\, f_{s(n)}}{\sqrt{n^2 - \lambda}} \tag{5.13}$$

When the frequency of backward traveling wave becomes zero, it reaches the critical rotational speed and blade starts to vibrate in a resonance [100]. The critical rotational speed should be obtained for all reference modes and the lowest speed has to be considered as a critical speed as shown in Figure 5.1.

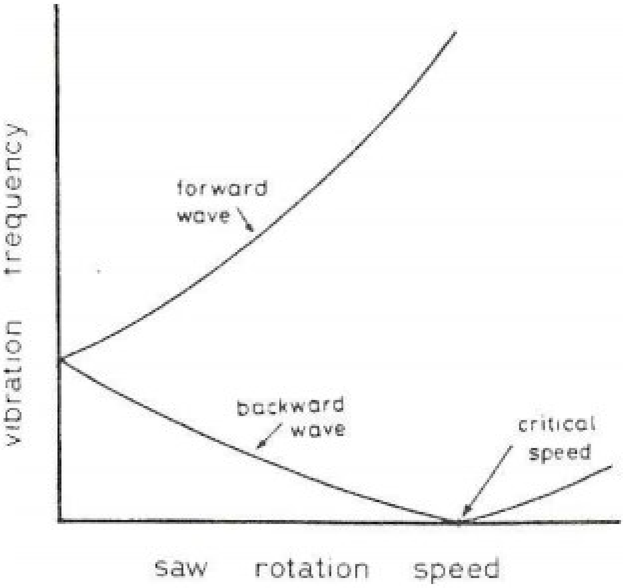

Figure 5.1 – vibration frequency and rotational speed of a circular saw blade [99]

Finite element simulation

Siemens NX, ABAQUS, and CATIA are used to obtain natural frequency of the blade for nodal diameters, n = 1, 2, 3, 4, in static modal analysis. The blade chosen here is M2 with 3.07 in outside diameter, 2° rake angle, 30° relief angle, 56 teeth, and 1 in clamping diameter (bore diameter). The bore diameter of blade has been used to fix the blade as shown in Figure 5.2 to find the natural frequency when it is not rotating. After creating the CAD model and assigning material to the part model, element type has been chosen to apply the mesh. The boundary condition is a fixed boundary condition for which the surface of inner diameter of the blade or bore diameter has been selected.

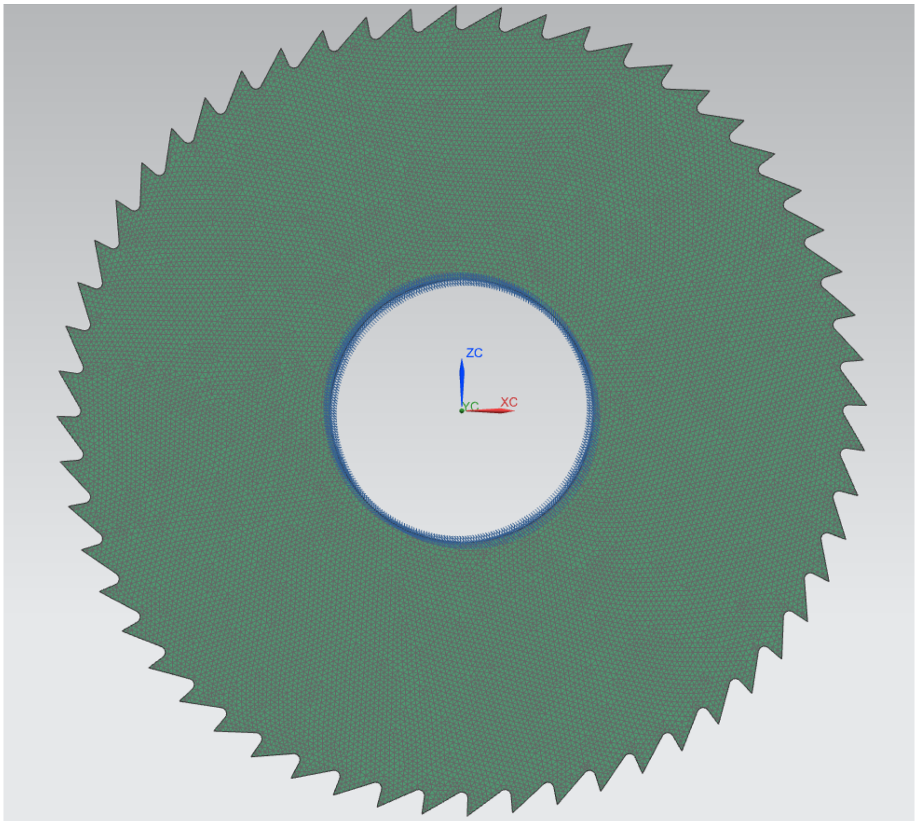

Figure 5.2 – A fixed blade for modal analysis

Natural frequency results

The natural frequencies for the first four modes are shown in Table 5.2 and Table 5.3. It has been found out that using NX SOL 103 with 3D four-sided solid elements with 10 grid points results in values of natural frequencies that are the closest to the calculated natural frequencies from the theory.

Figure 5.3 shows the mode shape results along with the greatest and lowest displacement for blade M2 using NX SOL 103. The errors between calculated and simulated natural frequencies are 0.7%, 0.4%, 2.8%, and 8.9% for mode 1, 2, 3, and 4, respectively. It can be seen that the difference for mode 4 is not desired. However, it is not possible to certainly conclude whether or not the error is from application of the theory or simulation. Experimental validation could have been used in this regard to validate the results. In addition, the approximate value of frequencies will help to avoid resonance phenomena, and also the first mode of blade natural frequency is more important since the system can reach at it at first.

Table 5.2 FEM natural frequency for blade M2

Software	**Mesh**	**No. of elements**	**No. of nodes**	**Time (min)**	**Frequency mode (Hz)**			
					1	**2**	**3**	**4**
NX	HEX8	126310	190599	15.26	741.91	874.17	1357.7	2180.82
NX	TETRAL10	105422	160645	3.46	742.89	875.14	1358.41	2181.51
NX	TETRAL10	538278	812999	247.6	705.99	831.658	1291.19	2073.489
ABAQUS	C3D6	105332	80811	1.48	740.18	879.18	1372.5	2206.6
ABAQUS	C3D6	16136	16776	0.19	832.48	997.53	1550.8	2475.5
ABAQUS	C3D6	646701	435964	52.23	718.72	846.09	1313.8	2110.6
ABAQUS	C3D6	62330	93573	1.7	613.16	723.56	1125.1	1807.5
CATIA	TETRA10	3808	8561	0.51	861.06	1038.2	1537.18	2501.73
CATIA	TETRA10	8591	18454	2.3	747.93	881.93	1366.2	2193.6
CATIA	TETRA10	29093	59733	8.7	743.24	875.45	1358	2180.3
CATIA	TETRA10	128551	222586	26.1	741.58	873.6	1356.3	2178.3

Table 5.3 Analytical natural frequency for blade M2

Frequency mode1 Hz	**Frequency mode2 Hz**	**Frequency mode3 Hz**	**Frequency mode4 Hz**
700.4993	835.7276	1328.565	2277.203

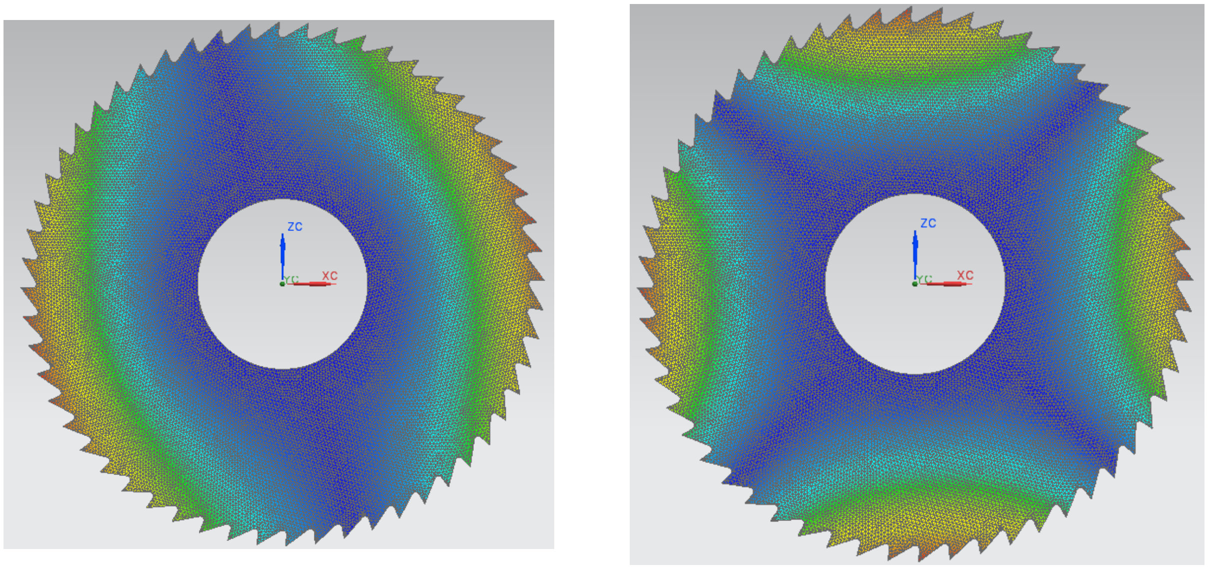

(a) First mode (0,1) (b) Second mode (0,2)

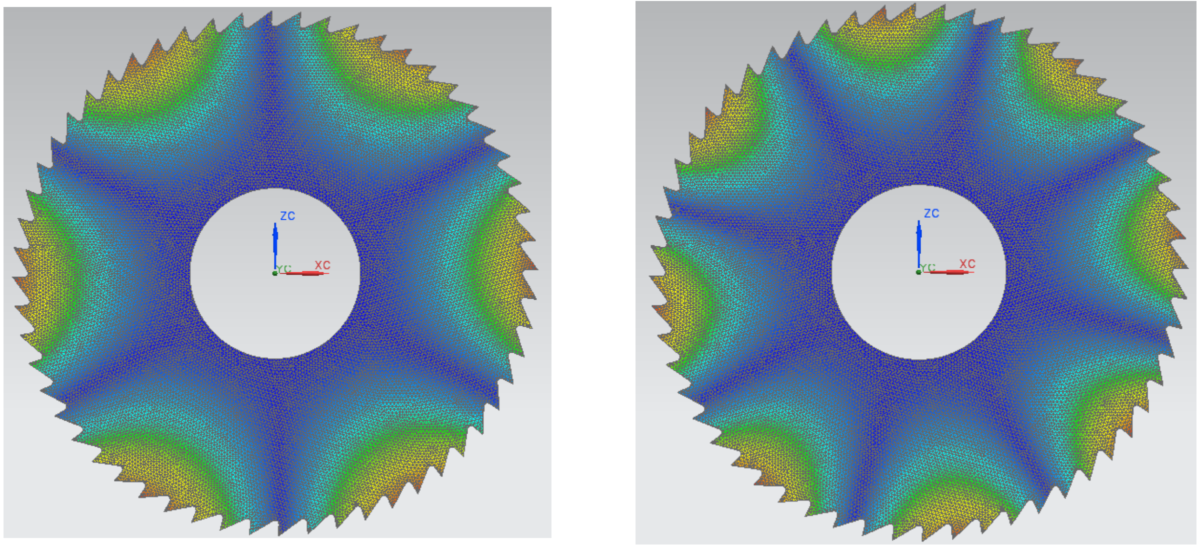

(c) Third mode (0,3) (d) Fourth mode (0,4)

Figure 5.3 – First four mode shapes for blade M2

The same blade geometry, bore hole for clamping constraint, and solver as the ones used for the above cases are used to further identify the effect of annular and radial slots on the natural frequency of the blade. The different slots geometries that are made on the circular saw blade for this analysis are shown in Figure 5.4. Table 5.4 shows the natural frequencies that resulted from the analysis of the different cases where annular and/or radial slots were made on the blade. It should be noted there that increased natural frequency is desired so that the vibration and noise during the cutting process are reduced.

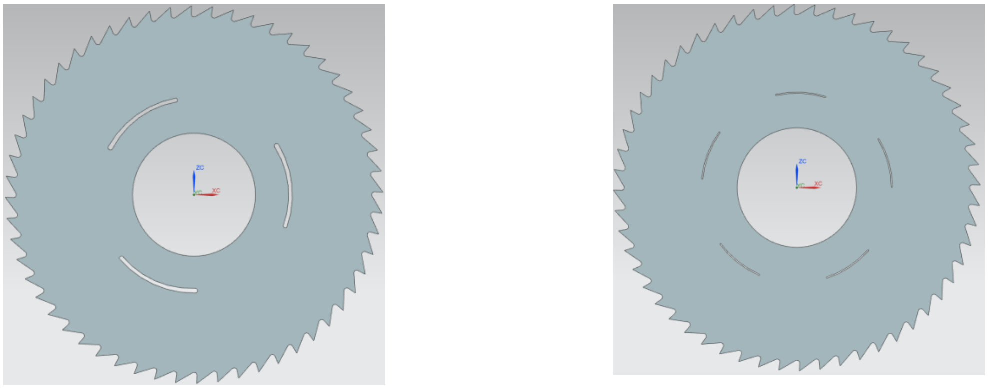

(a) Blade with three annular slots (b) Blade with five annular slots

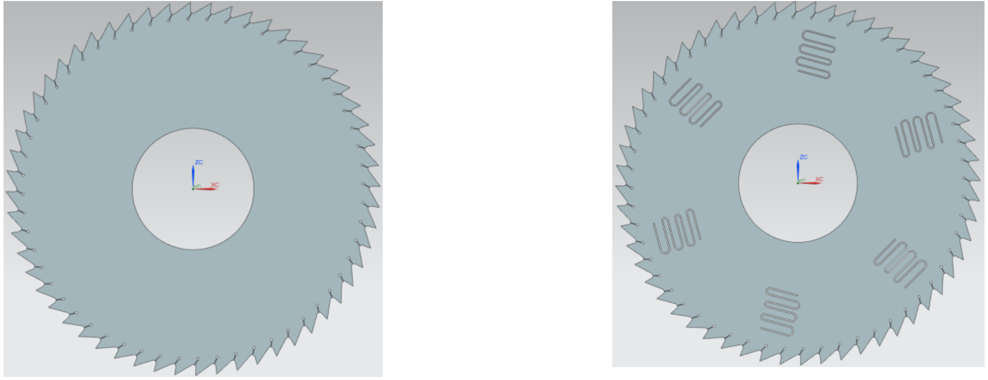

(c) Blade with radial slots (d) Blade with annular and radial slots

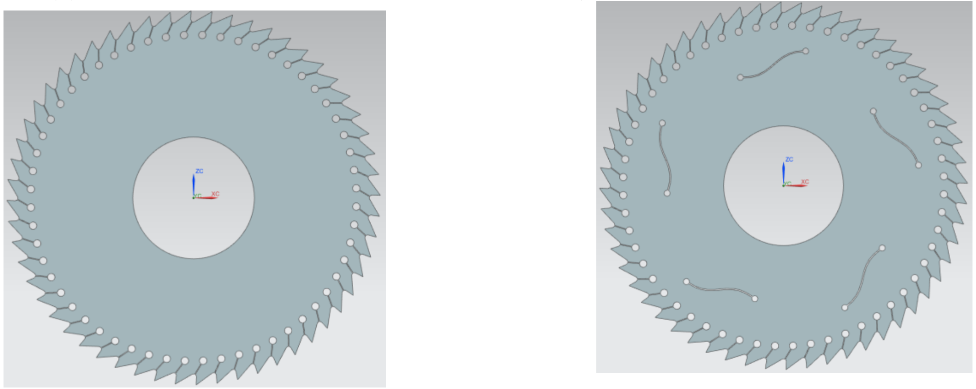

(e) Blade with larger radial slots (f) Blade with annular and radial slots

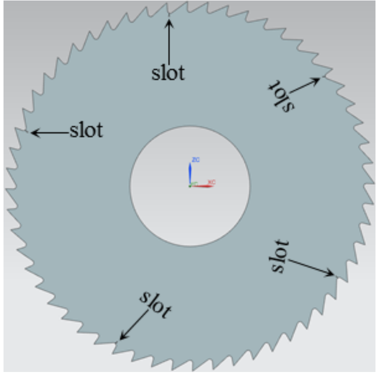

(g) Blade with five radial slots

Figure 5.4 – Different slots on the circular saw blade

For the common blade used by RGL, having blades with annular slots (Cases *a* and *b*) can reduce the natural frequency of the blade especially for the first three modes described in the previous section. Cases *d* and *f* include both annular and radial slots which have resulted in a decrease in the natural frequency for all modes. Even though radial slots have not improved the natural frequencies for all modes, they have led to an increase in the first mode's natural frequency. The first mode is more important to consider, since the resonance in machining process can occur at this mode due to having the smallest natural frequency for all cases. Therefore, Case *e* which has the largest radial slot on each tooth is suggested to replace the current blade used by RGL and more investigation on the geometric feature such as the size of the radial slot can be considered.

Table 5.4 Natural frequencies for blade having slots (Hz)

Circular blade case	**First mode**	**Second mode**	**Third mode**	**Fourth mode**
No slots	705.99	831.658	1291.19	2073.483
Case a	600.8	782.6	1223.4	2037.9
Case b	658.3	797.4	1270.1	2057.8
Case c	707.2	824.3	1246.1	2875.3
Case d	668.3	787.7	1136.1	1731.3
Case e	718.9	824.4	1182.2	2482.2
Case f	682.1	791.5	1141.4	1707.6
Case g	706	831.3	1289.8	2070.1

5.2 Static analysis

The circular saw blade that is currently used by RGL and the one shown under Case *e* in Figure 5.4 are selected to conduct the static analysis because they have the highest value of natural frequency (referring to Mode 1). The blade is kept fixed and static analysis is performed for the moment in the cutting process at which the maximum force is applied to the blade. The instance where the exerted force is highest is obtained from the force calculation presented in Section 4.3. The force values in both *x* and *y* directions apply to the teeth (12 teeth) that are in contact with the workpiece at this moment.

Figure 5.5 shows the deflection enlarged by a factor of 1 for the blades with and without radial slots obtained from the static analysis. It is important to note that in the figures shown, the *y* and *z* directions are different from the ones defined in Chapter 2 and this change is considered while applying the loads on the teeth.

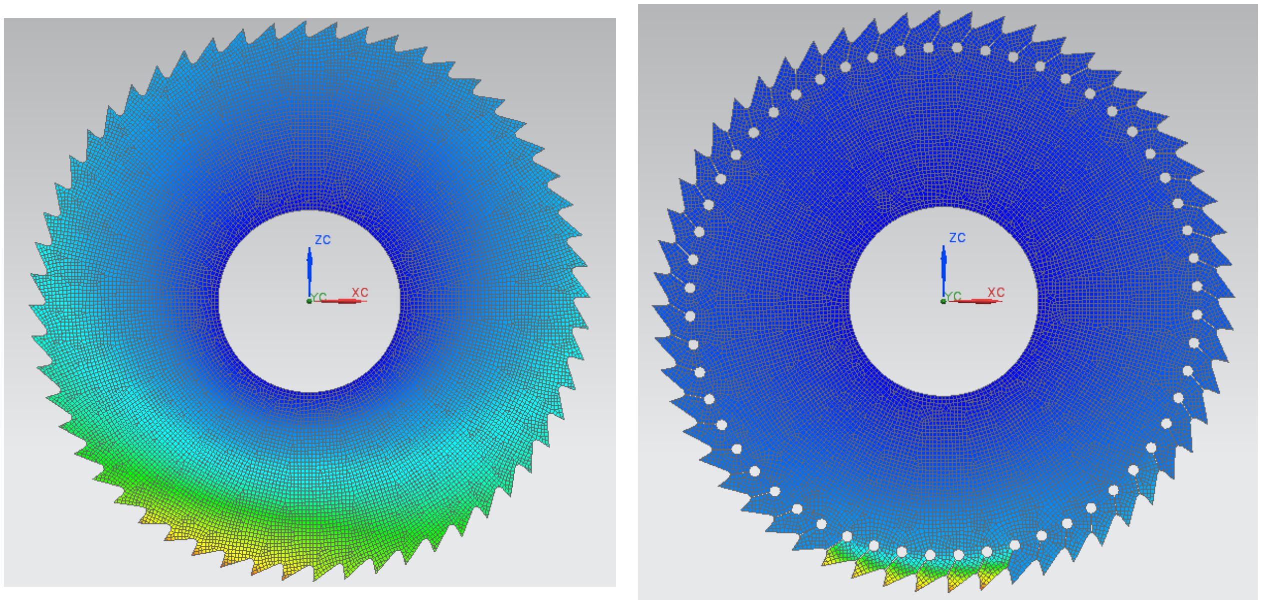

(a) Deformation in the original blade

(b) Deformation in the blade with radial slots

Figure 5.5 – Deflection of the blades in static analysis

Table 5.5 shows the maximum displacement the blade undergoes and that stress applied to it due to the highest cutting force during slotting process. Circular blades having radial slots have greater natural frequencies whereas blades without any radial slots experience less deformation and stress during cutting. This is very important as the cutting force has a direct impact on the tool life. It can be said that the initial blade design is preferred because it has a better tool life. The reason for blade deformation when having radial slots is the opening area between the teeth which, upon an applied force, makes is the blade material easier to break.

Table 5.5 Deformation results for blades with and without slots

	Maximum displacement (mm)				**Maximum Von-Mises stress (Mpa)**	
Blade	*magnitude*	*x*	*y*	*z*	*elemental*	*nodal*
Without slots	0.037	0.036	0.0002	0.011	393	490.9
With slots	0.107	0.104	0.00063	0.022	965.2	1399.6

Shape optimization

The aim of this section is to investigate the possibility of changing the blade geometry to reduce the blade teeth displacement due to the applied force. This can be achieved by using software packages such as NX and CATIA. A local sensor should first be created to measure the tooth deformation. It is preferred to place the sensor where the maximum displacement is experienced. This sensor can be parametrized and considered as an objective function for a minimization problem. Parameters for all features used to create the CAD model of the blade have to be created. These parameters in the current study are outer diameter of blade, bore diameter, tooth height, tooth pitch, gullet radius, rake angle, and relief angle. It should be noted that to design all teeth for the blade, pattern feature is the most common tool which uses one tooth to create all teeth along the outer diameter of the blade. Therefore, the formula for the number of teeth in the pattern feature should be used to automatically update the teeth number when other dimensions are changed. The equation to determine the number of teeth is given as:

$$\#of\ teeth = \frac{blade\ outer\ diameter * \pi}{tooth\ pitch} \tag{5.14}$$

There are several constraints that should be included in the problem. The blade has to have enough material to keep its stiffness; it can reach the plunge and cut the workpiece (for 0.362 in of pipe thickness and 0.3 in plunge). The upper limit for the outer diameter must be specified such that blades are separated by enough distance when they are mounted on the arbor. The gullet area has to have enough space to maintain the chips during cutting.

The upper limit for the relief angle is not defined because the rake angle is small and it can only be increased in the optimization. It is therefore important that as the rake angle is increased, the relief angle does not increase with it so as to maintain the material angle on the blade. The optimization process can thus be represented by:

$$objective: \min(deformation)$$

$$constraints: \begin{cases} outer\ diameter - bore\ diameter > 1.5in \\ 2in < outer\ diameter < 4in \\ 0.6in < bore\ diameter < 2in \\ 2deg < rake\ angle < 40deg \\ 3deg < relief\ angle < 30deg \\ 0.06in < tooth\ height < 0.15in \\ 0.14in < tooth\ pitch < 0.2in \\ 0.01in < gullet\ radius < 0.05in \end{cases} \quad (5.15)$$

Figure 5.6 shows the optimized geometry of the blade. Table 5.6 shows the dimensions for original and optimized blade.

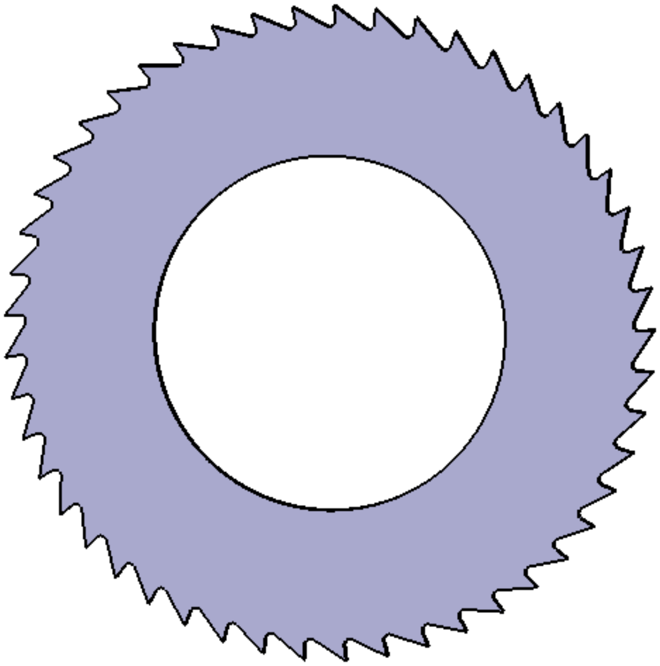

Figure 5.6 – New designed blade

Table 5.6 Updated geometry design

Parameter	**Original dimension**	**Optimal dimension**
Outer diameter (in)	3.07	2.93
Bore diameter (in)	1	1.57
Rake angle (degree)	2	5
Relief angle (degree)	30	28
Gullet radius (in)	0.023	0.027
Tooth pitch (in)	0.172	0.184
Tooth height (in)	0.082	0.073
Number of teeth	56	50

Based on the new blade design while keeping all other cutting parameters and material properties constant, the number of teeth that are in touch with the workpiece is different. The maximum number of teeth during slotting was calculated as 11 from the analytical models' solution. Therefore, both force in x and y directions should be excluded for one tooth as constraint in the static analysis. Figure 5.7 shows the deflection for the optimized blades without radial slots obtained from the static analysis. The deflection shown in the figure is enlarged by a factor of 10 for the purpose of clarity.

Table 5.7 shows the deformation results from static analysis. It can be inferred that the blade with optimal geometry has a better tool life since its displacement is smaller than the original shape especially in x and z directions.

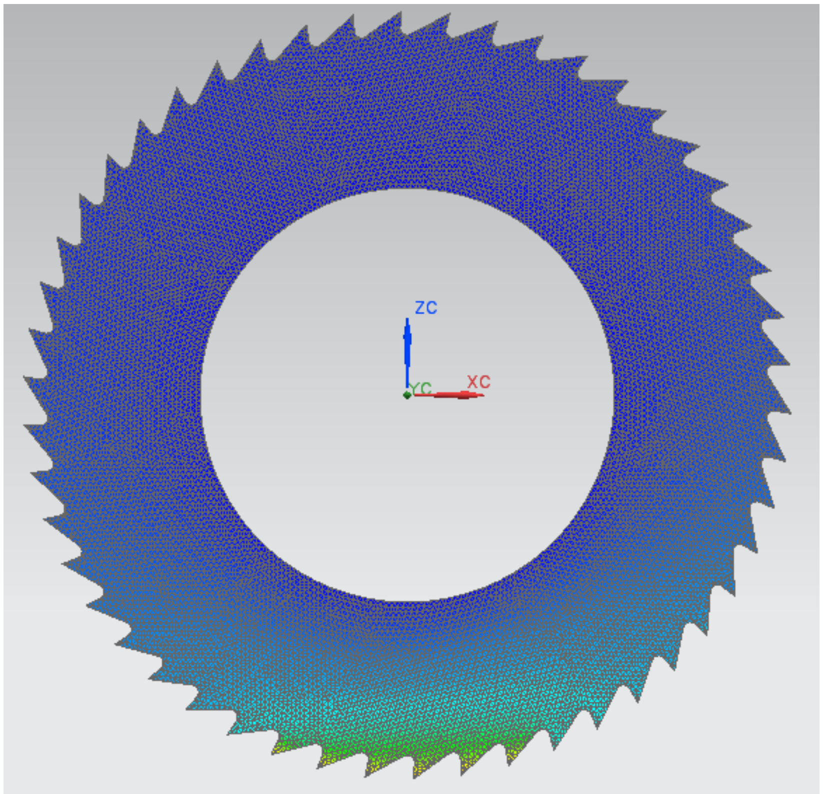

Figure 5.7 – Static analysis for the modified blade

Table 5.7 Deformation results for initial and modified blades without slots

	Maximum displacement (mm)				**Maximum Von-Mises stress (Mpa)**	
Blade	*magnitude*	*x*	*y*	*z*	*elemental*	*nodal*
Initial	0.037	0.036	0.0002	0.011	393	490.9
Modified	0.0264	0.0264	0.0002	0.006	488.8	629.4

Figure 5.8 shows the sensitivity analysis for the performed optimization process. It can be seen from Figure 5.8 (a) that the relief angle does not have significant changes during the course of optimization but decreased by 2 degrees for the lowest displacement. On the other hand, the rake angle has fluctuated during the iteration and its value is increased for the lowest deformation. Bore diameter has had more change as compared to the outer diameter of the blade as shown in Figure 5.8 (b). Increased inner hole of the blade leads to better results; however, since this parameter is directly related to the size of the arbor, it may require further considerations before reaching at a conclusion. The values of tooth height and gullet radius have differed during

iterations as given in Figure 5.8 (c). The tooth pitch remained constant for this optimization while the height and gullet had higher values for the lowest displacement.

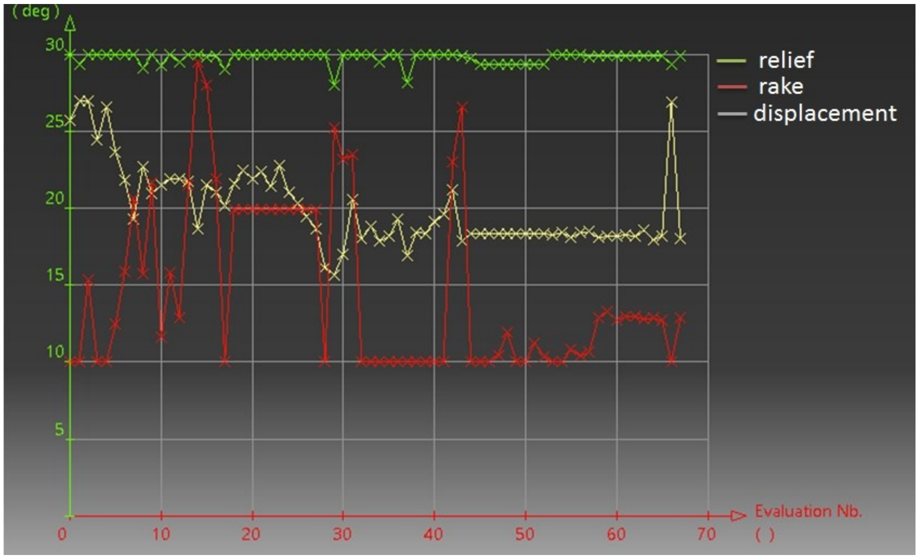

(a)

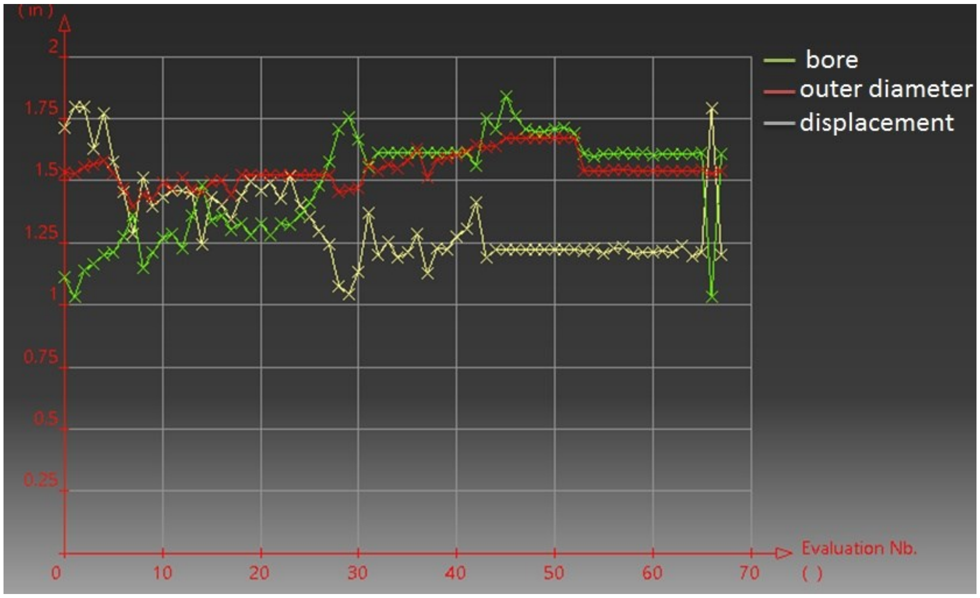

(b)

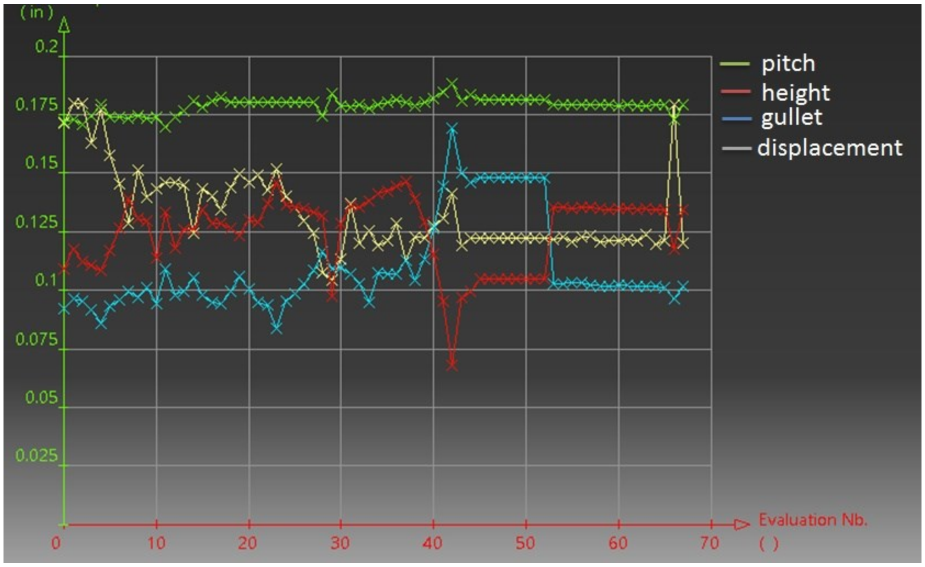

(c)

Figure 5.8 – Sensitivity analysis for (a) rake and relief angles (b) blade outer radius and bore diameter (c) tooth pitch, tooth height and gullet radius

A separate optimization is conducted for a circular blade with radial slots given under Case *e* in Figure 5.4. All dimensions are the same as the initial design with radial length, width, and radius of 0.05 in, 0.002 in, and 0.02 in, respectively. Figure 5.9 and Table 5.8 show the specifications of the updated design of the blade that has radial slots after optimization.

A similar trend is seen in the sensitivity analyses plots for blades with and without slots. In addition, Figure 5.10 shows that slot width and radius have fluctuated during iterations and decreased for the lowest displacement. However, slot length has increased for blade deformation improvement.

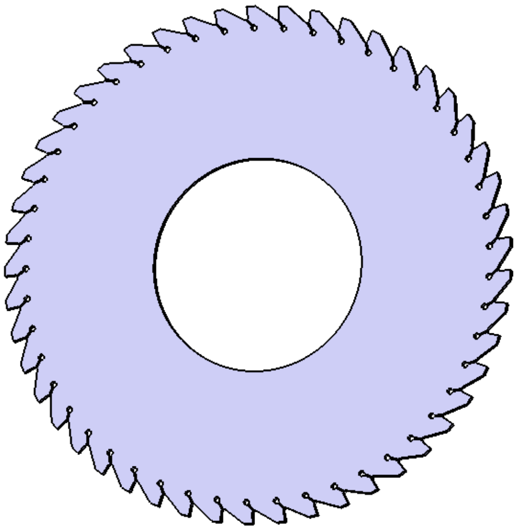

Figure 5.9 – New designed blade having radial slots

Table 5.8 Updated geometry design for blade having radial slots

Parameter	**Original dimension**	**Optimal dimension**
Outer diameter (in)	3.07	3.616
Bore diameter (in)	1	1.486
Rake angle (degree)	2	4
Relief angle (degree)	30	30
Gullet radius (in)	0.023	0.018
Tooth pitch (in)	0.172	0.167
Tooth height (in)	0.082	0.077
Number of teeth	56	67
Radial length (in)	0.05	0.075
Radial width (in)	0.002	0.001
Radial radius (in)	0.02	0.016

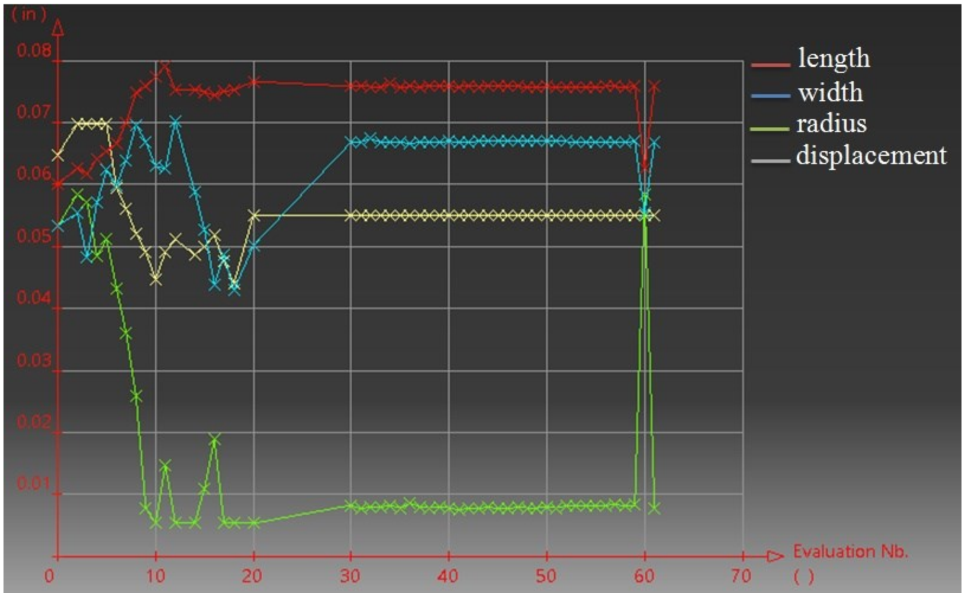

Figure 5.10 – Sensitivity analysis for radial slot geometry

The maximum number of teeth of the modified blade having radial slots as that are in contact with workpiece during cutting process is calculated to be 14 by solving the analytical models. Both forces in x and y directions are added for two teeth as constraint in the static analysis. Figure 5.11 shows the deflection for the optimized blades with radial slots obtained from the static analysis.

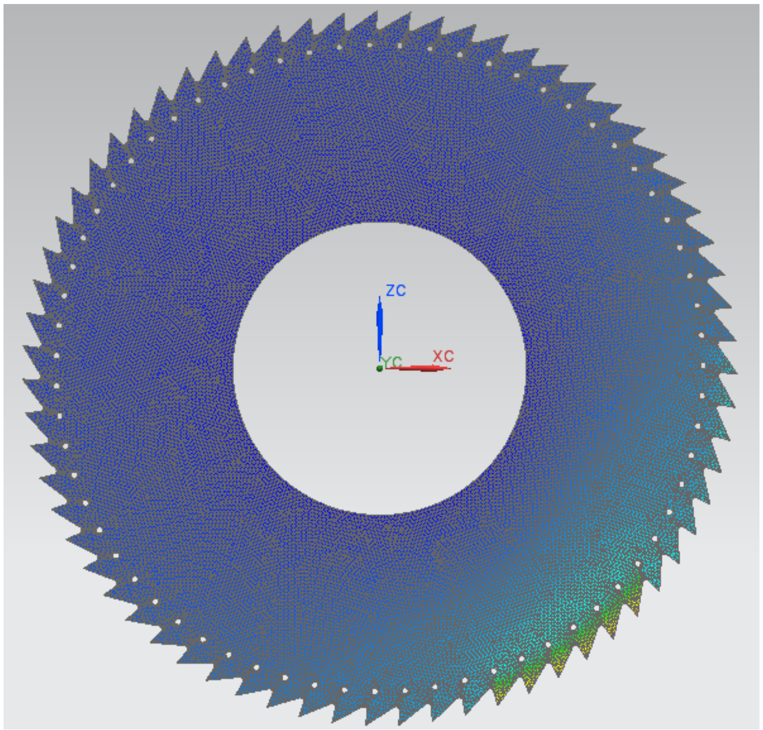

Figure 5.11 – Static analysis for the modified blade with radial slots

Table 5.9 shows the deformation results for the modified blade including slots from static analysis. Here again, a better tool life can be expected from the optimized blade since its displacement is smaller than the original shape especially in *x* and *z* directions.

Table 5.9 Deformation results for initial and modified blades with radial slots

	Maximum displacement (mm)				**Maximum Von-Mises stress (Mpa)**	
Blade	*magnitude*	*x*	*y*	*z*	*elemental*	*nodal*
Original	0.107	0.104	0.00063	0.022	965.2	1399.6
Modified	0.057	0.0052	0.000464	0.03	1034.2	1427.3

Comparing original and the optimized blades

The optimization results showed improved deformations for both circular saw blades with and without radial slots. It implies better tool life of the blades with optimized shape and dimensions can be expected for both cases. Further comparison between the two optimal shapes of blades shows that the blade without radial slots has better tool life since its teeth deformation is less.

The natural frequency for the blade modified by the shape optimization in discussed in the previous section is measured in NX. The element type highlighted in Table 5.2 that has been used for the original geometry remained the same in this analysis of the optimized shape. The natural frequencies of a rotating circular blade at different spindle speeds can be calculated using (5.11) and (5.12). Therefore, it is possible to check whether or not the stiffness and critical rotational speed of the blade have improved.

Table 5.10 shows the natural frequencies of both original blade and optimized one. It is find out that the new design of blade not only has smaller deformation, but also its natural frequency has increased which decrease the possibility of resonance.

Table 5.10 natural frequency for M2 blade and optimized blade (Hz)

Blade	**First mode**	**Second mode**	**Third mode**	**Fourth mode**
Original shape	705.99	831.658	1291.19	2073.489
Modified shape	1808.06	1996.18	2356.27	2999.7

Figure 5.12 shows the first four mode shape obtained from FE simulations for the modified blade.

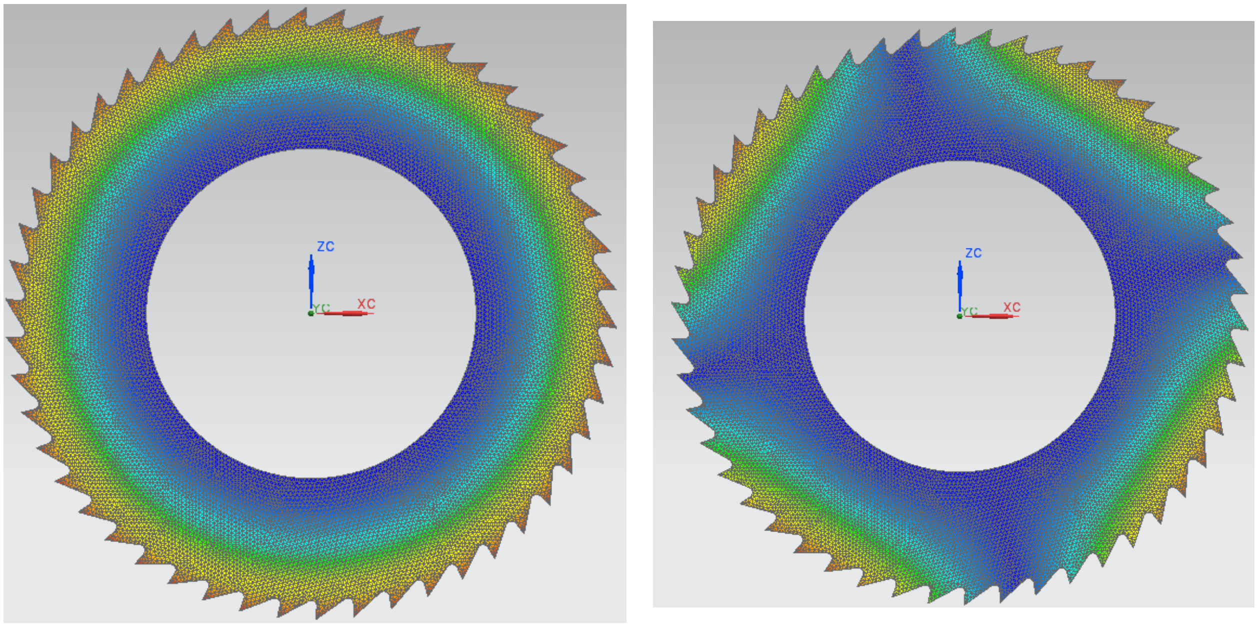

(a) 0.1

(b) 0.2

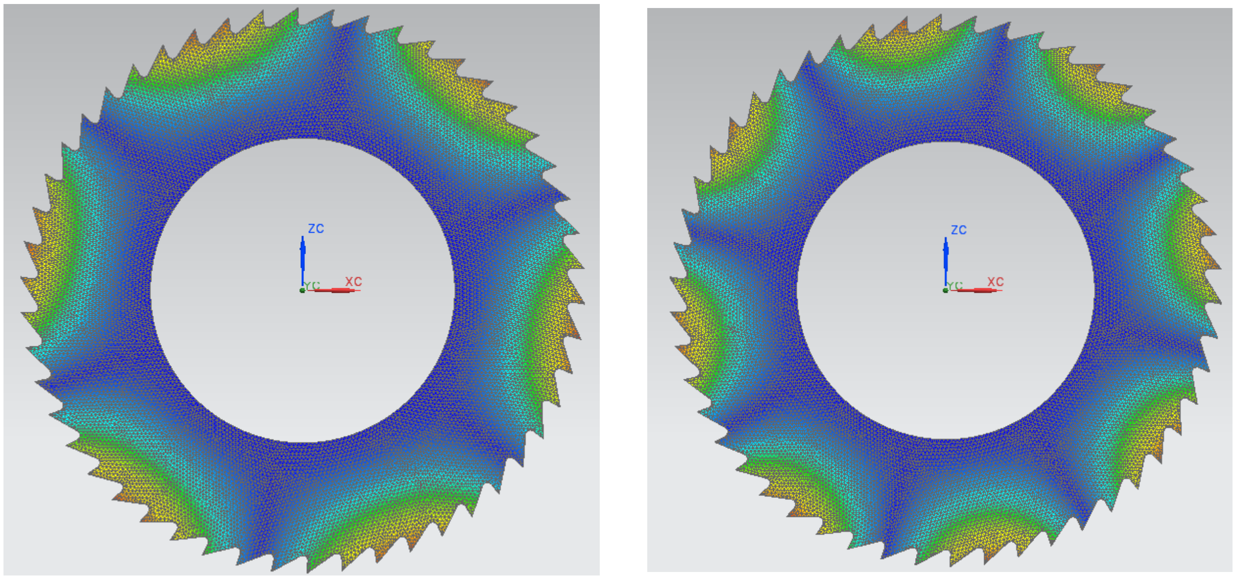

(c) 0.3 (d) 0.4

Figure 5.12 – Mode shapes for the optimized blade at different mode shapes

Table 5.11 shows the critical, optimal and permissible rotational speed for blade M2 and its optimized shape. The improvement in the rotational speed of the blade has also achieved from shape optimization as higher spindle speeds can used for the new designed blade. However, the blade rotational speed may not be a significant issue because the rpm are used by the multi-spindle slotting machine is usually much lower than the values mentioned in Table 5.11.

Table 5.11 Rotational speeds for both original and new designed blade

Blade	**Critical speed (rpm)**			**Optimal speed (rpm)**			**Permissible speed (rpm)**		
	(0.2)	*(0.3)*	*(0.4)*	*(0.2)*	*(0.3)*	*(0.4)*	*(0.2)*	*(0.3)*	*(0.4)*
Original	38846.6	34785.6	39538.1	23307.9	20871.3	23722.8	33019.6	29644.2	33632.8
Modified	93279.4	63482.8	57209.7	55967.6	38089.6	34325.8	79287.4	53960.3	48628.2

6. CONCLUSION AND RECOMMENDATIONS

6.1 Conclusion

A multi spindle slotting machine built by RGL was used as the case here to study the effect of different processing conditions on the efficiency of the machining process. The effects of the cutting speed and feed rate on the tool life and production rate were identified. The geometry and material properties of circular saw blades used by RGL were manipulated to conduct an analytical and numerical analysis of the cutting process.

In the methodology employed for this research, analysis of forces involved in the cutting process was the major component. An algorithm designed to solve an analytical model specifically developed for a multi-spindle slotting machine that uses circular saw blades was used for the force analysis. The model development has accounted for the different time steps caused by the difference in feed rates at progressive stages in the process of the slotting through the pipe. Results from these analyses were later applied to study the chatter frequency during the machining process, and conduct optimization on the geometry of the blade.

The effect of rake angle and relief angle was studied. Increasing rake angle resulted in decrease in the required force. As the rake angle increases, the relief angle should be decreased to preserve the material angle of the tooth. It was concluded that having higher rake angle leads to better tool life. However, the consequential adjustment that has to be made on the relief angle shall be considered accordingly.

The analyses also covered different spindle speeds. It was concluded that increase in the spindle speed resulted in lower required force. The selection of rpm for this specific machine can be guided by the stability lobe diagram given in Figure 4.17. For a similar pipe and blade materials used, this diagram can be referred to identify the stability condition when processing parameters are planned to change. The possibilities of tool breakage at different rpms that could be expected based on results of this study, match the small-scale in house trend recorded by RGL.

Cases where slotting machine included sharp and/or dull blades were investigated by combining analytical models and simulations for the respective scenarios. As expected, dull blades caused significantly higher force requirements and blade displacement. As this condition leads to significant increase in the cost incurred by the operation, monitoring of the blades to keep sharp blades on the machine at all times needs to be implemented. The accuracy of the system that is to be used to monitor shall be given enough emphasis to make sure that dull blades do not reduce the efficiency of the process and/or quality of the product.

The different pipe and blade materials that are commonly used by RGL were used to come up with tool-pipe combinations that formed cases that were separately studied. From the results it was concluded that HSS M2 blade is best suited to slot K55 pipe while L80 pipe can be slotted with HSS M35 blade for better manufacturing.

The shear angle values that resulted from FE simulations came in good agreement with results from analytical calculation. Therefore, the satisfactory application of the developed analytical model to predict the slotting process' parameters was strongly indicated. Furthermore, this research demonstrated that the methodologies presented can be applied for any future case to form a basis in the tool selection for a given pipe material.

Optimization was conducted to identify new blade geometries for improved performance. By making use of the results from the force analysis different cases for blade geometry with and without added features were studied to determine the optimal blade geometry and dimensions. Table 5.6 and Table 5.8 give the specifications for the optimal blade geometry identified. It was concluded that, if changing the blade geometry for better tool life is considered by RGL, the specifications given in Table 5.6 shall be followed

6.2 Recommendations

Based on what is studied in this research and the above conclusion given, the following points are forwarded as recommended considerations for future work in the same or related topic:

- The phenomenon of friction during the cutting process can be further investigated in detail so that the validity of the friction coefficient used in this study is confirmed.
- The issue of thermal effects during the cutting process shall be more investigated as it may be expected that the effect of generated heat is significant. Experimental techniques that apply online and non-intrusive measurements such as optical methods are suggested to be considered.

- The algorithm presented in this research can be accordingly modified to be able to have an in-depth analysis of a specific manufacturing problem at hand
- There can be significant change in the cost of operation and material that may result from what is suggested by the optimization results given in Chapter 5. Further study can be conducted to determine the economic feasibility of using the new blade or arbor dimensions.
- Future investigations especially on the effect of vibration are suggested to include enough experimental work in parallel with numerical or analytical studies. This will primarily help in the validation of results but it will also give enough flexibility to experiment and simulate as many conditions as are actual and relevant.
- Different software packages had to be used to solve the analytical models and, mainly, to conduct FE simulations throughout this research. From the entire experience, the potential to increase the efficiency by applying a computer system that integrates the functionality of the various software applications used was clearly visible. Future researches dedicated to work on multidisciplinary modeling and software development can take on the task of making an application that presents the user with functions of required packages.

REFERENCES

[1] C. Holly, M. Mader, S. Soni, and J. Toor, “Alberta Energy, Oil Sands Production Profile: 2004-2014,” 2016.

[2] R. M. Butler, G. S. McNab, and H. Y. Lo, “Theoretical Studies on the Gravity Drainage of Heavy Oil During in-Situ Steam Heating.,” *Can. J. Chem. Eng.*, vol. 59, no. 4, pp. 455–460, 1981.

[3] R. M. Butler, “Steam-Assisted Gravity Drainage: Concept, Development , Performance and Future,” *J. Can. Pet. Technol.*, 1984.

[4] D. Matanovic, M. Cikes, and B. Moslavac, *Sand Control in Well Construction and Operation*. Springer, 2012.

[5] V. ENERGY, “SAGD.” [Online]. Available: http://voltaenergy.ca/dev/introduction/sagd/.

[6] D. B. Bennion, S. Gupta, S. Gittins, and D. Hollies, “Protocols for slotted liner design for optimum SAGD operation,” *J. Can. Pet. Technol.*, vol. 48, no. 11, pp. 21–26, 2009.

[7] J. Xie, S. W. Jones, C. M. Matthews, B. T. Wagg, P. Parker, and R. Ducharme, “Slotted liner design for SAGD wells,” *World Oil*, vol. 228, no. 6, pp. 67–75, 2007.

[8] W. Renpu, *Advanced Well Completion Engineering*. ELSEVIER, 2011.

[9] A. Kumar, A. Srivastava, and R. Kumar, “Design Optimization of Slotted Liner Completions in Horizontal Wells of Mumbai High Field,” *Proc. SPE Asia Pacific Oil Gas Conf. Exhib.*, 2010.

[10] T. Childs, K. Maekawa, T. Obikawa, and Y. Yamane, *Metal Machining Theory and Applications*, 1st ed. London: Arnold, 2000.

[11] H. El-Hofy, *Fundamentals of machining processes: conventional and nonconventional processes*, 2nd ed. Boca Raton: CRC Press, Taylor & Francis Group, 2014.

[12] Y. Altintas, *Manufacturing automation: metal cutting mechanics, machine tool vibrations, and CNC design*, 2nd ed. Cambridge: Cambridge University Press, 2012.

[13] N. Balihodzic, “A Numerical Investigation of Orthogonal Machining,” University of New Brunswick, 2002.

[14] C. KILIÇASLAN, “MODELLING AND SIMULATION OF METAL CUTTING BY FINITE ELEMENT METHOD,” İzmir Institute of Technology, 2009.

[15] A. P. Markopoulos, *Finite Element Method in Machining Processes*, 1st ed. London: Springer-Verlag, 2013.

[16] A. Behrens and B. Westhoff, “Finite Element Modeling of High Speed Machining Processes,” 1999.

[17] A. Behrens and B. Westhoff, “Finite Element Modeling of high speed machining

processes," *PTW TU Darmstadt*, p. 6, 1999.

[18] H. K. (Hans K. Tönshoff, *Basics of Cutting and Abrasive Processes*. Berlin: Springer, 2013.

[19] E. M. Trent and P. K. Wright, *Metal Cutting*, 4th ed. Butterworth-Heinemann, 2000.

[20] G. W. Rowe and P. T. Spick, "A New Approach to Determination of the Shear-Plane in Machining," *ASME J. Eng. Ind.*, vol. 89, pp. 530–538, 1967.

[21] M. E. Merchant, "Mechanics of the metal cutting process. II. Plasticity conditions in orthogonal cutting," *J. Appl. Phys.*, vol. 16, no. 6, pp. 318–324, 1945.

[22] P. L. B. Oxley, "Mechanics of Metal Cutting," *Int. J. Mach. Tool Des. Res.*, vol. 1, no. 2, 1961.

[23] J. A. Stori, "Machining operation planning based on process simulation and the mechanics of milling," UNIVERSITY OF CALIFORNIA, BERKELEY, 1998.

[24] I. A. TIME, "Resistance of metals and wood to cutting (in Russian)," in *Dermacow Press House*, 1870.

[25] H. Tresca, "Mémoires sur le Rabotage des Métaux. Bulletin de la Société d," in *Encouragement pour l' Industrie Nationale*, 1873, pp. 585–607.

[26] K. Zvorykin, "On the force and energy necessary to separate the chip from the workpiece (in Russian)," in *Vetnik Promyslennostie*, 1896.

[27] A. Mallock, "The action of cutting tools," in *Proc Roy Soc Lond*, 1881.

[28] V. Piispanen, "Theory of formation of metal chips," *J. Appl. Phys.*, vol. 19, no. 10, pp. 876–881, 1948.

[29] H. Ernst and M. E. Merchant, "Chip Formation, Friction and High Quality Machined Surfaces, in Surface Treatment of Metals," *Am. Soc. Met.*, vol. 29, p. 299, 1941.

[30] M. E. Merchant, "Mechanics of the metal cutting process. I. Orthogonal cutting and a type 2 chip," *J. Appl. Phys.*, vol. 16, no. 5, pp. 267–275, 1945.

[31] E. H. Lee and B. W. Shaffer, *The Theory of Plasticity Applied to a Problem of Machining*. Division of Applied Mathematics, 1949.

[32] S. Kobayashi and E. G. Thomson, "Metal-Cutting Analysis — II," *J. ofEngineeringfor Ind.*, vol. 84, no. Transactions ofASME, pp. 71–80, 1962.

[33] E. J. A. Armarego; and R. H. Brown, *The machining of metals*. Englewood Cliffs, 1969.

[34] J. Krystof, *Berichte uber Betriebswissenschaftliche Arbeiten*, 12th ed. VDI Verlag, 1939.

[35] M. C. Shaw, *Metal Cutting Principles*. Clarendon Press, 1984.

[36] S. Sikder, "Analytical Model for Force Prediction wHEN mACHINING mETAL

cUTTING mATRIX cOMPOSITES," University of Ontario Institute of Technology, 2010.

[37] T. L. Eldho and Y. M. Desai, *Finite Element Method with Applications in Engineering*. Pearson India, 2011.

[38] T. K. Kershah, "Prediction of cutting coefficients during orthogonal metal cutting process using FEA approach," McMaster University, 2013.

[39] K. Iwata, K. Osakada, and Y. Terasaka, "Process Modeling of Orthogonal Cutting by the Rigid-Plastic Finite Element Method," *J. Eng. Mater. Technol.*, vol. 106, no. 2, pp. 132–138, 1984.

[40] K. Komvopoulos and S. A. Erpenbeck, "Finite Element Modeling of Orthogonal Metal Cutting," *J. Eng. Ind.*, vol. 113, no. August, pp. 253–267, 1991.

[41] A. J. Shih, "Finite Element Simulation of Orthogonal Metal Cutting," *J. Eng. Ind.*, vol. 117, no. February, pp. 84–93, 1995.

[42] S. Guoqin, D. Xiaomin, and C. Shet, "A finite element study of the effect of friction in orthogonal metal cutting," *Finite Elem. Anal. Des.*, vol. 38, no. 9, pp. 863–883, 2002.

[43] T. Schermann, J. Marsolek, C. Schmidt, and J. Fleischer, "Aspects of the Simulation of a Cutting Process with ABAQUS/Explicit Including the Interaction between the Cutting Process and the Dynamic Behavior of the Machine Tool," *9th CIRP Int. Work. Model. Mach. Oper. Bled, Slowenia*, vol. 11, p. 12, 2006.

[44] T. Marusich and M. Ortiz, "Modeling and simulation of high-speed machining," *International Journal for Numerical Methods in Engineering*, vol. 38. pp. 3675–3694, 1995.

[45] G. Warnecke and J.-D. Oh, "A new Thermo-viscoplastic Material Model for Finite-Element-Analysis of the Chip Formation Process," *CIRP Ann. - Manuf. Technol.*, vol. 51, no. 1, pp. 79–82, 2002.

[46] Y. C. Yen, A. Jain, and T. Altan, "A finite element analysis of orthogonal machining using different tool edge geometries," *J. Mater. Process. Technol.*, vol. 146, no. 1, pp. 72–81, 2004.

[47] Y. C. Yen, J. Söhner, B. Lilly, and T. Altan, "Estimation of tool wear in orthogonal cutting using the finite element analysis," *J. Mater. Process. Technol.*, vol. 146, no. 1, pp. 82–91, 2004.

[48] X. L. K. Li Goa, J.W. Sutherland, "Finite element simulation of the orthogonal metal cutting process for qualitative understanding of the effects of crater wear on the chip formation process.," *J. Mater. Process. Technol.*, vol. 127, pp. 309–324, 2002.

[49] J. T. Carroll and J. S. Strenkowski, "Finite element models of orthogonal cutting with application to single point diamond turning," *Int. J. Mech. Sci.*, vol. 30, no. 12, pp. 899–920, 1988.

[50] J.-S. Wu, O. W. Dillon Jr., and W.-Y. Lu, “Thermo-viscoplastic modeling of machining process using a mixed finite element method,” vol. 39, no. November 1996, pp. 113–128, 1992.

[51] H. V. Martinez and M. Hankele, “Simulation of the circular sawing process,” 2015.

[52] B. Wang and Z. Liu, “Investigations on the chip formation mechanism and shear localization sensitivity of high-speed machining Ti6Al4V,” *Int. J. Adv. Manuf. Technol.*, vol. 75, no. 5–8, pp. 1065–1076, 2014.

[53] T.T.Öpöz and X. Chen, “FINITE ELEMENT SIMULATION OF CHIP FORMATION,” in *School of Computing and Engineering Researchers' Conference, University of Huddersfield*, 2010.

[54] B. Zhang and A. Bagchi, “Finite element simulation of chip formation and comparison with machining experiment,” *J. Eng. Ind.*, vol. 116, no. 3, pp. 289–297, 1994.

[55] J. M. Huang and J. T. Black, “An Evaluation of Chip Separation Criteria for the FEM Simulation of Machining,” *J. Manuf. Sci. Eng.*, vol. 118, no. 4, pp. 545–545, 1996.

[56] V. Madhavan, S. Chandrasekar, and T. N. Farris, “Machining as a Wedge Indentation,” *J. Appl. Mech.*, vol. 67, no. 1, p. 128, 2000.

[57] I. Escamilla, O. Zapata, B. Gonzalez, N. Gámez, and M. Guerrero, “3D Finite Element Simulation of the Milling Process of a TI 6AL 4V Alloy,” *2010 SIMULA Cust. Conf.*, pp. 1–10, 2010.

[58] M. Agmell, A. Ahadi, and J. E. Ståhl, “The link between plasticity parameters and process parameters in orthogonal cutting,” *Procedia CIRP*, vol. 8, pp. 224–229, 2013.

[59] X. Bin Liu, X. Bin Wang, C. N. Li, and S. P. Deng, “Finite Element Simulation of the Orthogonal Cutting Based on Abaqus,” *Adv. Mater. Res.*, vol. 821–822, pp. 1410–1413, 2013.

[60] N. Sawarkar and G. Boob, “Finite Element based Simulation of Orthogonal Cutting Process to Determine Residual Stress Induced,” *Int. J. Comput. Appl.*, pp. 33–38, 2014.

[61] Y. Zhang, J. C. Outeiro, and T. Mabrouki, “On the selection of Johnson-Cook constitutive model parameters for Ti-6Al-4V using three types of numerical models of orthogonal cutting,” *Procedia CIRP*, vol. 31, pp. 112–117, 2015.

[62] J. S. Strenkowski and J. T. Carroll, “A Finite Element Model of Orthogonal Metal Cutting,” *J. Eng. Ind.*, vol. 107, no. 4, p. 349, 1985.

[63] J. Q. Xie, A. E. Bayoumi, and H. M. Zbib, “FEA modeling and simulation of shear localized chip formation in metal cutting,” *Int. J. Mach. Tools Manuf.*, vol. 38, no. 9, pp. 1067–1087, 1998.

[64] Zorev NN, “Inter-relationship between shear processes occurring along tool face and shear plane in metal cutting,” *Proc. Int. Res. Prod. Eng. Conf. ASME, New York*, pp. 42–49, 1963.

[65] E. Usui and T. Shirakashi, “Mechanics of Machining - from ‘Descriptive’ to ‘Predictive’ Theory,” *ASME Publ.*, vol. 7, pp. 13–35, 1982.

[66] Q. Zheng, R. Yang, Y. Hu, and X. Yue, “A study for micro cutting process of Guide abrasive wear based on ABAQUS,” *2014 IEEE Int. Conf. Mechatronics Autom. IEEE ICMA 2014*, pp. 834–838, 2014.

[67] A. Shrot and M. Bäker, “Is It Possible To Identify Johnson-Cook Law Parameters From Machining Simulations ?,” *Int J Mater Form*, vol. 3, pp. 443–446, 2010.

[68] M. Sarwar and P. J. Thompson, “Simulation of the cutting action of a single hacksaw blade tooth,” *Prod. Eng.*, no. June, pp. 195–198, 1974.

[69] A. J. Shih, “FINITE ELEMENT ANALYSIS OF THE RAKE ANGLE EFFECTS IN ORTHOGONAL METAL CUTTING,” *Int. J. Mech. Sci.*, vol. 38, no. 1, p. 17, 1996.

[70] C. K. Ng, S. N. Melkote, M. Rahman, and A. Senthil Kumar, “Experimental study of micro- and nano-scale cutting of aluminum 7075-T6,” *Int. J. Mach. Tools Manuf.*, vol. 46, no. 9, pp. 929–936, 2006.

[71] X. Liu, R. E. DeVor, S. G. Kapoor, and K. F. Ehmann, “The Mechanics of Machining at the Microscale: Assessment of the Current State of the Science,” *J. Manuf. Sci. Eng.*, vol. 126, no. 4, p. 666, 2004.

[72] L. Wan, D. Wang, and Y. Gao, “Investigations on the Effects of Different Tool Edge Geometries in the Finite Element Simulation of Machining,” *J. Mech. Eng.*, vol. 61, no. 3, pp. 157–166, 2015.

[73] A. Pal, S. K. Choudhury, and S. Chinchanikar, “Machinability Assessment through Experimental Investigation during Hard and Soft Turning of Hardened Steel,” *Procedia Mater. Sci.*, vol. 6, no. Icmpc, pp. 80–91, 2014.

[74] K. S. S. Tony L. Schmitz, *Mechanical Vibration: modeling and measurement*. Springer, 2012.

[75] S. M. Young, “Dynamics of Low Immersion Milling by,” University of Maryland, 2008.

[76] R. Sridhar, R. E. Hohn, and G. W. Long, “A General Formulation of the Milling Process Equation - Contrivution to Machine Tool Chatter Research - 5,” *ASME J. Eng. Ind.*, vol. 90, pp. 317–324, 1968.

[77] B. I. A. Sutherland, B. Sc, C. Andrew, D. Ph, and M. E. Mech, “FORCED VIBRATION AND CHATTER IN HORIZONTAL MILLING : AN INVESTIGATION USING A STRUCTURAL MODEL,” *Proc. Inst. Mech. Eng.*, vol. 183, no. 21, pp. 395–416, 1968.

[78] Y. Altintas and I. Yellowley, “The identification of radial width and axial depth of cut in peripheral milling,” vol. 27, no. 3, pp. 367–381, 1987.

[79] M. D. Tsai, S. Takata, M. Inui, F. Kimura, and T. Sata, “Prediction of Chatter Vibration by Means of a Model-Based Cutting Simulation System,” *CIRP Ann. - Manuf. Technol.*, vol. 39, no. 1, pp. 447–450, 1990.

[80] J. Tlusty and F. Ismail, "Basic Non-Linearity in Machining Chatter," *CIRP Ann. - Manuf. Technol.*, vol. 30, no. 1, pp. 299–304, 1981.

[81] S. Smith and J. Tlusty, "An Overview of Modeling and Simulation of the Milling Process," *J. Eng. Ind.*, vol. 113, no. 2, pp. 169–175, 1991.

[82] B. E. Clancy and Y. C. Shin, "A comprehensive chatter prediction model for face turning operation including tool wear effect," *Int. J. Mach. Tools Manuf.*, vol. 42, no. 9, pp. 1035–1044, 2002.

[83] E. Solis, C. R. Peres, J. E. Jiménez, J. R. Alique, and J. C. Monje, "A new analytical-experimental method for the identification of stability lobes in high-speed milling," *Int. J. Mach. Tools Manuf.*, vol. 44, no. 15, pp. 1591–1597, 2004.

[84] X. Jin, Y. Sun, Q. Guo, and D. Guo, "3D stability lobe considering the helix angle effect in thin-wall milling," *Int. J. Adv. Manuf. Technol.*, vol. 82, no. 9–12, pp. 2123–2136, 2016.

[85] W. Wang, "Simulation of Force for Circular Saw Blades based on MATLAB," 2014.

[86] L. Pang, "Analytical Modeling and Simulation of Metal Cutting Forces for Engineering Alloys," University of Ontario Institute of Technology, 2012.

[87] T. L. Schmitz and K. S. Smith, *Machining dynamics: Frequency response to improved productivity*. 2009.

[88] A. G. Atkins, "Modelling metal cutting using modern ductile fracture mechanics: Quantitative explanations for some longstanding problems," *Int. J. Mech. Sci.*, vol. 45, no. 2, pp. 373–396, 2003.

[89] A. J. Shih, *Finite Element Simulation of Orthogonal Metal Cutting*, vol. 117, no. 1. 1995.

[90] G. R. Johnson and W. H. Cook, "Fracture characteristics of three metals subjected to various strains, strain rates, temperatures and pressures," *Eng. Fract. Mech.*, vol. 21, no. 1, pp. 31–48, 1985.

[91] A. Maftah, "FINITE ELEMENT SIMULATION OF ORTHOGONAL METAL CUTTING USING AN ALE APPROACH," UNIVERSITY OF NEW BRUNSWICK, 2008.

[92] B. Fermaniuk, "Sand Control in Steam Assisted Gravity Drainage (SAGD) Wellbores and Process of Slotted Liner Design and Manufacture," University of Calgary.

[93] F. Klocke, *Manufacturing Processes 1*. Aachen: Springer, 2011.

[94] A. Aramcharoen and P. T. Mativenga, "Size effect and tool geometry in micromilling of tool steel," *Precis. Eng.*, vol. 33, no. 4, pp. 402–407, 2009.

[95] A. Skoblar, N. Andjelic, and R. Zigulic, "DETERMINATION OF CRITICAL ROTATIONAL SPEED OF CIRCULAR SAWS FROM NATURAL FREQUENCIES OF ANNULAR PLATE WITH ANALOGOUS DIMENSIONS," *Int. J. Qual. Res.*, vol. 10,

no. 1, pp. 177–192, 2016.

[96] R. Singh, “Case history: The effect of radial slots on the noise of idling circular saws,” *Noise Control Eng. J.*, vol. 31, pp. 167–172, 1988.

[97] Y. M. Stakhiev, “Today and tomorrow circular sawblades: Russian version,” *Holz als Roh- und Werkst.*, vol. 58, no. 4, pp. 229–240, 2000.

[98] J. Svoreň, Ľ. Javorek, A. Droba, and D. Paulíny, “Comparison of Natural Frequencies Values of Circular Saw Blade Determined by Different Methods,” *Drv. Ind.*, vol. 66, no. 2, pp. 123–128, 2015.

[99] A. Kaczmarek, K. Orłowski, and L. Javorek, “The Effect of Circular Saw Blade Clamping Diameter on its Resonant Frequencies,” *Appl. Mech. Mater.*, vol. 838, no. June, pp. 18–28, 2016.

[100] A. Droba, Ľ. Javorek, J. Svoreň, and D. Paulíny, “New design of circular saw blade body and its influence on critical rotational speed,” *Drewno*, vol. 58, no. 194, pp. 147–157, 2015.

APPENDICES

Appendix A

```matlab
clear all
clc
set(gca,'Fontname','Timesnewroman','FontSize', 14)
%Input Parameters
     R = 3.07/2;                 % inch, blade outer radius
     H = R+0.2;                    % inch, intial distance from the circle centre to the work-piece
     vf2 = 3/60;                 % inch/s, feed rate
     vf3 = 2/60;                 % inch/s, feed rate
     vf4 = 4/60;                 % inch/s, feed rate
     vf1 = 90/60;                % inch/s, feed rate
     RPM = 255;                  % spindle speed
     omega = ((2*pi)/60)*RPM;               % rad/s, angular velocity, corresponding to RPM rotational speed
     N = 56;                     % number of total teeth
     Th = 0.362;                 % inch, thickness of the work-piece
     tau = 633*10^6 * 0.000145038;      % PSI, Mpa*145.0377=PSI, shearing stress of the work-piece
     W = 0.023;                  % inch, slot width
     L = 1.842;                  % inch, OD slot length
     alpha = 2*2*pi/360;         % rad, rake angle of the circular saw blade
     beta = 26.5*2*pi/360;         % rad, friction angle of interface between blade and work-piece
     precision = 0.1;              % precision used to divide time period into number of shares
     P = (R)-(sqrt(((R)^2)-(((L)/2)^2)));   % Plunge (in)
     vv = (2 * R * pi * RPM)/60;         %cutting speed (in/sec)
     vvi = vv * 0.0254;                  %cutting speed (m/sec)
     vvii = vvi * 1000;                  % cutting speed (mm/sec)
     phi1 = xlsread('D:\first review\pro\Force calculation\abaqus\stability\sarafinal (1).xlsx', 'Sheet2');  % Reading shear angle data
     phi = (phi1 * pi)/180;              % shear angle (degree)


     %     ************************     Calculation     of     key     time     points **************************************
     T = 2 * pi / omega;      % s, rotational period of the circular saw blade
     T_tooth = T / N;             % s, time per tooth, the time peoriod between two adjacent teeth
     theta_tooth = 2 * pi / N;       % rad, angle per tooth, the radial angle between two adjacent teeth
     t0 = (2*(H - R))/(vf1+vf2);
     theta0 = (ceil(t0 / T_tooth) - t0 / T_tooth) * theta_tooth;
     i = 1;
     while true
         y= ((i*precision)*(vf1+vf2)/2) - R+R * cos(theta0 - omega * (i*precision));
```

```
         if y > 0.00000
             index = i;
             y2 = (((i*precision)^2)*(vf1+vf2)-(vf1*(i*precision)*(precision)))/(2*(i-
1)*precision) - R+R * cos(theta0 - omega * ((i-1) * precision));
             break;
         end
         i = i+1;
     end
     if abs(y) < abs(y2)
         delta_t = index * precision;
     else
         delta_t = (index - 1) * precision;
     end
     t1 = t0 + delta_t;
     y3=(2*Th)/(vf2+vf3);
     t2=y3+t1;

    y4=(2*P)/(vf3+vf4);
    t3=y4+t2;


%**************************************Number of effective teeth and chip 
thickness*********************************************
    for i = 1 : 1 : Number_of_Points
        t(i) = i * precision;
        if t(i) < t0
            Ne;
        elseif t(i) < t2
             vf(i) = (((vf3-vf2)/(t2-t1))*(t(i)-t1)) + (vf2);
            %alpha_outer(i) = acos((R - (vf .* t(i))) ./ R);
            for n = 1: 1: N
                alpha_outer(i) = acos((R - (vf(i) .* t(i))) ./ R);
                theta_phase(n,i) = ((2 * pi) * n / N) + (omega * t(i));
                theta_judging(n,i) = (theta_phase(n,i) / (2 * pi)) - 
floor(theta_phase(n,i) / (2 * pi));
                if theta_judging(n,i) <= (alpha_outer(i) / (2 * pi)) || 
theta_judging(n,i) >= (1.0 - (alpha_outer(i) / (2 * pi)));
                    Ne(i) = Ne(i) + 1;
                    dt0(n,i) = (n*2*pi*vf(i)*sin(theta_judging(n,i)))/((omega)*N); 
%uncut chip thickness
                    As(n,i) = (dt0(n,i) * W)/ sin(phi(n,i));      %shear area
                    Tdt(i) = (sum(dt0(:,i)).');
                    TAs(i) = (sum(As(:,i)).');
                    MRR(i) =MRR(i) + ((vf(i)/(N*RPM)) * sum(dt0(:,i)) .* (N * RPM * 
W));
                end
            end
        else
            vf(i) = (((vf4-vf3)/(t3-t2))*(t(i)-t2)) + (vf3);
            for n = 1: 1: N
                alpha_outer(i) = acos((R - (vf(i) .* t(i))) ./ R);
```

```
                alpha_inner(i) = acos((R + Th - (vf(i) .* t(i))) ./ R);
                theta_phase(n,i) = ((2 * pi) * n / N) + (omega * t(i));
                theta_judging(n,i)    =    (theta_phase(n,i)    /    (2    *    pi))    -
floor(theta_phase(n,i) / (2 * pi));
                if   theta_judging(n,i)   <=   (alpha_outer(i)   /   (2   *   pi))   &&
theta_judging(n,i) >= (alpha_inner(i) / (2 * pi)) || ...
                   theta_judging(n,i)  >=  (1.0  -  (alpha_outer(i)  /  (2  *  pi)))  &&
theta_judging(n,i) <= (1.0 - (alpha_inner(i) / (2 * pi)));
                    Ne(i) = Ne(i) + 1;
                    dt0(n,i)   =   (n*2*pi*vf(i)*sin(theta_judging(n,i)))/((omega)*N);
%uncut chip thickness
                    As(n,i) = (dt0(n,i) * W)/ sin(phi(n,i));       %shear area
                    Tdt(i) = (sum(dt0(:,i)).');
                    TAs(i) = (sum(As(:,i)).');
                    MRR(i)  =  MRR(i)  +  ((vf(i)/(N*RPM))  *  sum(dt0(:,i))  .*  (N  *  RPM  *
W));
                end
            end
        end
    end
    yy = unique(dt0); %in
    yyy = yy .* 25.4; %mm
    dt0mm = dt0 .* 25.4;
    figure (1)
    plot(t, Ne)
    %title('Number of Teeth')
    set(gca,'box','off')
    xlabel('Time (\it{s}\rm{)}')
    ylabel('Number of teeth')
    figure(11)
    plot(t,MRR)
    %title('material removal rate')
    set(gca,'box','off')
    xlabel('Time (\it{s}\rm{)}')
    ylabel('MRR (\it{in3/sec}\rm{)}')
 %*******************************************************         TOOTH          FORCE
CALCULATION*************************************************************
    for i = 1 : 1 : Number_of_Points
         t(i) = i * precision;
         if t(i) < t0
         elseif t(i) < t2
              vf(i) = (((vf3-vf2)/(t2-t1))*(t(i)-t1)) + (vf2);
              alpha_outer(i) = acos((R - (vf(i) .* t(i))) ./ R);
             for n = 1: 1: N
             theta_phase(n,i) = ((2 * pi) * n / N) + (omega * t(i));
             theta_judging(n,i)    =    (theta_phase(n,i)    /    (2    *    pi))    -
floor(theta_phase(n,i) / (2 * pi));
             if    theta_judging(n,i)    <=    (alpha_outer(i)    /    (2    *    pi))    ||
theta_judging(n,i) >= (1.0 - (alpha_outer(i) / (2 * pi)));
                 Fn1(n,i)   =   2   *   pi   *   tau   *   W   *   vf(i)   *   cos(beta)   *
sin(theta_judging(n,i)) / (omega * N * sin(phi(n,i)) * cos(phi(n,i) + beta - alpha));
```

```
                 Ff(n,i) = 2 * pi * tau * W * vf(i) * sin(beta) *
sin(theta_judging(n,i)) / (omega * N * sin(phi(n,i)) * cos(phi(n,i) + beta - alpha));
                 theta_r(n,i) = atan(Ff(n,i)/Fn1(n,i)) - alpha;
                 F_tooth(n,i) = ((n * 2 * pi * tau * W) .* (vf(i) .*
sin(theta_judging(n,i)))) ./ ((omega * N) .* (sin(phi(n,i)) .* cos(phi(n,i) + beta -
alpha))); % tooth resultant force
                 Fx(n,i) = F_tooth(n,i) .* cos(beta - alpha);
                 Fy(n,i) = F_tooth(n,i) .* sin(beta - alpha);
                 NFx(n,i) = Fx(n,i) .* 4.44822;
                 NFy(n,i) = Fy(n,i) .* 4.44822;
                 ftoot(i) = ftoot(i) + (F_tooth(n,i));
                 NAFx(i) = NAFx(i) + (((ftoot(i) .* cos(beta - alpha))) .* 4.44822);
                 NAFy(i) = NAFy(i) + (((ftoot(i) .* sin(beta - alpha))) .* 4.44822);
                 fric(n,i) = Ff(n,i)/Fn1(n,i);
                 powerone(n,i) = vvi * NFx(n,i);
                 fv(n,i)=(Fx(n,i) .* cos(alpha)) - (Fy(n,i) .* sin(alpha));
                 fu(n,i)=(Fx(n,i) .* sin(alpha)) + (Fy(n,i) .* cos(alpha));
                 mu2(n,i)=fu(n,i)/fv(n,i);
                 Vc(n,i)=(sin(phi(n,i)).*vvi)./(cos(phi(n,i)-alpha));
                 Pu(n,i)=(fu(n,i)*4.44822)*Vc(n,i);
                 Pu1(i)=sum(Pu(:,i));
                 Vs(n,i)=(cos(alpha)*vvi)./(cos(phi(n,i)-alpha));
                 Fs(n,i) = F_tooth(n,i) * cos(phi(n,i)+beta-alpha);
                 Ps(n,i)=(Fs(n,i)*4.44822)*Vs(n,i);
                 Ps1(i)=sum(Ps(:,i));
                 Ptc(i)=Ps1(i)+Pu1(i);
                 Ptc1(i)=(sum(NFx(:,i))).*vvi;
                 mu(n,i) = alpha + (atan(Fy(n,i)/Fx(n,i)));
                 torque(i) = (sum(NFx(:,i))) .* (R*0.0254);
                 Kx(n,i) = ((tau*6894) * (W*0.0254) * cos(beta -
alpha))./(sin(phi(n,i)) .* cos(phi(n,i) + beta - alpha));
                 Ky(n,i) = ((tau*6894) * (W*0.0254) * sin(beta -
alpha))./(sin(phi(n,i)) .* cos(phi(n,i) + beta - alpha));
                 Ks1(n,i) = ((tau*0.006894)*cos(beta-alpha))./(sin(phi(n,i)) .*
cos(phi(n,i) + beta - alpha));
                 Ks2(n,i) = ((tau*0.006894)*sin(beta-alpha))./(sin(phi(n,i)) .*
cos(phi(n,i) + beta - alpha));
                 Ks3(n,i) = (tau*0.006894)./(sin(phi(n,i)) .* cos(phi(n,i) + beta -
alpha));
                 cuttingspeed(i) = ((vf(i)*60)/(RPM*N))*25400;
                 chipthick (n,i) = cuttingspeed(i)/tan(phi(n,i));
                 Fxx(n,i) = (NFx(n,i) * cos(theta_judging(n,i))) + (NFy(n,i) *
sin(theta_judging(n,i)));
                 Fyy(n,i) = (NFx(n,i) * sin(theta_judging(n,i))) - (NFy(n,i) *
cos(theta_judging(n,i)));
                 s2(n,i) = ((vf(i) * tau * W) .* (sin(theta_judging(n,i))) .* cos(beta
- alpha)) ./ ((omega * N) .* (sin(phi(n,i)) .* cos(phi(n,i) + beta - alpha)));
                 s3(n,i) = ((vf(i) * tau * W) .* (sin(theta_judging(n,i))) .* sin(beta
- alpha)) ./ ((omega * N) .* (sin(phi(n,i)) .* cos(phi(n,i) + beta - alpha)));
                 s1(n,i) = sqrt((s2(n,i)^2)+(s3(n,i)^2)) / ((W)* omega * N *(vf(i) *
sin(theta_judging(n,i))));
```

```
             end
             end
         else
              vf(i) = (((vf4-vf3)/(t3-t2))*(t(i)-t2)) + (vf3);
              alpha_outer(i) = acos((R - (vf(i) .* t(i))) ./ R);
              alpha_inner(i) = acos((R + P - (vf(i) .* t(i))) ./ R);
             for n = 1: 1: N
             theta_phase(n,i) = ((2 * pi) * n / N) + (omega * t(i));
             theta_judging(n,i) = (theta_phase(n,i) / (2 * pi)) -
floor(theta_phase(n,i) / (2 * pi));
             if theta_judging(n,i) <= (alpha_outer(i) / (2 * pi)) &&
theta_judging(n,i) >= (alpha_inner(i) / (2 * pi)) || ...
                   theta_judging(n,i) >= (1.0 - (alpha_outer(i) / (2 * pi))) &&
theta_judging(n,i) <= (1.0 - (alpha_inner(i) / (2 * pi)));
                 Fn1(n,i) = 2 * pi * tau * W * vf(i) * cos(beta) *
sin(theta_judging(n,i)) / (omega * N * sin(phi(n,i)) * cos(phi(n,i) + beta - alpha));
                 Ff(n,i) = 2 * pi * tau * W * vf(i) * sin(beta) *
sin(theta_judging(n,i)) / (omega * N * sin(phi(n,i)) * cos(phi(n,i) + beta - alpha));
                 theta_r(n,i) = atan(Ff(n,i)/Fn1(n,i)) - alpha;
                 F_tooth(n,i) = ((n * 2 * pi * tau * W) .* (vf(i) .*
sin(theta_judging(n,i)))) ./ ((omega * N) .* (sin(phi(n,i)) .* cos(phi(n,i) + beta -
alpha))); % tooth resultant force
                 Fx(n,i) = F_tooth(n,i) .* cos(beta - alpha);
                 Fy(n,i) = F_tooth(n,i) .* sin(beta - alpha);
                 NFx(n,i) = Fx(n,i) .* 4.44822;
                 NFy(n,i) = Fy(n,i) .* 4.44822;
                 ftoot(i) = ftoot(i) + (F_tooth(n,i));
                 NAFx(i) = NAFx(i) + (((ftoot(i) .* cos(beta - alpha))) .* 4.44822);
                 NAFy(i) = NAFy(i) + (((ftoot(i) .* sin(beta - alpha))) .* 4.44822);
                 fric(n,i) = Ff(n,i)/Fn1(n,i);
                 powerone(n,i) = vvi * NFx(n,i);
                 fv(n,i)=(Fx(n,i) .* cos(alpha)) - (Fy(n,i) .* sin(alpha));
                 fu(n,i)=(Fx(n,i) .* sin(alpha)) + (Fy(n,i) .* cos(alpha));
                 mu2(n,i)=fu(n,i)/fv(n,i);
                 Vc(n,i)=(sin(phi(n,i)).*vvi)./(cos(phi(n,i)-alpha));
                 Pu(n,i)=(fu(n,i)*4.44822)*Vc(n,i);
                 Pu1(i)=sum(Pu(:,i));
                 Vs(n,i)=(cos(alpha)*vvi)./(cos(phi(n,i)-alpha));
                 Fs(n,i) = F_tooth(n,i) * cos(phi(n,i)+beta-alpha);
                 Ps(n,i)=(Fs(n,i)*4.44822)*Vs(n,i);
                 Ps1(i)=sum(Ps(:,i));
                 Ptc(i)=Ps1(i)+Pu1(i);
                 Ptc1(i)=(sum(NFx(:,i))).*vvi;
                 mu(n,i) = alpha + (atan(Fy(n,i)/Fx(n,i)));
                 torque(i) = (sum(NFx(:,i))) .* (R*0.0254);
                 Kx(n,i) = ((tau*6894) * (W*0.0254) * cos(beta -
alpha))./(sin(phi(n,i)) .* cos(phi(n,i) + beta - alpha));
                 Ky(n,i) = ((tau*6894) *(W*0.0254) * sin(beta -
alpha))./(sin(phi(n,i)) .* cos(phi(n,i) + beta - alpha));
                 Ks1(n,i) = ((tau*0.006894)*cos(beta-alpha))./(sin(phi(n,i)) .*
cos(phi(n,i) + beta - alpha));
```

```
                 Ks2(n,i) = ((tau*0.006894)*sin(beta-alpha))./(sin(phi(n,i)) .*
cos(phi(n,i) + beta - alpha));
                 Ks3(n,i) = (tau*0.006894)./(sin(phi(n,i)) .* cos(phi(n,i) + beta -
alpha));
                 cuttingspeed(i) = ((vf(i)*60)/(RPM*N))*25400;
                 chipthick (n,i) = cuttingspeed(i)/tan(phi(n,i));
                 Fxx(n,i) = (NFx(n,i) * cos(theta_judging(n,i))) + (NFy(n,i) *
sin(theta_judging(n,i)));
                 Fyy(n,i) = (NFx(n,i) * sin(theta_judging(n,i))) - (NFy(n,i) *
cos(theta_judging(n,i)));
                 s2(n,i) = ((vf(i) * tau * W) .* (sin(theta_judging(n,i))) .* cos(beta
- alpha)) ./ ((omega * N) .* (sin(phi(n,i)) .* cos(phi(n,i) + beta - alpha)));
                 s3(n,i) = ((vf(i) * tau * W) .* (sin(theta_judging(n,i))) .* sin(beta
- alpha)) ./ ((omega * N) .* (sin(phi(n,i)) .* cos(phi(n,i) + beta - alpha)));
                 s1(n,i) = sqrt((s2(n,i)^2)+(s3(n,i)^2)) / ((W)*(vf(i) * omega * N *
sin(theta_judging(n,i))));

             end
             end
         end
     end


     CHIP = unique(chipthick);
     figure(6)
     plot(t, NAFx, 'b-')
     %title('Total Fx')
     set(gca,'box','off')
     xlabel('Time (\it{s}\rm{})')
     ylabel('Force (\it{N}\rm{})')
     figure(7)
     plot(t, NAFy, 'b-')
     %title('Total Fy')
     set(gca,'box','off')
     xlabel('Time (\it{s}\rm{})')
     ylabel('Force (\it{N}\rm{})')
     figure(8)
     plot(t, Ptc, 'b-')
     %title('shear power & friction poer')
     set(gca,'box','off')
     xlabel('Time (\it{s}\rm{})')
     ylabel('Power (\it{W}\rm{})')
     figure(9)
     plot(t,Ptc1, 'b-')
     %title ('cutting power from spindle')
    set(gca,'box','off')
     xlabel('Time (\it{s}\rm{})')
     ylabel('Power (\it{W}\rm{})')
     figure(10)
```

```
    plot(t,torque, 'b-')
    %title ('torque')
    set(gca,'box','off')
    xlabel('Time (\it{s}\rm{})')
    ylabel('Torque (\it{Nm}\rm{})')
    figure(24)
    plot(t, Ps1, 'b-')
    %title ('shear power')
    set(gca,'box','off')
    xlabel('Time (\it{s}\rm{})')
    ylabel('Power (\it{W}\rm{})')
    figure (25)
    plot(t,Pu1, 'b-')
    %title ('friction power')
    set(gca,'box','off')
    xlabel('Time (\it{s}\rm{})')
    ylabel('Power (\it{W}\rm{})')



%*****************************Displacement Calculation******************************

kx = 2.3e7;                         % N/m
zetax = 0.02;
wnx = omega;                      % rad/s
mx = kx/(wnx^2);                    % kg
cx = 2*zetax*sqrt(mx*kx);           % N-s/m

% Define parameters for y direction
ky = kx;                           % N/m
zetay = 0.02;
wny = omega;                      % rad/s
my = ky/(wny^2);                    % kg
cy = 2*zetay*sqrt(my*ky);           % N-s/m

x = 0;
dx = 0;
y = 0;
dy = 0;
```

```
    ddx = (TFXX - cx*dx - kx*x)/mx;
    dx = dx + (ddx*precision);
    x = x + dx*precision;
    xpos = x;

    ddy = (TFYY - cy*dy - ky*y)/my;
    dy = dy + ddy*precision;
    y = y + dy*precision;
```

```
    ypos = y;

xd = 0;
dxd = 0;
gd = 0;
dgd = 0;


figure(30)
plot (t,xpos*1e6,'b-')
%title('displacement in x direction')
set(gca,'box','off')
xlabel('Time (\it{s}\rm{)}')
ylabel('Displacement (\it{\mum}\rm{)}')
figure(31)
plot(t,ypos*1e6,'b-')
%title('displacement in y direction')
set(gca,'box','off')
xlabel('Time (\it{s}\rm{)}')
ylabel('Displacement (\it{\mum}\rm{)}')

% Calculate FFT of time domain Force signal
Force = (TFXX.^2 + TFYY.^2).^0.5;
NN = length(Force);
fs = 1/precision;              % sampling frequency, Hz
F_mean = mean(Force);
Force = Force - F_mean; % remove mean prior to computing FFT
F = fft(Force');
F = F(1:NN/2+1);
F = F/(NN/2);            % correct amplitude
F(1) = F_mean;          % replace DC value with mean
f = [0:fs/NN:(1-1/(2*NN))*fs]';
f = f(1:NN/2+1);         % frequency, Hz


figure(35)
plot(f, abs(F))
axis([0 5 0 800])
set(gca,'box','off')
xlabel('Frequency (\it{Hz}\rm{)}')
ylabel('Force (\it{N}\rm{)}')
```

Appendix B

```
%*****************************Shear angle calculation for minimum applied
force******************

function k = myfunc(Phi)
```

```
beta = 8.5*pi/180;
alpha = 10*pi/180;
tau = 71838.8;
R = 40000;
chip = xlsread('D:\first review\pro\Force calculation\abaqus\p\chip.xlsx', 'Sheet3');
Z = R./(tau.*chip);


    for i=1:1:length(Z)
A = [1-(sin(beta)*sin(Phi)/(cos(beta-alpha)*cos(Phi-alpha)))];
B = [1/(cos(Phi-alpha))^2-1/(sin(Phi))^2];
C = [cot(Phi)+tan(Phi-alpha)+Z(i)];
D = (sin(beta)/cos(beta-alpha));
E = [cos(Phi)/cos(Phi-alpha)+sin(Phi)*sin(Phi-alpha)/(cos(Phi-alpha))^2];

k = (A*B)+(C*D*E);
    end

clc;
clear all;
close all;
format long
chip = xlsread('D:\first review\pro\Force calculation\abaqus\p\chip.xlsx', 'Sheet3');
beta = 8.5*pi/180;
alpha = 10*pi/180;
tau = 71838.8;
R = 40000;
Z = R./(tau.*chip);

x0 = (pi/4)-((1/2)*(beta-alpha));
for i=1:1:length(Z)
[x(i),fval] = fsolve(@myfunc,x0);
sol = (180/pi)*x;
end
```

Appendix C

```
%**********************Natural frequency calculation********************
clc;
clear all;
close all;
```

Constant parameters for all three materials

```
h = 0.023*0.0254;
```

```
ro = 8160;

nu = 0.3;

alpha = 1.0e+03*[0.6637 0.9841 2.7202 7.6939];
```

Computation of natural frequencies for AISI M2

```
D1 = 3.07*0.0254;

E1 = 2.1e+11;



omega_M2 = (h/D1^2)*sqrt(E1*alpha/(12*ro*(1-nu)));

f_M2 = (1/(2*pi))*omega_M2;
```

Computation of natural frequencies for AISI M35

```
D2 = 3.227*0.0254;

E2 = 30022811.71*6894.76;



omega_M35 = (h/D2^2)*sqrt(E2*alpha/(12*ro*(1-nu)));

f_M35 = (1/(2*pi))*omega_M35;
```

Computation of natural frequencies for AISI M42

```
D3 = 3.25*0.0254;

E3 = 29007547.55*6894.76;



omega_M42 = (h/D3^2)*sqrt(E3*alpha/(12*ro*(1-nu)));

f_M42 = (1/(2*pi))*omega_M42;
```